# ‘A tale of two codons: Synergistic mechanisms in oncogenic Nras induced hematological malignancies’

By

Adhithi Rajagopalan

A dissertation submitted in partial fulfillment of the requirements for the degree of

Doctor of Philosophy

(Cellular and Molecular Biology)

at the

UNIVERSITY OF WISCONSIN- MADISON

2022

Date of final oral examination: May 4th, 2021

The dissertation is approved by the following members of the Final Oral Committee:

Jing Zhang, Professor, Oncology

Emery Bresnick, Professor, Cell and Regenerative Biology

Shigeki Miyamoto, Professor, Oncology

Shannon Kenney, Professor, Oncology

Igor. I. Slukvin, Professor, Pathology & Laboratory Medicine

## Abstract

RAS genes (*NRAS, KRAS, and HRAS)* are the most frequently mutated family of genes in solid tumors such as colorectal cancer, pancreatic ductal adenocarcinoma, lung adenocarcinoma, melanoma, and in certain hematological cancers such as juvenile myelomonocytic leukemia. All mutant *RAS* are not created equal- there is emerging understanding of the striking differences in the frequency of specific isoforms and codons that are mutated in different cancer types. *NRAS Q61* mutations are predominant in plasma cell myeloma whereas *NRAS G12* mutations are more prevalent in acute myeloid leukemia (AML). Biochemically, the intrinsic GTPase activity of G12 and G13 mutations is more activating than that of Q61 mutations. Thus, it is crucial to understand Ras isoform and codon specific mechanisms that promote tumor progression in order to develop appropriate therapeutic regimens.

In human multiple myeloma (MM) patients, *RAS* pathway mutations constitute >50% of advanced and relapsed cases, with *NRAS* mutations occurring equally in untreated advanced and relapsed MM patients. *NRAS Q61* mutations correlate with poor patient outcomes, thus underscoring the importance of *NRAS* downstream signaling in both MM progression and drug resistance. To understand these *RAS* dependent mechanisms, we genetically engineered a murine model conditionally expressing oncogenic $Nras^{Q61R}$ and *MYC* transgene in the germinal center B cells, hereafter dubbed “VQ mice”. VQ mice display most of the biological and clinical features seen in human myeloma such as impaired hematopoiesis, bone lesions and kidney abnormalities. VQ mice also display several characteristics of advanced/high-risk MM, such as high proliferation index, hyperactivation of ERK and AKT signaling, and extensive extramedullary disease. At the molecular level, these MM cells preserved key inhibitory immune checkpoint pathways such as PD-L1/PD-1 and CD155/TIGIT as well as gene signatures corresponding to human high-risk MM. These MM phenotypes are transplantable in syngeneic recipients. The VQ model yielded two MM cell lines that facilitate a tractable system for future genetic manipulations.

Combination therapies based on MEK inhibition significantly prolonged survival of VQ recipients with advanced-stage MM. Thus, our study provides compelling evidence to build combinatorial therapeutic strategies based on MEK-inhibition. The resources generated herein will prove to be useful in exploring and developing such strategies in the future.

Although *NRAS* mutations are predominant in AML, they may function as early/initiating or as cooperating mutations that are acquired during disease progression. Mice expressing $Nras^{G12D/+}$ in hematopoietic system develop chronic myelomonocytic leukemia characterized by persistent monocytosis in peripheral blood, but these mice do not spontaneously transform to AML. This underscores the importance of additional genetic events to promote transformation of oncogenic *Nras*. This was evidenced by our previous study where loss of tumor suppressor gene *p53* cooperates with oncogenic $Nras^{G12D}$ to transform megakaryocyte-erythroid progenitor cells and promote AML. Therein, we also reported that AML patients with concurrent mutations in both *RAS* pathway and *TP53* had a significantly shorter survival compared to patients with single pathway mutations. Importantly, majority of these *TP53* mutations reported were missense mutations. Missense *p53* mutations have been shown to confer gain-of-function properties in several solid tumor and hematological malignancies. Thus, we investigated the genetic interaction between *p53* missense mutant ($p53^{R172H}$) and oncogenic *Nras*. Our study shows prominent synergism between $p53^{mut}$ and $Nras^{G12D}$ resulting in a fully penetrant, rapidly lethal AML in primary mice. Interestingly, we found that mechanisms of $p53^{mut}$ and oncogenic *Nras* cooperation are distinct from that of loss of *p53*. $p53^{mut}$ driven transformation of $Nras^{G12D}$ mice was characterized by downregulation of key hematopoietic transcription factor Gata2 network, upregulation of several receptor-like tyrosine kinases and enrichment of inflammatory and Toll-like receptor (TLR) pathways. These result in hyperactivation of downstream signaling pathways including MEK/ERK and NFκB. These distinct mechanisms support the idea that *p53* missense mutations may confer unique properties in driving leukemogenesis in the context of oncogenic *Nras*.

## Table of contents

## List of figures

**Chapter 1**



**Chapter 2**

## List of Tables

**Chapter 2**



**Chapter 3**

**Acknowledgements**

I would like to thank my mentor, Dr. Jing Zhang, for her continued guidance and support throughout my graduate school. She has been instrumental in shaping my approach towards science and its practice. Her constant encouragement even in the face of hardships have inspired me to try and overcome many hurdles. One can learn a lot from her vast knowledge about the complex world of hematopoiesis and leukemia and more importantly, her impeccable sense of how to succinctly communicate it. She has not only taught me how to be critical but also creative about doing science. I hope I can carry forward these valuable lessons as I forge on.

Secondly, I would like to extend my appreciation to all my committee members, Drs. Emery Bresnick, Shigeki Miyamoto, Igor Slukvin, Shannon Kenney and Michael Gould. Their thought-provoking questions about the nuances of my project have continued to inspire my scientific thinking. Although the current circumstances of a global pandemic preclude an in-person meeting to thank them, nevertheless, I hope to convey my gratitude with these words.

The work contained herein is not the product of a single person, but a network of curious, brilliant scientists who relentlessly lend their scientific knowledge and expertise to help answer our questions. In this respect, I would like to thank our collaborators, Drs. Fotis Asimakopoulos, Erik Ranheim, Natalie Callander, Robert Burns, Demin Wang without whom this work would be impossible. I would also like to thank Dr. Xinmin Zhang, (COO, BioInfoRx) for his valuable inputs in the field of bioinformatics.

In some ways, the Zhang lab members, both past and current, have been my pseudo-mentors. They have always been there not only to help troubleshoot experiments but also be a reliable support. Special thanks to Dr. Zhi Wen, who has been a great collaborator to tackle the intricacies of the “VQ myeloma model”. My sincerest gratitude to Xiaona, Yun and Evan, who have always been a source of motivation and positivity. It was my pleasure to mentor Taylor Klungness, a diligent undergraduate researcher, whom I could always count upon.

The scientific community of UW-Madison, especially the McArdle weekly seminars and Blood Research Group seminars have always been a source of inspiration and enthusiasm and I am deeply indebted to them.

It would be remiss of me if I did not thank the UWCCC Flow Cytometry Core, especially Dagna, Kathryn, Lauren, Zach and Alex. There have been numerous occasions when they took time out of their personal lives to help with my flow sorting experiments, and I am ever so grateful for their patience and support. Thanks also to RARC SMPH Vet Staff & WIMR Vivarium Staff for their continuous support in taking care of our experimental animals.

To friends who became my family here in Madison, words would not suffice to express my gratitude.

To my parents, sister, and partner - you have been my pillars of support throughout this journey. There may have been an iPad screen separating us always, but your warm, encouraging words have always lifted my spirits.

# Chapter 1

# Introduction

### 1.1 Ras family of small-GTPases: an overview

In 1964, scientists studying cancer-causing viruses at the Cancer Research Department of the London Hospital Research Laboratories unexpectedly found that a murine leukemia virus taken from a leukemic rat could also induce sarcomas (solid tumor) in rodents (1). Subsequently, additional murine sarcoma retroviruses (MSVs) were identified and named after the scientists who discovered them, Kirsten-MSV and Harvey-MSV (2-4). About a decade later, Scolnick *et. al.* reported that these MSVs were recombinant viruses that carried, in addition to the replication competent helper retrovirus, two different rat cellular sequences- the 30s RNA, and a mutated form of the rat cellular gene later named *Ras*, a portmanteau of "Rat sarcoma" (5-7).

RAS proteins belong to the family of small guanosine triphosphatases (GTPases) that include over 150 members in mammals, broadly divided into five major groups based on the sequence and functional similarities: RHO, RAB, RAN, ARF and the founding member RAS (8, 9). Small GTPase family members function as guanine nucleotide binding proteins (G proteins) capable of intrinsically hydrolyzing bound GTP to GDP (guanosine diphosphate) (10). Thus, RAS proteins act as binary molecular switches that cycle between GTP-bound ON and GDP-bound OFF states.

RAS activation requires dissociation of bound GDP, but due to high affinity binding between the two, this dissociation is an intrinsically slow process that can be hastened by guanine nucleotide exchange factors (GEFs) (11). Structurally, the RAS-protein bound nucleotide is sandwiched between two loops called switch 1 and switch 2 (Figure 1.1). The switch regions along with the phosphate-binding loop (P loop) interact with the phosphates and a facilitating magnesium ion. GEF binding induces conformational changes in the switch regions and the P loop thus decreasing nucleotide affinity resulting in GDP release (12).

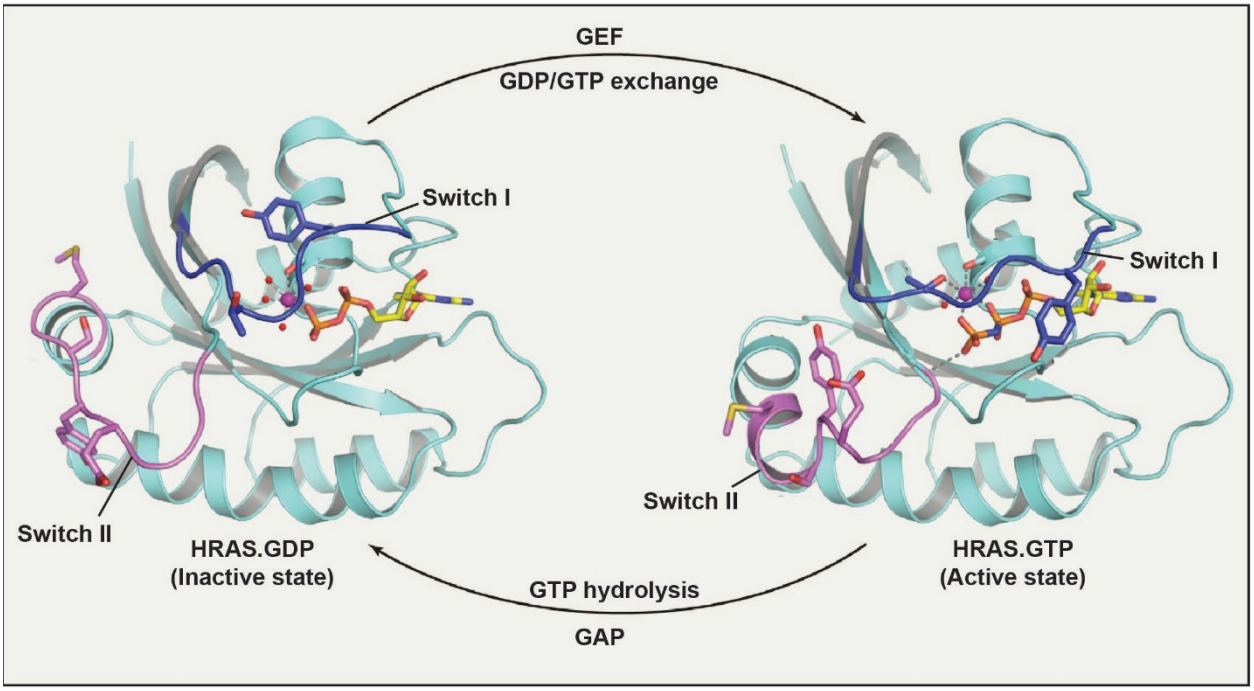


Figure 1.1: RAS conformational changes during activation cycle (adapted, 79)

Affinity of RAS for GTP and GDP is similar, and the GEF does not prefer one over the other either. Rather, due to the much higher cytosolic concentration of GTP compared to GDP, there is an increase in GTP-bound RAS resulting in an “ON” state that facilitates downstream signaling important for various cellular processes. To turn the switch off, the RAS-bound GTP should be hydrolyzed to GDP (GTPase reaction), which is an irreversible reaction. Though RAS proteins are GTPases, their intrinsic GTP hydrolysis reaction is very slow but association with GTPase-activating proteins (GAPs) can accelerate this process by several orders of magnitude. The reaction mechanism involves proper positioning of a water molecule opposite to the γ-phosphate moiety of the leaving GDP. Structural insights show that stabilization of the position of RAS glutamine 61 by RASGAP helps to coordinate the attacking water (13). Neutralization of the negative charge on the γ-phosphate is facilitated by positioning of the arginine finger into the phosphate-binding site, thus stabilizing the transition state.

The three mammalian *Ras* genes *Hras*, *Kras* and *Nras* are located on different chromosomes, composed of four coding exons and a 5' non-coding exon. These genes encode four homologous 21kDa proteins- Hras, Kras4A, Kras4B and Nras (14-16). The two protein isoforms of KRAS are generated by alternative splicing of the fourth coding exon of the *Kras* gene, with the more ubiquitous isoform KRAS4B containing 188 amino acids (a.a) and KRAS4A having 189 a.a, the same number of a.a as HRAS and NRAS proteins. The four proteins are highly homologous throughout the "G domain" which spans amino acid residues 1-165 (Figure 1.2). The first 85 amino acids are identical and dictate binding to GDP and GTP. This region includes the P loop (10-16 a.a) that binds the γ-phosphate of GTP, switch I (32-38 a.a) and switch II (59- 67 a.a) both of which also govern binding regulators and effectors of RAS proteins. Amino acids 86-165 show ~85-90% sequence identity, while the remaining C-terminal "hypervariable region" spanning a.a 165-188 (or 165-189 in KRAS4A) is the only diverse region. This hypervariable (HVR) domain contains sequences that are undergo post-translational modifications necessary for localization of Ras proteins to the inner cell membrane (17).

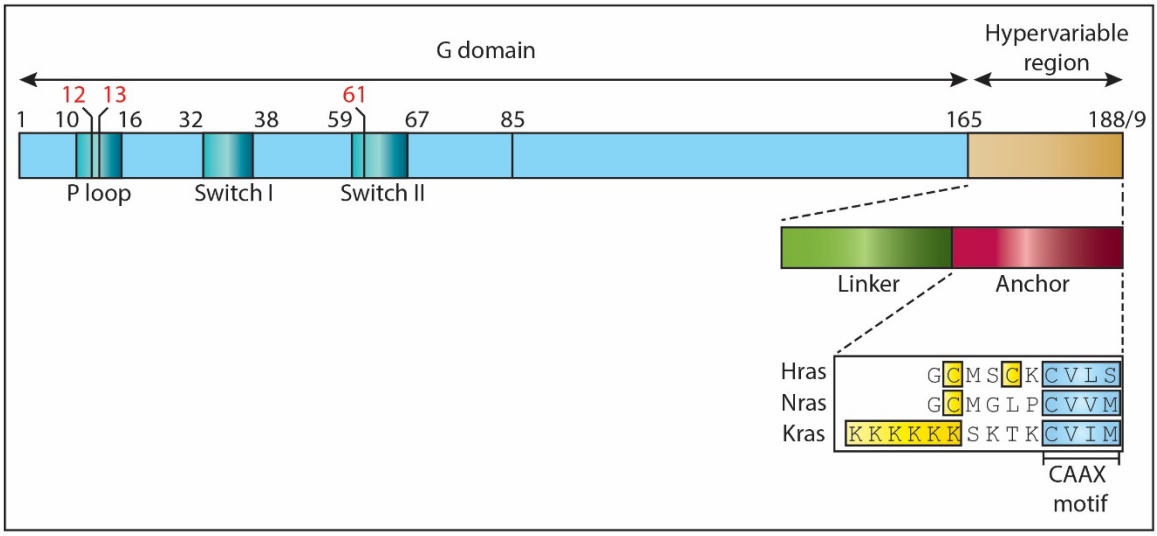


Figure 1.2: Ras protein domain structure (adapted, 16-17)

The HVR of all the RAS isoforms terminates with a CAAX motif, which undergoes three different modifications (Figure 1.2, inset). RAS proteins are synthesized as precursors in the cytosol and are prenylated at the cysteine residue of CAAX motif by farnesyl transferase enzyme. This farnesylation targets RAS to ER cytosol surface where Ras-converting enzyme I (Rce-1), an endopeptidase, cleaves the AAX tripeptide. The carboxyl group of the carboxy-terminal farnesyl-cysteine is methylated by isoprenylcysteine carboxyl methyltransferase (ICMT). A second signal motif stabilizes the weak membrane binding affinity. Hras, Nras and Kras4A undergo palmitoylation on cysteine next to the CAAX motif whereas the polylysine domain of Kras4B stabilizes its interaction with the phospholipid membrane. The palmitoylation/ depalmitoylation cycle enables H-, N- and K-RAS4A traffic through the Golgi to the plasma membrane (PM) and back via vesicles, while KRAS4B directly localizes to the PM through diffusion (18). Recent studies have shown that RAS proteins may undergo oligomerization or dimerization after membrane localization, thus leading to effective downstream signaling (19-22). Incorrect processing or perturbation of these modifications results in mis-localization of the RAS protein, thus decreasing RAS signaling from the plasma membrane (23, 24).

RAS signaling cascade can be activated by several upstream cellular receptors including family members of receptor tyrosine kinases (RTKs), G-protein coupled receptors (GPCRs), and integrins (25). Activation of these upstream receptors triggers signaling cascades that mediate RAS activation from an inactive GDP-bound state to an active GTP-bound state through the assembly of several scaffolding proteins. Perhaps the earliest and most well characterized upstream receptor in this regard is the Epidermal Growth Factor Receptor (EGFR) (26, 27). EGFR is an RTK family member anchored to the plasma membrane, that includes three other members (erbB2/HER-2, erbB3/HER-3, and erbB4/HER-4). In normal tissues, ligand binding to the receptor causes a conformational change in the receptor that results in its dimerization and autophosphorylation of several tyrosine residues in the receptor cytoplasmic tail (Figure 1.3). Key

phosphorylated tyrosine residues provide docking sites for cytoplasmic adaptor proteins containing Src homology 2 (SH2) and phosphotyrosine-binding domains, such as growth-factor-receptor-bound protein 2 (GRB2) (28). GRB2 is bound to Son of Sevenless (SOS), a RAS-GEF protein, via Src homology 3 (SH3) domain, thus recruiting SOS to the membrane where RAS is located. Proximity of SOS to RAS results in exchange of GDP for GTP, resulting in activation of RAS protein. Although the above process is a generally accepted sequence of events preceding RAS activation, owing to the diversity in upstream receptors, scaffolding proteins, GEFs and GAPs, RAS can by activated by a wide variety of extracellular stimuli through a myriad of upstream mechanisms (11, 29- 31).

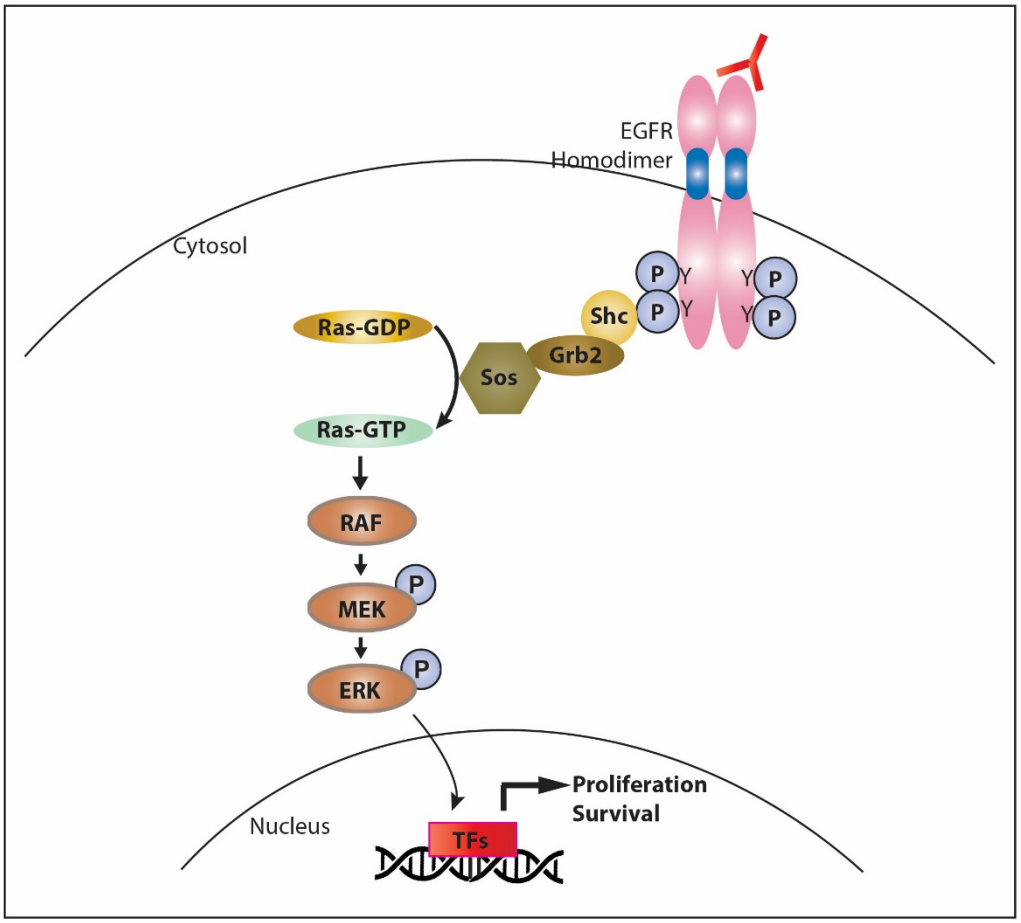


Figure 1.3 Ras signaling activation downstream of EGFR (adapted, 27)

Activated RAS (GTP-bound) facilitates downstream signaling by binding to its effectors, through which it regulates a wide variety of cellular processes including cell cycle progression, differentiation, metabolism, and apoptosis among others (32-35) (Figure 1.4). The three major RAS effector proteins include RAF kinase, phosphatidylinositol 3-linase (PI3K) and RalGDS, which are characterized by the presence of a putative RAS binding domain or RBD.

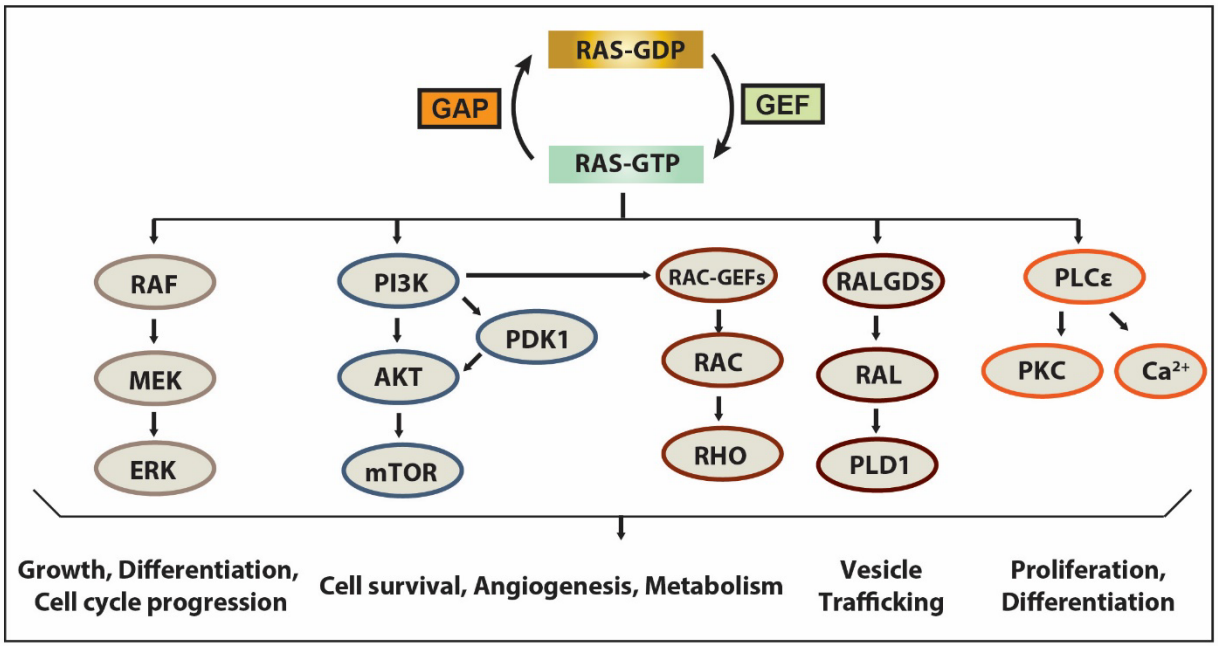


Figure 1.4 Ras Effector pathways (adapted, 25,52)

The earliest and most well characterized RAS effector pathway is the mitogen-activated protein kinase (MAPK) pathway defined by RAF/MEK/ERK signaling axis (36, 37). GTP bound RAS binds to serine/threonine kinase RAF, resulting in its membrane recruitment and activation. There are three closely related Raf family members, A-Raf , B-Raf, and Raf-1/C-Raf, which when activated, can phosphorylate specific serine/threonine (S/T) residues of and activate downstream mitogen-activated protein kinases 1 and 2 (MEK1 and MEK2). MEKs are dual-specificity kinases that can further phosphorylate downstream extracellular signaling-regulated kinases 1 and 2 (ERK1 and ERK2). Activated ERK1/2 serine/threonine kinases phosphorylate and further activate

a wide variety of cytosolic and nuclear protein substrates (>60 substrates) such as p90 ribosomal six kinase-1 ($p90^{Rsk-1}$) that can influence gene expression by activating cyclic-AMP (cAMP) response element-binding protein transcription factor (38). Importantly, ERK can phosphorylate ETS family of transcription factors such as ELK1, which in turn control expression of several immediate early genes including *FOS*, *JUN* and *MYC*. FOS and JUN can form AP-1 dimer that further promote expression of key cell-cycle regulatory proteins such as Cyclin-D and enable cell cycle progression through G0/G1 phase (39, 40). In addition, ERK can also phosphorylate upstream pathway members such as B-Raf, MEK1 or SOS, and alter their activity to exert negative feedback in certain contexts (41-43).

In addition to RAF, RAS has been shown to activate lipid kinases such as Type I phosphatidylinsositol 3-kinases (PI3Ks), by directly interacting with the catalytic subunit (p110) and inducing its membrane translocation and conformational change (44, 45). Activated PI3K then phosphorylates phosphatidylinositol-4,5-bisphosphate (PIP2) to produce phosphatidylinositol-3,4,5-bisphosphate (PIP3), a lipid secondary messenger that can recruit downstream kinases such as phosphatidyl inositol-dependent kinase 1 (PDK1) and PKB/AKT to the plasma membrane, where PDK1 phosphorylates and activates AKT (46,47). Some AKT isoforms (such as AKT3) have a strong anti-apoptotic function by inhibiting key pro-apoptotic enzymes as well as promoting cell growth and metabolism (48, 49). PI3K activation also leads to stimulation of RAC, a RHO family protein, that can regulate actin cytoskeleton and key transcription factor pathways such as nuclear factor-κB (NF- κB) (50). Apart from RAF and PI3K effector pathways, another well-studied effector family consists of the three exchange factors for the RAS-related RAL proteins (RALGDS, RGL and RGL2), through which RAS can stimulate RAL and its downstream pathway to promote survival of transformed cells (51). Apart from the above described major pathways, there are numerous others that act downstream of activated RAS and these have been comprehensively curated elsewhere (25, 52).

### 1.2 Role of *RAS* pathway in hematopoiesis

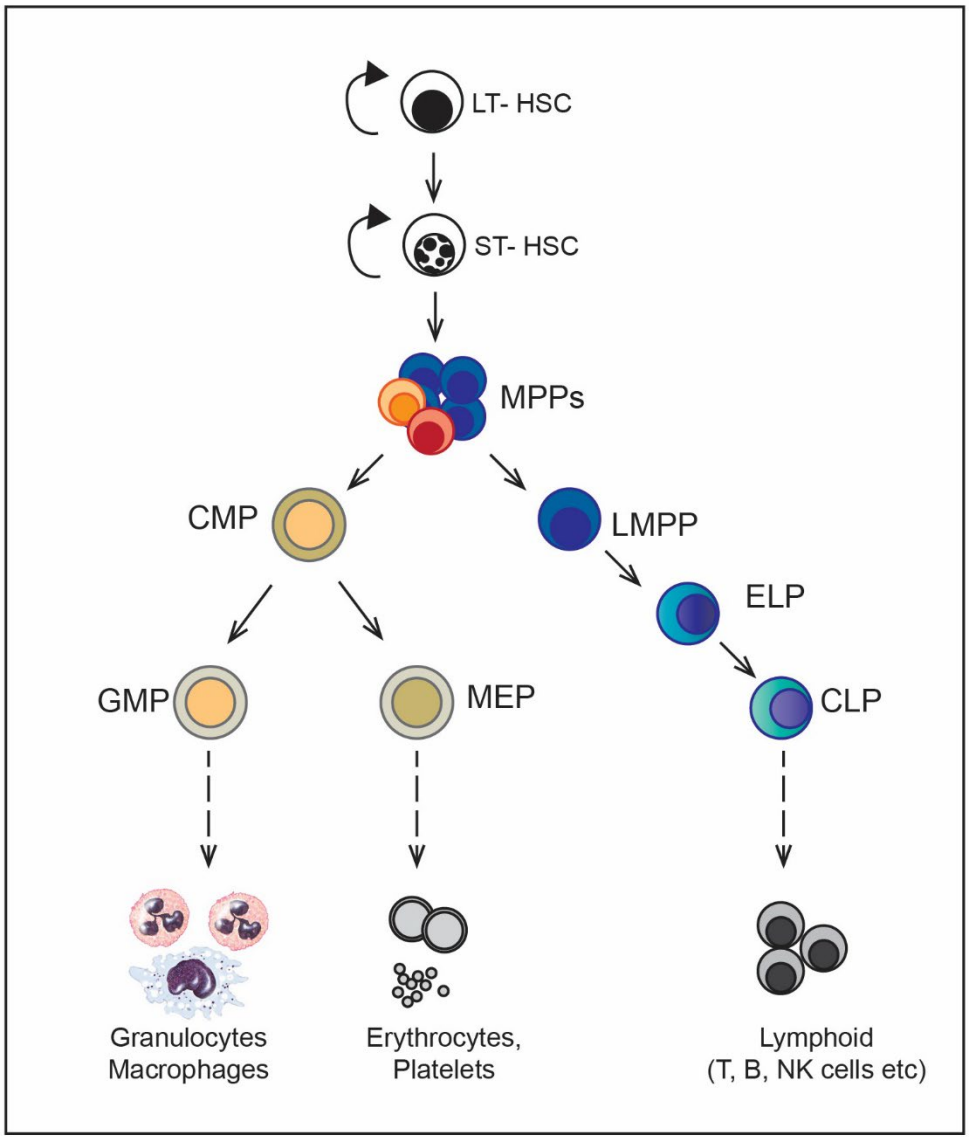


Figure 1.5 Schematic illustration of hematopoietic differentiation hierarchy

Hematopoiesis is the formation of blood cellular components and occurs during embryonic development and throughout adulthood to continuously replenish the blood system (53). In adult mammals, it is a hierarchically ordered process with the hematopoietic stem cell (HSCs) at the apex of the hierarchy and increasingly lineage restricted progenitor cells further downstream (Figure 1.5). HSCs fundamentally possess the ability to self-renew for a long-term (i.e., produce

more HSCs) as well as differentiate into more lineage committed progenitors. HSCs differentiate into multipotent progenitors (MPPs), which can have intermediate or short-term repopulating capacity with a limited self-renewal potential. Current models of hematopoietic hierarchy suggest successive loss of specific lineage potentials, with MPPs losing erythroid/megakaryocytic potential developing into lymphoid-primed MPPs (LMPPs) and early lymphoid progenitors (ELPs). ELPs further lose myeloid potential to become common lymphoid progenitors (CLPs) that give rise to terminally differentiated lymphoid cells. MPPs also give rise to the common myeloid progenitors (CMPs) that generate granulocyte/macrophage progenitors (GMPs) and their terminally differentiated granulocytes (basophils, neutrophils, and eosinophils) and macrophages and megakaryocyte/erythroid progenitors (MEPs) that terminally differentiate into erythrocytes, platelets etc. These various cell populations can be detected in hematopoietic tissues using analytical methods such as flow cytometry that uses fluorochrome-conjugated antibodies against the specific cell surface markers.

Different *Ras* isoforms play different roles in hematopoiesis, as evidenced by studies of effect of gene knockout on murine hematopoiesis. *Kras*$^{-/-}$ mice die between embryonic stage E12 and E14, likely due to hematopoietic defects, as indicated by overall pale color of embryos and increased fetal liver cell death (55). *In vitro* culture of erythroid progenitors from *Kras*$^{-/-}$ fetal liver indicate delayed differentiation of early erythroid blasts (80). Loss of *Kras* results in reduction of Erythropoietin (EPO) or Stem Cell Factor (SCF) dependent Akt activation in fetal liver cells (80). In addition, *Kras*$^{-/-}$ fetal liver cells have similar reconstitution ability compared to control cells (55). These data suggest that *Kras* is largely dispensable for fetal liver hematopoiesis. To study *Kras* function in adult hematopoiesis, we generated a *Kras* conditional knockout allele and combined with *Mx1-Cre* or *Vav-Cre*, thus overcoming the embryonic lethality of *Kras* germline knockout mice (63). Loss of *Kras* in adult hematopoietic system results in reduced long-term and intermediate-term HSC compartments and their decreased self-renewal capability. *Kras* deficiency also

reduced thrombopoietin (TPO) stimulated signaling in HSCs and MPPs, with an imbalance in myeloid and common lymphoid progenitor populations. Deletion of *Kras* in hematopoietic compartment using Vav-Cre impairs early B cell development at the pro to pre-B cell transition stage and late B cell maturation (61). This impairment is B-cell autonomous, as B cell-specific deficiency of Kras in BM chimeric mice (mix of Vav-Cre $Kras^{fl/fl}$ and B cell-deficient μMT BM cells transplanted into sub-lethally irradiated Rag1-deficient or lethally irradiated μMT mice) resulted in defective B cell development (61). By contrast, *Kras* deficiency has no effect on early T cell development or T cell maturation. However, *Kras* deficiency specifically impairs Th17 cell differentiation from CD4 T cells (81). Kras deficiency reduced T-cell Receptor (TCR) induced cell proliferation, ERK activation and altered TCR-induced gene expression profiles. As a consequence, *Kras* loss does not affect anti-leukemia activity of CD8 T cells but compromises graft-versus-host effects mediated by CD4 T cells.

In contrast to $Kras^{-/-}$, $Hras^{-/-}$ and $Nras^{-/-}$ mice are viable and fertile (56-57). Deficiency of *Hras* or *Nras* does not hamper early T cell development, but both $Hras^{-/-}$ and $Nras^{-/-}$ negatively affect Th1 response of CD4+ T cells and IFN-γ production (58). *Nras* deficiency causes a reduction in CD8 single positive thymocyte numbers due to decreased proliferation and impairs CD8 T cell memory (59,60).

### 1.3 Differential role of *RAS* isoforms and codons in cancer

Though *RAS* mutations are genetic drivers in several types of cancers such as colorectal carcinoma (CRC), pancreatic ductal adenocarcinoma (PDAC), lung adenocarcinomas (LAC), melanoma and certain hematological cancers (65-69), the frequency and distribution of *RAS* gene mutations are not uniform (70). RAS mutation tropism is seen among different RAS isoforms as well as specific codon changes within an isoform. Mutations in *RAS* isoforms have been found in over 30% of human cancers causing an accumulation of GTP-bound “ON” conformation of RAS

and hyperactivation of downstream signaling (64). *KRAS* is the most frequently mutated isoform, mutated in 75% of RAS-driven cancers, followed by *NRAS* (17%) and less frequently, *HRAS* (7%) (82). In PDAC, ~88% harbor *KRAS* mutations compared to 0.5% *NRAS*. 50% of colon or rectal adenocarcinoma have mutated *KRAS* compared to <5% in which *NRAS* is mutated. *NRAS* is the predominantly mutated isoform in skin cutaneous melanomas, whereas *HRAS* mutations, although rare, are predominant in bladder urothelial carcinomas and head and neck squamous cell carcinomas. Overall, in hematological malignancies, both *KRAS* and *NRAS* are mutated at significant frequencies whereas *HRAS* mutations are rare. *NRAS* is mutated at twice the rate as *KRAS* in acute myeloid leukemia (AML), and slightly higher in chronic myelomonocytic leukemia (CMML) and its juvenile counterpart JMML (72, 82). Interestingly, both *KRAS* and *NRAS* are roughly equally mutated in multiple myeloma, a cancer of plasma cells (73, 74, 82).

*RAS* gene mutations are predominantly single base missense mutations, most of which occur at residues G12, G13 or Q61. These mutations disrupt GTP hydrolysis and guanine exchange rates of RAS proteins resulting in accumulation of a persistently GTP-bound RAS. Though mutations at these codons are all considered to be oncogenic, they are biochemically and functionally distinct (75). Mutations in codon 12, 13 decrease rate of GTP hydrolysis by partially decreasing the intrinsic GTPase activity of RAS and preventing proper position of the Ras-GAP arginine finger within the catalytic site. In addition to improper positioning of Ras-GAP arginine finger, mutations in codon 61 decrease the rate of GTP hydrolysis by completely abolishing intrinsic GTP-ase function leading to a more severe impairment (76). Thus, G12 and G13 mutations are less activating than Q61 mutations.

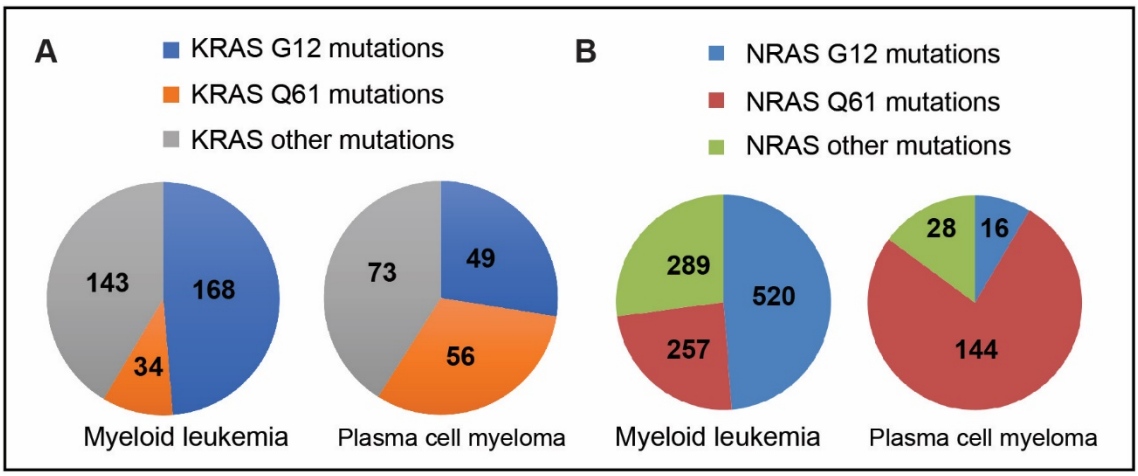


Figure 1.6 *NRAS* and *KRAS* mutation codon usage in patients with heme malignancies (Adapted 82, 76 (Fig S1A))

While most *KRAS* and *HRAS* mutations occur at G12 codon, Q61 mutations are predominant in *NRAS* (Table S3, 82). There are also differences in the relative frequency of mutations at the three codons in different cancer types. In solid tumors such as PDAC and LAC, *KRAS* G12 mutations are predominant whereas in CRC, *KRAS* G13 mutations also occur at a considerable frequency (20%) (69). Interestingly, in hematological malignancies, both G12 and Q61 *KRAS* codons are mutated at similar frequencies in plasma cell myelomas, whereas G12 codon is favored in AML & CML (82). (Figure 1.6 A) In hematological malignancies with *NRAS* mutations, G12 mutations are 46%-48% of all codons mutated in myeloid leukemia, while Q61 mutations are predominant in plasma cell myeloma (Figure 1.6 B). We have previously shown that the leukemogenic properties of endogenous *NRAS* oncogenes depends on the specific mutated codons (77). Activation of endogenous $Nras^{Q61R/+}$ mutation in hematopoietic system using Mx1-Cre resulted in leukemia phenotypes that were more potent than $Nras^{G12D/+}$, but lesser compared to homozygous $Nras^{G12D/G12D}$. $Nras^{Q61R/+}$ induced increase of Nras-GTP and cytokine signaling was intermediate between $Nras^{G12D/+}$ and $Nras^{G12D/G12D}$. Given the prevalence of specific *Nras* codon mutations in certain hematopoietic malignancies, this murine system can be

leveraged to understand how different *Nras* codon mutations interact with additional genetic mutations to accelerate or alleviate leukemia/other hematological malignancy phenotypes.

### 1.4 Synopsis of this research

The goal of this thesis is to understand how specific *Nras* codon mutations promote different hematological malignancies in cooperation with other genetic alterations. *NRAS* Q61 mutations are predominant in advanced/relapsed multiple myeloma (MM), whereas G12D mutations are frequently found in myeloid malignancies (76). The first question we addressed is whether expression of oncogenic $Nras^{Q61R}$ cooperates with *MYC* transgene in germinal center B cells to promote multiple myeloma (78). The second question is to determine whether oncogenic $Nras^{G12D}$ synergizes with *p53* missense mutant to promote AML.

To address the first question, we conditionally activated expression of endogenous $Nras^{Q61R}$ and a MYC transgene in germinal center (GC) B cells, deemed 'VQ mice'. VQ mice developed a highly malignant MM, with several characteristics that recapitulate biological and clinical features of human advanced/high-risk MM. The MM phenotypes seen in primary VQ mice were serially transplantable and also yielded two tractable myeloma cell lines. This facilitates future genetic manipulations and therapeutic ventures to develop MEK-inhibition based therapies to treat advanced/relapsed MM.

Previously, we had shown a subset of AML patients with concurrent mutations in RAS pathway and *TP53* had inferior survival than patients with single pathway mutations. Most of the *TP53* mutations seen in these patients were missense mutations, which are purported to have gain-of-function properties. We previously showed that oncogenic $Nras^{G12D}$ synergized with *p53* deficiency in mice, transforming MEPs to initiate AML. To test whether this observation rings true for *p53* missense mutant, we expressed $p53^{R172H}$ mutant and oncogenic $Nras^{G12D}$ in the hematopoietic system. We found that the genetic interaction of the two mutations induced a fully

penetrant, rapidly lethal AML in primary mice and recipients. Although *p53*$^{mut}$ can also synergize with oncogenic *Nras*$^{G12D}$, the underlying cellular and molecular mechanisms were distinct from loss of *p53* driven transformation of *Nras*$^{G12D}$. *p53*$^{mut}$ driven transformation of *Nras*$^{G12D}$ mice was characterized by downregulation of key hematopoietic transcription factor Gata2 network, upregulation of several receptor-like tyrosine kinases and overwhelming enrichment of inflammatory and Toll-like receptor (TLR) pathways. These result in hyperactivation of downstream signaling pathways including MEK/ERK and NFκB. These distinct mechanisms support the idea that *p53* missense mutations may confer unique properties in driving leukemogenesis in the context of oncogenic *Nras*. The distinct mechanisms in this animal model may yield novel therapeutic approaches for treating leukemia with both RAS pathway and TP53 mutations.

### 1.5 References


1. Harvey, J. J. "An unidentified virus which causes the rapid production of tumours in mice." Nature 204.4963 (1964): 1104-1105.
2. Kirsten, W. H., and Lo A. Mayer. "Morphologic responses to a murine erythroblastosis virus." *Journal of the National Cancer Institute* 39.2 (1967): 311-335.
3. Peters, R. L., et al. "Naturally occurring sarcoma virus of the BALB/cCr mouse." (1974).
4. Rasheed, Suraiya, Murray B. Gardner, and Robert J. Huebner. "In vitro isolation of stable rat sarcoma viruses." *Proceedings of the National Academy of Sciences* 75.6 (1978): 2972-2976.
5. Scolnick, Edward M., et al. "Studies on the nucleic acid sequences of Kirsten sarcoma virus: a model for formation of a mammalian RNA-containing sarcoma virus." *Journal of virology* 12.3 (1973): 458-463.
6. Hager, G. L., et al. "Molecular cloning of the Harvey sarcoma virus closed circular DNA intermediates: initial structural and biological characterization." *Journal of virology* 31.3 (1979): 795-809.
7. Tsuchida, Nobuo, and Seiichiro Uesugi. "Structure and functions of the Kirsten murine sarcoma virus genome: molecular cloning of biologically active Kirsten murine sarcoma virus DNA." *Journal of virology* 38.2 (1981): 720-727.
8. Wennerberg, Krister, Kent L. Rossman, and Channing J. Der. "The Ras superfamily at a glance." *Journal of cell science* 118.5 (2005): 843-846.
9. Colicelli, John. "Human RAS superfamily proteins and related GTPases." *Science's STKE* 2004.250 (2004): re13-re13.
10. Vetter, Ingrid R., and Alfred Wittinghofer. "The guanine nucleotide-binding switch in three dimensions." *Science* 294.5545 (2001): 1299-1304.
11. Bos, Johannes L., Holger Rehmann, and Alfred Wittinghofer. "GEFs and GAPs: critical elements in the control of small G proteins." *Cell* 129.5 (2007): 865-877.
12. Boriack-Sjodin, P. Ann, et al. "The structural basis of the activation of Ras by Sos." *Nature* 394.6691 (1998): 337-343.
13. Scheffzek, Klaus, et al. "The Ras-RasGAP complex: structural basis for GTPase activation and its loss in oncogenic Ras mutants." *Science* 277.5324 (1997): 333-339.
14. Cox, Adrienne D., and Channing J. Der. "Ras history: The saga continues." *Small GTPases* 1.1 (2010): 2-27.
15. Bar-Sagi, Dafna. "A Ras by any other name." *Molecular and cellular biology* 21.5 (2001): 1441-1443.

16. Schubbert, Suzanne, Kevin Shannon, and Gideon Bollag. "Hyperactive Ras in developmental disorders and cancer." *Nature Reviews Cancer* 7.4 (2007): 295-308.
17. Hancock, John F. "Ras proteins: different signals from different locations." *Nature reviews Molecular cell biology* 4.5 (2003): 373-385.
18. Goswami, Debanjan, et al. "Membrane interactions of the globular domain and the hypervariable region of KRAS4b define its unique diffusion behavior." Elife 9 (2020): e47654.
19. Inouye, Kaoru, et al. "Formation of the Ras dimer is essential for Raf-1 activation." *Journal of Biological Chemistry* 275.6 (2000): 3737-3740.
20. Prior, Ian A., et al. "Direct visualization of Ras proteins in spatially distinct cell surface microdomains." *The Journal of cell biology* 160.2 (2003): 165-170.
21. Plowman, Sarah J., et al. "H-ras, K-ras, and inner plasma membrane raft proteins operate in nanoclusters with differential dependence on the actin cytoskeleton." *Proceedings of the National Academy of Sciences* 102.43 (2005): 15500-15505.
22. Abankwa, Daniel, et al. "Ras membrane orientation and nanodomain localization generate isoform diversity." *Proceedings of the National Academy of Sciences* 107.3 (2010): 1130-1135.
23. Rocks, Oliver, et al. "An acylation cycle regulates localization and activity of palmitoylated Ras isoforms." *Science* 307.5716 (2005): 1746-1752.
24. Kim, Edward, et al. "Disruption of the mouse Rce1 gene results in defective Ras processing and mislocalization of Ras within cells." *Journal of Biological Chemistry* 274.13 (1999): 8383-8390.
25. Gimple, Ryan C., and Xiuxing Wang. "RAS: striking at the core of the oncogenic circuitry." *Frontiers in oncology* 9 (2019): 965.
26. Buday, László, and Julian Downward. "Epidermal growth factor regulates p21ras through the formation of a complex of receptor, Grb2 adapter protein, and Sos nucleotide exchange factor." *Cell* 73.3 (1993): 611-620.
27. Scaltriti, Maurizio, and José Baselga. "The epidermal growth factor receptor pathway: a model for targeted therapy." *Clinical cancer research* 12.18 (2006): 5268-5272.
28. Lowenstein, E. J., et al. "The SH2 and SH3 domain-containing protein GRB2 links receptor tyrosine kinases to ras signaling." *Cell* 70.3 (1992): 431-442.
29. Quilliam, Lawrence A., John F. Rebhun, and Ariel F. Castro. "A growing family of guanine nucleotide exchange factors is responsible for activation of Ras-family GTPases." (2002): 391-444.

30. Mitin, Natalia, Kent L. Rossman, and Channing J. Der. "Signaling interplay in Ras superfamily function." *Current Biology* 15.14 (2005): R563-R574.
31. Buday, László, and Julian Downward. "Many faces of Ras activation." *Biochimica et Biophysica Acta (BBA)-Reviews on Cancer* 1786.2 (2008): 178-187.
32. Crespo, P., and J. Leon. "Ras proteins in the control of the cell cycle and cell differentiation." *Cellular and Molecular Life Sciences CMLS* 57.11 (2000): 1613-1636.
33. Ying, Haoqiang, et al. "Oncogenic Kras maintains pancreatic tumors through regulation of anabolic glucose metabolism." *Cell* 149.3 (2012): 656-670.
34. Cox, Adrienne D., and Channing J. Der. "The dark side of Ras: regulation of apoptosis." *Oncogene* 22.56 (2003): 8999-9006.
35. Shields, Janiel M., et al. "Understanding Ras:'it ain't over'til it's over'." *Trends in cell biology* 10.4 (2000): 147-154.
36. McCubrey, James A., et al. "Roles of the Raf/MEK/ERK pathway in cell growth, malignant transformation and drug resistance." *Biochimica et Biophysica Acta (BBA)-Molecular Cell Research* 1773.8 (2007): 1263-1284.
37. Steelman, L. S., et al. "Roles of the Ras/Raf/MEK/ERK pathway in leukemia therapy." *Leukemia* 25.7 (2011): 1080-1094.
38. Xing, Jun, David D. Ginty, and Michael E. Greenberg. "Coupling of the RAS-MAPK pathway to gene activation by RSK2, a growth factor-regulated CREB kinase." *Science* 273.5277 (1996): 959-963.
39. Zhang, Wei, and Hui Tu Liu. "MAPK signal pathways in the regulation of cell proliferation in mammalian cells." *Cell research* 12.1 (2002): 9-18.
40. Yordy, John S., and Robin C. Muise-Helmericks. "Signal transduction and the Ets family of transcription factors." *Oncogene* 19.55 (2000): 6503-6513.
41. Dougherty, Michele K., et al. "Regulation of Raf-1 by direct feedback phosphorylation." *Molecular cell* 17.2 (2005): 215-224.
42. Brummer, Tilman, et al. "Identification of novel ERK-mediated feedback phosphorylation sites at the C-terminus of B-Raf." *Oncogene* 22.55 (2003): 8823-8834.
43. Chen, Dong, et al. "SOS phosphorylation and disassociation of the Grb2-SOS complex by the ERK and JNK signaling pathways." *Journal of Biological Chemistry* 271.11 (1996): 6328-6332.
44. Castellano, Esther, and Julian Downward. "RAS interaction with PI3K: more than just another effector pathway." *Genes & cancer* 2.3 (2011): 261-274.

45. Polak, Roel, and Miranda Buitenhuis. "The PI3K/PKB signaling module as key regulator of hematopoiesis: implications for therapeutic strategies in leukemia." *Blood, The Journal of the American Society of Hematology* 119.4 (2012): 911-923.
46. Cully, Megan, et al. "Beyond PTEN mutations: the PI3K pathway as an integrator of multiple inputs during tumorigenesis." *Nature Reviews Cancer* 6.3 (2006): 184-192.
47. Scheid, Michael P., and James R. Woodgett. "PKB/AKT: functional insights from genetic models." *Nature reviews Molecular cell biology* 2.10 (2001): 760-768.
48. Datta, Sandeep Robert, Anne Brunet, and Michael E. Greenberg. "Cellular survival: a play in three Akts." *Genes & development* 13.22 (1999): 2905-2927.
49. Manning, Brendan D., and Lewis C. Cantley. "AKT/PKB signaling: navigating downstream." *Cell* 129.7 (2007): 1261-1274.
50. Cantley, Lewis C. "The phosphoinositide 3-kinase pathway." *Science* 296.5573 (2002): 1655-1657.
51. Chien, Yuchen, and Michael A. White. "RAL GTPases are linchpin modulators of human tumour-cell proliferation and survival." *EMBO reports* 4.8 (2003): 800-806.
52. Rajalingam, Krishnaraj, et al. "Ras oncogenes and their downstream targets." *Biochimica et Biophysica Acta (BBA)-Molecular Cell Research* 1773.8 (2007): 1177-1195.
53. Rieger, Michael A., and Timm Schroeder. "Hematopoiesis." *Cold Spring Harbor perspectives in biology* 4.12 (2012): a008250.
54. Lin, Kuanyin K., and Magaret A. Goodell. "Detection of hematopoietic stem cells by flow cytometry." *Methods in cell biology* 103 (2011): 21-30.
55. Johnson L, et al. K-ras is an essential gene in the mouse with partial functional overlap with N-ras. Genes Dev. 1997;11:2468–81.
56. Esteban, Luis M., et al. "Targeted genomic disruption of H-ras and N-ras, individually or in combination, reveals the dispensability of both loci for mouse growth and development." *Molecular and cellular biology* 21.5 (2001): 1444-1452.
57. Umanoff H, et al. The murine N-ras gene is not essential for growth and development. Proc Natl Acad Sci USA. 1995;92(5):1709–13.
58. Iborra, Salvador, et al. "H-ras and N-ras are dispensable for T-cell development and activation but critical for protective Th1 immunity." Blood, The Journal of the American Society of Hematology 117.19 (2011): 5102-5111.
59. Perez de Castro, I., et al., Mice deficient for N-ras: impaired antiviral immune response and T-cell function. Cancer Research, 2003. 63(7): p. 1615-22.

60. Iborra, Salvador, et al. "N-ras couples antigen receptor signaling to Eomesodermin and to functional CD8+ T cell memory but not to effector differentiation." Journal of Experimental Medicine 210.7 (2013): 1463-1479.
61. Chen, Yuhong, et al. "Kras is critical for B cell lymphopoiesis." The Journal of Immunology 196.4 (2016): 1678-1685.
62. Hara, Takahiko, and Atsushi Miyajima. "Function and signal transduction mediated by the interleukin 3 receptor system in hematopoiesis." Stem Cells 14.6 (1996): 605-618.
63. Damnernsawad, Alisa, et al. "Kras is required for adult hematopoiesis." Stem Cells 34.7 (2016): 1859-1871.
64. Braun, Benjamin S., and Kevin Shannon. "Targeting Ras in myeloid leukemias." Clinical Cancer Research 14.8 (2008): 2249-2252.
65. Cancer Genome Atlas Network. "Comprehensive molecular characterization of human colon and rectal cancer." Nature 487.7407 (2012): 330.
66. Akbani, Rehan, et al. "Genomic classification of cutaneous melanoma." Cell 161.7 (2015): 1681-1696.
67. Cancer Genome Atlas Research Network. "Comprehensive molecular profiling of lung adenocarcinoma." Nature 511.7511 (2014): 543.
68. Raphael, Benjamin J., et al. "Integrated genomic characterization of pancreatic ductal adenocarcinoma." Cancer cell 32.2 (2017): 185-203.
69. Cox, Adrienne D., et al. "Drugging the undruggable RAS: mission possible?." Nature reviews Drug discovery 13.11 (2014): 828-851.
70. Prior, Ian A., Paul D. Lewis, and Carla Mattos. "A comprehensive survey of Ras mutations in cancer." Cancer research 72.10 (2012): 2457-2467.
71. Ward, Ashley F., Benjamin S. Braun, and Kevin M. Shannon. "Targeting oncogenic Ras signaling in hematologic malignancies." Blood, The Journal of the American Society of Hematology 120.17 (2012): 3397-3406.
72. Chng, W. J., et al. "Clinical and biological significance of RAS mutations in multiple myeloma." Leukemia 22.12 (2008): 2280-2284.
73. Lohr, Jens G., et al. "Widespread genetic heterogeneity in multiple myeloma: implications for targeted therapy." Cancer cell 25.1 (2014): 91-101.
74. Hunter, John C., et al. "Biochemical and structural analysis of common cancer-associated KRAS mutations." Molecular cancer research 13.9 (2015): 1325-1335.
75. Moore, Amanda R., et al. "RAS-targeted therapies: is the undruggable drugged?." Nature Reviews Drug Discovery 19.8 (2020): 533-552.

76. Kong, Guangyao, et al. "The ability of endogenous Nras oncogenes to initiate leukemia is codon-dependent." Leukemia 30.9 (2016): 1935-1938.
77. Zhang, Jingfang, et al. "p53−/− synergizes with enhanced Nras G12D signaling to transform megakaryocyte-erythroid progenitors in acute myeloid leukemia." Blood, The Journal of the American Society of Hematology 129.3 (2017): 358-370.
78. Wen, Zhi, et al. "Expression of NrasQ61R and MYC transgene in germinal center B cells induces a highly malignant multiple myeloma in mice." Blood 137.1 (2021): 61-74.
79. Simanshu, Dhirendra K., Dwight V. Nissley, and Frank McCormick. "RAS proteins and their regulators in human disease." Cell 170.1 (2017): 17-33.
80. Zhang, Jing, and Harvey F. Lodish. "Identification of K-ras as the major regulator for cytokine-dependent Akt activation in erythroid progenitors in vivo." Proceedings of the National Academy of Sciences 102.41 (2005): 14605-14610.
81. Luo, Lan, et al. "Kras-deficient T cells attenuate graft-versus-host disease but retain graft-versus-leukemia activity." The Journal of Immunology 205.12 (2020): 3480-3490.
82. Prior, Ian A., Fiona E. Hood, and James L. Hartley. "The frequency of Ras mutations in cancer." Cancer research 80.14 (2020): 2969-2974.

# Chapter 2

# Expression of *Nras*$^{Q61R}$ and *MYC* transgene in germinal center B cells induces a highly malignant multiple myeloma in mice

This chapter has been published as: Wen, Zhi[#], Rajagopalan, Adhithi[#] et al. "Expression of *Nras*$^{Q61R}$ and *MYC* transgene in germinal center B cells induces a highly malignant multiple myeloma in mice." Blood, The Journal of the American Society of Hematology 137.1 (2021): 61-74. (# indicates equal contribution)

## 2.1 Abstract

NRAS Q61 mutations are prevalent in advanced/relapsed multiple myeloma (MM) and correlate with poor patient outcomes. Thus, we generated a novel MM model by conditionally activating expression of endogenous NrasQ61R and a MYC transgene in germinal center B cells (VQ mice). VQ mice developed a highly malignant MM characterized by high proliferation index, hyperactivation of ERK and AKT signaling, impaired hematopoiesis, widespread extramedullary disease, bone lesions, kidney abnormalities, preserved PD1 and TIGIT immune checkpoint pathways, and expression of human high-risk MM gene signatures. VQ MM mice recapitulate most of the biological and clinical features of human advanced/high-risk MM. These MM phenotypes are serially transplantable in syngeneic recipients. Two MM cell lines were also derived to facilitate future genetic manipulations. Combination therapies based on MEK inhibition significantly prolonged the survival of VQ mice with advanced stage MM. Our study provides a strong rationale to develop MEK inhibition-based therapies for treating advanced/relapsed MM.

## 2.2 Introduction

Multiple myeloma (MM), a tumor of mature plasma B cells that produce antibodies (1), ranks as the second most common blood malignancy in the United States with an estimated 32,270 new cases in 2020 (https://www.cancer.org). Myeloma incidence has been steadily growing in both males and females since the mid-70's worldwide (SEER statistics and 2). With the introduction of "novel agents" to MM treatment, including proteasome inhibitors, immunomodulatory agents, and therapeutic antibodies, MM patient survival has increased (5-year survival now exceeds 50%), and quality-of-life also has improved (3). Relapses are almost inevitable and clinical benefit becomes less durable with each successive regimen until ultimate demise from multi-drug resistant MM (4) and/or aggressive manifestations such as non-secretory MM, extramedullary disease, and plasma cell leukemia (5).

Aberrant MYC expression is an early molecular event that associates with progression from indolent MGUS (monoclonal gammopathy of undetermined significance) to overt MM (6,7). Consistent with this observation in humans, activation of a human MYC transgene in germinal center (GC) B cells induces a highly penetrant, indolent MM in Vκ*MYC mice (8). Extramedullary involvement occurs in ~30% of Vκ*MYC mice. Targeting MYC (e.g., through bromodomain inhibition) has been shown to confer significant benefit (9).

The infrequency of advanced MM in the Vκ*MYC model suggests that additional genetic mutations are required. Indeed, genomic analysis of Vκ*MYC myeloma tumors identified frequent aneuploidy and biallelic deletions of Rb1, Kdm6a or Cdkn2a (10). Large-scale sequencing analyses reveal key progression events that primarily drive the hyperactivation of the RAS/RAF/MEK/ERK pathway and secondarily the NFκB pathway (11-14). RAS pathway mutations collectively constitute more than 50% of advanced and relapsed MM cases 14 and are even more frequent in drug-resistant patients (72% 15). Here, we present the first genetically-engineered Ras; MYC-driven MM murine model (VQ mice). VQ mice recapitulate most of the biological and clinical features of human advanced/high-risk MM.

### 2.3 Materials and Methods

#### Mice

All mouse lines were maintained in a pure C57BL/6 genetic background (>N10). The Vκ*MYC, conditional oncogenic Nras (Nras Lox-stop-Lox (LSL) Q61R/+), and IgG1-Cre mice were described previously (8,16-18). CD45.1+ transplant recipients were purchased from Jackson Laboratory (stock # 002014) and bred at Biotron Animal Research Services facility, University of Wisconsin-Madison. All animal experiments were conducted in accordance with the Guide for the Care and Use of Laboratory Animals and approved by an Animal Care and Use Committee at

UW-Madison. The program is accredited by the Association for Assessment and Accreditation of Laboratory Animal Care.

*Nras*$^{LSL\ Q61R/+}$*; IgG1-Cre* (Q), *Vκ*MYC; IgG1-Cre* (V), and *Vκ*MYC; Nras*$^{LSL\ Q61R/+}$*; IgG1-Cre* (VQ) compound mice were generated. Genotyping of *Vκ*MYC*, *Nras* $^{LSL\ Q61R/+}$ and *IgG1-Cre* was performed as previously described [1-3]. To evaluate the recombination efficiency of the *Vκ*MYC* allele, a competitive PCR assay was performed using 50ng of genomic DNA and three primers (O1727, O1875, and O1728) at the ratio of 1:3:3. The primer sequences are: O1727 (AAGGTGAGAGGTAGGCAAAGG), O1875 (GATCTGCGTCGACTGGGATGTTGTATAATG ACTCC) and O1728 (TGTGTAGCCTAAGCTGGTTTGA). PCR program was: 95°C 2 min; 25 cycles of 95°C 40 sec, 60°C 40 sec, and 72°C 60 sec; 72 °C 5 min; and 4°C forever.

To boost IgG1-Cre expression, 6-7 weeks old control (*IgG1-Cre*), V, Q, and VQ mice were immunized intraperitoneally twice with 200 µl of NP-CGG (Biosearch Technologies, N-5055C-5) in Imject Alum (Thermo, 77161) every other week. The mixture was prepared as following: 100 µl of 1mg/ml NP-CGG in PBS was mixed with 100 µl of Imject Alum at room temperature for 30 minutes before immunization.

**Serum protein electrophoresis (SPEP)**

Mice were retro-orbitally bled with plain micro hematocrit tubes (Bris, ISO12772). Blood samples were spun in microtainer tubes (BD, 365967) at 2,000x g for 10 minutes to collect serum. Serum was loaded into Hydragel agarose gel (Sebia, 4140) and processed using the Hydrasys instrument (Sebia) following the manufacturer's instruction. The processed film was scanned and quantified with Sebia Hydragel analysis system.

**Complete blood count (CBC) and histopathology**

Peripheral blood samples were collected via retro-orbital bleeding and analyzed with Hemavet 950FS (Drew Scientific). Mouse tissues were fixed in 10% neutral buffered formalin (Sigma-

Aldrich) and further processed at the Experimental Pathology Laboratory of the University of Wisconsin Carbone Cancer Center.

**Flow cytometric analysis of hematopoietic tissues**

Flow cytometric analysis of surface antigens on hematopoietic cells was performed as previously described [4]. Stained cells were analyzed on a FACS Calibur, LSRII, or LSRII Fortessa (BD Biosciences). Directly conjugated antibodies specific for the following mouse surface antigens were purchased from eBioscience unless specified: CD138 (BioLegend, 281-2), B220 (RA3-6B2), CD19 (eBio1D3), BMCA (Miltenyi, 130108301), PD-L1 (10F.9G2), PD-L2 (122), CD155 (TX56), H2-D$^{b}$ (28-14-8), I-A/I-E (M5/114.15.2), TIGIT (BioLegend, 1G9), PD1 (BioLegend, 29F.1A12), CD4 (GK1.5), CD8 (53-6.7), CD45.2 (104), CD45.1 (A20), and Thy1.2 (53-2.1).

**Phospho-flow analysis of ERK1/2 and AKT signaling in CD138$^{+}$ cells**

Cells were starved in IMDM containing 1% Bovine Serum Albumin for 2 hours at 37°C prior to fixation with paraformaldehyde at a final concentration of 2% (16% ampoules; Electron Microscopy Sciences) for 10 minutes at 37ºC. Flow cytometric analyses of phospho-ERK1/2 (pERK) and pAKT levels in defined CD138$^{+}$ cells were performed as previously described [4]. pERK1/2 was detected using a primary antibody against pERK Thr202/Tyr204 (Cell signaling, 9101L) while pAKT was detected using a primary antibody against pAKT S473 (Cell signaling, 4060L). Both reactions were followed by APC-conjugated donkey anti-rabbit IgG secondary antibody (Jackson ImmunoResearch, 711-136-152). The stained cells were analyzed on a FACS Calibur, LSRII or LSRII Fortessa.

**Ki67 analysis of CD138$^{+}$ cells**

Ki67 analysis was performed essentially as previously described [5]. Briefly, $10\times10^{6}$ cells were labeled with B220 and CD138 as described above. The stained cells were fixed in paraformaldehyde at a final concentration of 2% in PBS containing 2% FBS for 10 minutes at

room temperature. After washing with PBS, fixed cells were permeabilized with 0.1% saponin containing 1:20 Ki67-FITC (BD Biosciences, 556026) for 45 minutes at room temperature. Finally, the cells were resuspended with 1 ng/ml DAPI (Life Technologies) in PBS containing 2% FBS for one hour before analysis on FACS Calibur, LSRII or LSRII Fortessa.

**Isotyping of serum antibodies**

Mouse serum was diluted at 1:100,000 with PBS containing 1% BSA. Isotyping of serum antibodies was performed using the IsoStrip™ Mouse Monoclonal Antibody Isotyping Kit (Sigma, 11493027001) following the manufacturer's instructions.

**Clonality analysis of myeloma cells**

Genomic DNAs were extracted from mouse tail tissues or sorted $CD138^{+}$ cells. The PCR analysis was performed using primers DSF, DQ52 and JH4 as previously described [6].

**X-ray imaging of hind limb bones**

Mice were anesthetized and posed in the imaging chamber of UltraFocus$^{XL}$ (Faxitron) to take high resolution X-ray images.

**Immunofluorescence**

Suspension cells were washed twice in PBS and spun on slides using the Cytospin 4 centrifuge (Thermo, A78300003). Immunofluorescence was performed as previously described [7] using rabbit anti-MYC antibody (1:200, Santa Cruz, sc-789), PE-conjugated Rat anti-mouse CD138 antibody (1:100, Biolegend, 281-2), Biotin-conjugated Donkey anti-rabbit IgG antibody (1:1,000, Fitzgerald, 43R-1448), and FITC-Streptavidin (1:400, BD, 554060). Slides were mounted using VECTASHIELD Mounting Medium with DAPI (Vector, H-1200). Images were collected with Nikon A1 confocal microscope.

**Transplantation of myeloma cells**

Donor cells were resuspended in 100 µl of PBS containing 2% mouse serum. Eight-fourteen weeks old CD45.1$^{+}$ recipient mice were sub-lethally irradiated at 4.0 Gy using an X-RAD 320 Irradiator (Precision X-Ray Inc.) and transplanted with various numbers of donor cells via intracardiac injection. Frequency of myeloma initiating cells was calculated using L-Calc™ Limiting Dilution Software Version 1.1 (STEMCELL Technologies).

**scRNA-Seq analysis**

CD138$^{+}$ B220$^{-}$ cells were sorted from age-matched control bone marrow (Con-BM) and VQ-D2 BM and lymph node (LN). scRNA-Seq was performed using the Illumina® Bio-Rad® Single-Cell Sequencing Solution, which consists of Bio-Rad's ddSEQ™ Single-Cell Isolator with Illumina's SureCell WTA 3' Library Prep Kit. The libraries were sequenced on an Illumina HiSeq2500 outputting paired-end 75bp reads in rapid run mode. The sequencing data were aligned to the Mus musculus MM10 genome and UMI sums for each gene/cell combination were quantified using the SureCell RNA Single-Cell Illumina BaseSpace app. Only cells passing the knee filter, a heuristic for determining real cells from background sequences, were retained for further analysis. Filtered barcode matrix files were imported into the Seurat v2.3.4 single cell analysis package [8] using R v3.5.2. Cells expressing fewer than 300 genes, cells with >7.5% contribution of mitochondrial genes, and genes expressed in fewer than 3 cells were filtered out. Gene expression values for each cell were log-normalized and scaled by a factor of 10,000 based on the number of UMIs in each cell. Cell cycle phase was predicted as described [9]. In order to prevent clusters from being biased by cell cycle status, cellular library size, and mitochondrial transcript content, gene expression values were scaled based on the number of UMIs in each cell, the cell mitochondrial transcript content, and the cell cycle score. Naïve clustering of the cells into sub-populations was then conducted using Seurat's implementation of a shared nearest neighbor (SNN) modularity optimization based clustering algorithm (Louvain's original algorithm

[10]) using the first 3 principle components separating the cells and a resolution value of 0.4. The sample populations were visualized using t-distributed stochastic neighbor embedding (tSNE) plots [11]. Differentially expressed genes between clusters or samples were determined using Wilcoxon rank sum tests and Bonferroni correction. Pre-ranked gene set enrichment analyses (GSEA) [12] using the average log2 fold-changes were conducted using gene sets from the Broad Institute's Molecular Signatures Database [13]. High-risk MM signature module scores were calculated for each cell using methods described in [9]. Of note, among the 70 human genes [14], only 63 mouse orthologs were found. To determine whether VQ and control plasma cells expressed this multiple myeloma signature at different level, Welch's t-test was conducted between these groups.

**Bulk RNA-Seq analysis**

Total RNAs were isolated from 50,000 sorted CD138$^{+}$ B220$^{-}$ CD45.2$^{+}$ bone marrow cells of WT (n=3), V (n=3), recipients of tVk12653 (n=2), VQ-D1 (n=2), VQ-D4 (n=1), and VQ-D5 (n=2) using RNeasy Micro Kit (Qiagen). RNA-Seq libraries were prepared using SMARTer® Stranded Total RNA-Seq Kit v1 - Pico Input Mammalian (Takara Bio USA/Clontech). Sequencing was performed on an Illumina HiSeq 4000 system at the NUSeq Core facility. Reads from each sample were aligned to the Mus musculus GRCm38.p6 genome using STAR v2.6.1d [15]. During alignment, the first three nucleotides (the switching oligonucleotides) were clipped from each read as recommended by Takara Bio USA/Clontech. Reads that aligned to the sense strand of genes within the Gencode release M24 genome annotation were then counted. Read counts for each sample were then imported into R v3.6.1 (https://www.R-project.org/) and normalized using DESeq2 v1.26.0 [16]. Wald tests within DESeq2 were conducted to assess differential gene expression between groups and the ashr method was used to shrink log2 fold-change values [17]. Pre-ranked GSEA was conducted using clusterProfiler v3.14.3 [18] using the Wald test statistics as the ranking values and the fgsea method. Gene sets from the Broad Institute's Molecular

Signatures Database [13], Gene Ontology [19,20], Reactome [21], C2 curated, and UAMS-70 [14] gene sets were used. P values from differential gene expression analyses and GSEA were corrected for multiple testing using the Benjamini-Hochberg method (https://mathscinet.ams.org/mathscinet-getitem?mr=1325392).

**Establishment of multiple myeloma cell lines-4935 and 4938**

Total bone marrow cells were harvested from moribund VQ-D2 recipient mice and rinsed in ice-cold PBS containing antibiotics (GIBCO, 15140122). The cells were resuspended in IMDM containing 10% FBS, 1X antibiotics, and 10ng/ml human recombinant IL6 (PeproTech, 200-06) and continuously cultured at 37℃.

**Retroviral and lentiviral infection of established MM cell lines**

pMSCV-IRES-GFP and pCL-Eco (for retrovirus) and pGIPZ, MD2G and PAX2 (for lentivrus) were transfected into HEK293T cells using TransIT-LT1 (Mirus) following the manufacturer's instruction. Two days after transfection, the supernatant containing packaged virus was harvested and filtered with the 0.45 μM filtration unit.

4935 or 4938 cells were passaged 48 hours before infection. 0.5-1x$10^6$ cells were seeded in 6-well plate and mixed with 1ml of viral suspension medium containing 4-8 ng/ml polybrene. After spinning at 2000x g at 22℃ for 1-2 hours, the cells were supplemented with 1.5ml of IMDM containing 10% FBS, antibiotics, and 10ng/ml hIL6 (PeproTech) (final concentration). The cells were continuously cultured at 37℃ and 5% $CO_2$ for 48 hours and GFP expression was measured using flow cytometry on LSRII or LSRII Fortessa (BD Biosciences).

**Immunoblotting**

Immunoblotting analyses for various proteins were performed essentially as described in [22]. The membrane transfer was carried out with Bio-Rad Trans-Blot® Turbo™ Transfer System and the images were taken with ImageQuant LAS4000 imager (GE Product, 28-9558-10). The following

primary and secondary antibodies were used: anti-MYC antibody (Santa Cruz, sc-789), anti-β-actin (Santa Cruz, sc-1616R), Biotin-conjugated donkey anti-rabbit IgG antibody (Fitzgerald, 43R-1448), HRP-Streptavidin (Biocare, HP604) and HRP-conjugated anti-HA antibody (Roche, 12013819001).

**Small compound treatment**

Total bone marrow cells were harvested from three moribund VQ-D1 recipients and mixed equally. Approximately $5x10^6$ cells were transplanted into individual sub-lethally irradiated $CD45.1^+$ recipients as described above. Eight weeks after transplantation, the recipient mice were bled for SPEP analysis and randomly divided into 4 groups: vehicle, 25mg/kg of AZD6244 (Chemitek) twice a day for 21 days *via* oral gavage, 1mg/kg of bortezomib (Chemitek) once a day on Day 1, 4, 8, and 11 *via* IP injection, and combined AZD6244 and bortezomib. SPEP analysis was performed at a moribund stage or at day 28. The mice were closely monitored until a moribund stage.

For the trametinib and GSK525762 treatment, trametinib (Chemitek) was dissolved in 0.5% hydroxypropylmethylcellulose (Sigma) and 0.2% Tween-80 (Sigma) in distilled water (pH 8.0) and given orally at 0.25mg/kg every morning. GSK525762 (Chemitek) was dissolved in 1% methylcellulose (Sigma) containing 0.2% SDS and given orally at 15mg/kg every afternoon. The treatment lasted until the mice reached a moribund stage.

**Statistics**

For Kaplan–Meier survival curves, survival differences between groups were assessed with the log-rank test, assuming significance at $p<0.05$. Unpaired two-tailed Student's *t*-tests were used to determine the significance between two data sets unless specified, assuming significance at $p<0.05$.

## 2.4 Results

### Generation of an oncogenic Nras; MYC-driven multiple myeloma model

Mutations in RAS pathway genes (NRAS, KRAS, and BRAF) are rare in MGUS but collectively found in >50% of patients with advanced or relapsed multiple myeloma (MM) (11,13,14,19). We and others characterized multiple oncogenic Ras models, including KrasG12D/+ (20-22), NrasG12D/+ (23,24), NrasG12D/G12D (25,26), and NrasQ61R/+(27). When activated throughout the hematopoietic system using Mx1-Cre, we only observed B cell malignancies in a fraction of oncogenic Nras mice but never in oncogenic Kras mice (22,25,28). Moreover, unlike the prevalence of NRAS G12 and G13 mutations in myeloid diseases, NRAS Q61 mutations predominantly occur in MM 27 and have been reported to associate with MM poor prognosis (29). Therefore, we chose the NrasQ61R/+ allele 16 as the MM progression driver.

Chesi et al. reported that Vκ*MYC mice develop a highly penetrant, indolent MM (8), consistent with the role of dysregulated MYC expression in MM initiation (6). The Vκ*MYC allele includes multiple copies of Vκ*MYC transgene arranged in the head-to-tail order (8,10) (Fig. S1). Each copy contains an engineered stop codon at the third amino acid and a floxed 3' Kappa enhancer. The stop codons could be sporadically reverted by AID (Activation-induced cytidine deaminase) in germinal center (GC) B cells. The floxed 3' Kappa enhancer could be removed in the presence of Cre recombinase to downregulate MYC expression. Given that MYC activation signatures are overexpressed upon transition from MGUS to overt myeloma (30) and NRAS Q61 mutations are prevalent in the latter, we reasoned that the Vκ*MYC allele, when combined with the NrasQ61R/+ allele, may allow in vivo selection of myeloma initiating cells with appropriate level of MYC expression. The level of MYC expression may be critical as previous attempts utilizing an unfloxed Vκ*MYC allele in combination with various oncogenes almost invariably generated aggressive B cell lymphoma (Chesi, unpublished data), except for the extra-medullary MM noted in Vκ*MYC mice crossed with the Eμ-BCL2 allele (8).

We used IgG1-Cre (18) to drive NrasQ61R/+ expression and randomly select for hMYC expression levels in GC B cells (Fig. 1A). In addition to the Vκ*MYC; Nras LSL Q61R/+; IgG1-Cre (VQ) compound mice, we also generated Nras LSL Q61R/+; IgG1-Cre (Q), Vκ*MYC; IgG1-Cre (V) mice. IgG1-Cre mice served as control throughout the study. To boost IgG1-Cre expression, NP-CGG was used to immunize 6-7 weeks old mice. We closely monitored the control, Q, V, and VQ mice via regular serum protein electrophoresis (SPEP). A significant fraction of Q, V, and VQ mice developed an M-spike over time (Fig. 1B) and died pre-maturely (Fig. 1C). In the VQ cohort, 14/17 VQ mice developed a M-spike. Ultimately, four VQ mice were found dead and could not be evaluated. In the remaining 13 VQ mice, 8/13 died of a highly malignant MM, characterized by increased CD138+ B220- myeloma cells in bone marrow, spleen, and/or lymph node (>10%) and infiltration of myeloma cells to liver and kidney (Fig. 1D, S2A, 1E, and S6A). Immunoglobulin deposition in kidney (Fig. 1E) and rouleaux formation in peripheral blood (Fig. S2B) were also seen in some of the VQ MM mice. Associated with MM-like phenotypes, VQ mice showed impaired hematopoiesis typically seen in advanced MM patients, including anemia and thrombocytopenia (Fig. 1F). Isotyping of serum antibodies in 5 VQ MM mice demonstrated detectable kappa light chain in all mice along with IgG2b (B2518-VQ1), IgA and IgG3 (B2519-VQ2, B3518-VQ5, and B3520-VQ4), or lambda light chain (B2576-VQ3) (Table S1). Consistent with the isotyping results, our clonality analysis using a D-J rearrangement assay (31) showed that VQ1 myeloma had a single dominant clone while VQ2 myeloma was oligo-clonal (Fig. 1G). For the remaining 5/13 VQ mice, they either developed other lymphoid diseases (n=3) (e.g. B cell lymphoma in B2509) or died without a defined hematologic malignancy (n=2) (e.g. B3300) (Fig. 1C). Since both B2509 and B3300 showed a M-spike in SPEP analysis, we isotyped their serum samples; both were positive for kappa light chain, IgM and a few other IgGs (Table S1).

Based on our MM diagnostic criteria of >10% CD138+ B220- plasma cells in any hematopoietic tissues (bone marrow, spleen, and lymph node) plus evidence of end-organ damage, which is

analogous to the IMWG criteria, 1/13 V mice died with MM (Fig. 1C and Table S2) though most of them developed a M-spike at the moribund stage (Fig. 1B). In addition, 11/13 V mice developed non-MM lymphoid malignancies (including B cell lymphoma and non-MM plasmacytic diseases) based on presence of splenomegaly/lymphadenopathy, pathological evaluation, and flow cytometric analysis. The B cells from V mice with non-MM lymphoid malignancies were oligo clonal (Fig. S3). One out of 13 V mice died with a myeloproliferative neoplasm (MPN). The wide spectrum of malignancy phenotypes in V mice is not surprising, as the IgG1-Cre mediated recombination of the floxed kappa enhancer may perturb MYC expression to levels not optimal for myelomagenesis in the absence of a second molecular event (as corroborated by RNA-Seq analysis of hMYC level in Fig. 6A). We transplanted bone marrow cells from 3 V mice into sub-lethally irradiated recipients (Fig. S4). These donor mice developed either moderate MPN (V1) or plasma cell disease (V2 and V3) at the moribund stage (Fig. S4A-S4C). Currently, only one recipient developed a M spike and died after a prolonged latency (Fig. S4D and S4E). Taken together, our data indicate that V mice demonstrate distinct pathological phenotypes from the reported Vκ*MYC mice in which the transgene is not subject to Cre recombination/re-arrangement.

Of the Q mice, 1/7 died with MM and 6/7 died with either other lymphoid diseases (n=3, including lymphoma and non-MM lymphoplasmacytic diseases) or without a defined hematologic malignancy (n=3). The B cells in Q mice with other lymphoid diseases were also oligo clonal (Fig. S3). We further transplanted bone marrow or lymph node cells from 2 Q mice with a plasma cell disease (Fig. S5A-S5C) into secondary recipients. The Q-recipient mice showed inconsistent M-spikes (Fig. S5D) and lacked bone lesions upon X-ray imaging (Fig. S5E). They died within 15 months (Fig. S5F). Despite moderate plasmacytosis in lymph node (Fig. S5G), we did not observe plasma cell infiltration to liver or kidney and no kidney abnormality was detected in the recipients (Fig. S5H).

**Both ERK and AKT pathways are hyperactivated in VQ myeloma cells**

We characterized CD138+ B220- cells from VQ myeloma mice, in particular VQ1 and VQ2. Genotyping analysis demonstrated that Nras Q61R allele was fully activated in the myeloma cells, while Vκ*MYC allele was predominantly unrecombined (Fig. 2A). Expression of hMYC in myeloma cells was further validated using confocal immunofluorescence (Fig. 2B). Unlike the indolent Vκ*MYC cells 8, V and VQ plasma cells were highly proliferative (Fig. 2C). Similar to human advanced MM cells 32, both ERK and AKT pathways were hyperactivated in VQ MM cells (Fig. 2D and 2E). By contrast, Q and V plasma cells only showed moderate hyperactivation of ERK and AKT, respectively.

**VQ myeloma phenotypes are readily transplantable into syngeneic recipients**

We transplanted VQ MM cells from multiple hematopoietic tissues into sub-lethally irradiated syngeneic recipients (Fig. 3A and S6B). VQ1 myeloma cells were enriched primarily in bone marrow and secondarily in spleen, while VQ2 myeloma cells were localized primarily in lymph node and secondarily in bone marrow and spleen (Fig. 1D). Regardless of tissue origin, all the transplant recipients developed M-spike (5-6 weeks for VQ-D1 recipients and 2-3 weeks for VQ-D2 recipients) (Fig. 3B). VQ-D1 and VQ-D2 recipients died of malignant MM in 10-16 weeks and 3-5 weeks, respectively (Fig. 3C). Our data indicate an extramedullary myeloma disease in VQ1 spleen and VQ2 lymph node. Similarly, VQ-D4 and VQ-D5 recipients died of malignant MM in 7-9 weeks and 6-7 weeks, respectively (Fig. S6B). Clonality analysis showed that most of recipient mice had a dominant clone (Fig. S6C). X-ray imaging detected multiple osteolytic lesions in both VQ-D1 and VQ-D2 recipients (Fig. 3D). Not surprisingly, all of them suffered from hind-limb paralysis at the moribund stage (Fig. 3E). Flow cytometric analysis showed that VQ-D1 and VQ-D2 myeloma cells preserved their donor-characteristic tissue localization (Fig. 3F). Similar to their donor mice, myeloma cell infiltration was observed in liver and kidney (Fig. 3G). We did not detect surface expression of other B cell markers (e.g. CD19) (Fig. S7A). Similar as their donor myeloma

cells, VQ-D1 and VQ-D2 myeloma cells were hyperproliferative, to a greater degree than the transplantable Vκ*MYC MM cells (~35% in 33) (Fig. S7B). Associated with this high proliferation index, both ERK and AKT pathways were hyperactivated in VQ-D1 and VQ-D2 myeloma cells (Fig. S7C).

We continuously passaged VQ1 and VQ2 myeloma cells in vivo for 6 generations (Fig. S8A). All the VQ-D1 and VQ-D2 recipients developed M-spike at consistent time points and died of advanced MM as their corresponding donors. We also used cryopreserved myeloma cells for transplantation (Fig. S8B). Again, all the recipients developed MM-like phenotypes and died within a few weeks. We also transplanted cryopreserved VQ-D1 and -D2 cells into non-irradiated recipients (Fig. S8C). Interestingly, 5/5 VQ-D1 recipients died with a highly malignant MM within 11 weeks, while only 1/4 VQ-D2 recipients died with MM upon observation for up to 20 weeks.

To identify which population(s) of cells contain myeloma-initiating activities, we first determined the donor contribution in CD138+ B220-, CD138- B220+, and CD138- B220- cells (Fig. S9A). As expected, >95% of CD138+ B220- cells and >10% of CD138- B220- cells were donor-derived, while >99% of CD138- B220+ cells were derived from recipients (CD45.2-). Therefore, we fractionated VQ-D1 bone marrow cells (Fig. S9B) and VQ-D2 lymph node cells (Fig. S9C) into CD138+ B220- and CD138- B220- fractions and transplanted various numbers into sub-lethally irradiated recipients. Up to 3.5 million CD138- B220- cells failed to induce MM phenotypes (0/9), while as low as 500 CD138+ B220- cells induced MM in 100% of recipients (10/10). We calculated that the frequency of myeloma initiating cells was ~1/150-1/200 of CD138+ B220- cells, analogous to human myeloma (34).

**PD1 and TIGIT immune checkpoint pathways are preserved in the VQ MM model**

PD1 and TIGIT are major immune checkpoint pathways that mediate MM cells-induced T cell suppression in MM patients (35-37). Therefore, we surveyed the expression of multiple immune

checkpoint ligands in primary VQ-D1 and VQ-D2 CD138+ MM cells. Our data showed that >95% of VQ-D1 MM cells and ~59% of VQ-D2 MM cells expressed PD-L1, and ~50% of VQ-D1 MM cells and ~18% of VQ-D2 MM cells expressed CD155 (Fig. 4A). Expression of PD-L2 was not detectable on VQ-D1 and VQ-D2 MM cells. Moreover, >95% of VQ-D1 and VQ-D2 MM cells expressed MHC-I, but MHC-II was only expressed in a few MM cells (Fig. 4B). Corresponding to the PD-L1 and CD155 expression on MM cells, a fraction of CD8+ and CD4+ T cells in VQ-D1 and VQ-D2 recipient mice expressed the receptors, PD1 and TIGIT respectively (Fig. 4C and 4D). In VQ-D1 recipients, T cell compartment was only reduced in spleen, which was associated with a significant MM burden and increased PD1+ T cells (Fig. 4E). In VQ-D2 recipients, both TIGIT and PD1 appeared to be expressed in larger fraction of T cells than in control T cells (Fig. 4D). Correspondingly, we observed reduced T cell compartment in the spleen and lymph node of VQ-D2 recipients (Fig. 4F). Our data suggest that both PD1 and TIGIT pathways are preserved in VQ MM model.

**VQ myeloma cells display distinct transcriptional signatures from normal plasma cells and tVk12653 myeloma cells**

We investigated the molecular mechanisms underlying VQ myeloma using single-cell RNA-Seq (scRNA-Seq) analysis. CD138+ B220- cells were flow sorted from age-matched control bone marrow (BM) and VQ-D2 BM and lymph node (LN). Following removal of low-quality cells, a total of 749 single cells expressing >300 genes per cell were subjected to further analysis (Fig. S10A and S10B). The median number of genes detected in normal plasma cells was ~1,000 and in VQ MM cells was ~2,000. Cluster analysis of all these cells, visualized on a tSNE plot, yielded 5 distinct clusters (0-4) (Fig. 5A and Table S3). Consistent with the previous report (38), normal plasma cells fell into 2 distinct clusters (C2 and C4) (Fig. 5B). Based on the characteristic expression of genes associated with long-lived plasma cells (e.g. Prg2 and Slpi) vs short-lived plasma cells (e.g. CD93) (39), C2 and C4 may represent long- and short-lived plasma cells

respectively. In contrast, the majority of VQ MM cells, regardless of their tissue origins, grouped into 3 clusters distinct from normal plasma cells (C0, C1, and C3), reflecting the intratumor heterogeneity. As in human MM patients (38), the minor populations of myeloma cells in C2 and C4 likely represent the residual normal plasma cells derived from the host recipient. As expected, normal plasma cells were non-proliferative and predominantly in G1 phase, while MM cells from BM and LN were highly proliferative and mostly in G2/M or S phases (Fig. 5C). GSEA identified many pathways that were significantly enriched in VQ MM cells (P adjusted <0.25). Compared to normal plasma cells, VQ MM cells from BM were enriched for MYC and E2F target genes as well as genes involved in unfolded protein response pathway (Fig. 5D). In addition, VQ MM cells showed significant enrichment of many human MM gene signatures associated with poor prognosis in human MM patients (Fig. 5D and 5E) (40), including the high-risk MM signature (UAMS-70) (Table S4) acknowledged by the International Myeloma Workgroup at a significantly higher level than normal plasma cells (41). We also interrogated the high-risk MM gene signature, EMC-92 (42). Unfortunately, more than half of the genes were not detected in control and VQ plasma cells. Interestingly, while VQ MM cells from BM and LN were largely clustered together, GSEA revealed that they displayed distinct transcriptional profiles in cell metabolism and epithelial-mesenchymal transition (Fig. S10C).

To validate our scRNA-Seq data, we performed bulk RNA-Seq using CD138+ B220- BM cells sorted from WT (n=3), V (n=3), tVk12653 (a transplantable Vκ*MYC line reported in 33, n=2), and VQ recipient mice (n=5 from 3 donor lines) (Fig. 6). Although Myc transcript levels in V (mean FPKM: 134) and VQ cells (mean FPKM: 279-579) were higher than that in WT cells (mean FPKM: 20), they were much lower than that in tVk12653 cells (mean FPKM: 2939) (Fig. 6A). Notably, ~99% of Myc transcripts in V, VQ, and tVk12653 cells are human MYC. Excluding immunoglobin genes, we found that the transcriptome of V cells was essentially identical as that of WT cells, while VQ and tVk12653 transcriptomes were distinct from WT transcriptome (Fig. 6B). Compared

to WT cells, we identified a total of 3,091 and 2,654 genes differentially expressed in VQ and tVk12653 cells respectively (FDR < 0.05 and fold change > 2) (Fig. 6C). Consistent with our scRNA-Seq data, GSEA showed that MYC and E2F targets and genes involved in the unfolded-protein response pathway were enriched in VQ MM cells (Fig. 6D). By contrast, only MYC and E2F targets were enriched in tVk12653 MM cells. Importantly, UAMS-70 high-risk MM gene signature was significantly enriched in VQ cells but not in tVk12653 cells (Fig. 6E), while EMC-92 gene signature was not enriched in either type of MM cells (Fig. S11). To understand the molecular differences of VQ vs tVk12653 MM cells, we directly compared their transcriptomes. We identified a total of 1,217 genes differentially expressed in VQ cells (FDR < 0.05 and fold change > 2) (Fig. 6F), 727 genes up-regulated and 490 genes down-regulated. Despite higher hMYC levels in tVk12653 MM cells, MYC target gene signatures were more significantly enriched in VQ cells (P adjusted <0.25) (Fig. 6G), suggesting a prominent synergism between Nras Q61R signaling and hMYC. Consistent with our results described above, E2F targets and genes involved in the unfolded-protein response pathway were also more enriched in VQ MM cells (P adjusted <0.25) (Fig. 6G). These molecular changes associated with enrichment of RAS/ERK signaling signatures in VQ cells (P adjusted <0.25) (Fig. 6H). Our data demonstrate that Nras Q61R signaling plays an important role in driving high-risk VQ MM development.

**VQ MM cell lines enable further genetic manipulations**

To facilitate further genetic manipulations and drug screening/testing in VQ MM model, we established two VQ MM cell lines, 4935 and 4938, from 2 independent VQ-D2 recipients (Fig. 7A). Both cell lines showed MM-characteristic morphologies (Fig. 7B) and displayed CD138+ B220- immunophenotype (Fig. 7C). As their donor VQ2 MM cells, the Nras Q61R allele was fully activated in both cell lines, while the Vκ*MYC allele was predominantly unrecombined (Fig. 7D). hMYC was readily detectable in these cells (Fig. 7E and 7F) and they divided approximately once per day. Above 95% of cells co-expressed PD-L1 and CD155 (Fig. 7G). About 80% of 4935 and

4938 cells expressed high levels of MHC-I but neither of the cell lines expressed MHC-II (Fig. 7H). More importantly, both cell lines were easily infectible by retrovirus and lentivirus (Fig. 7I), making further genetic modifications feasible in these cell lines.

**MEK inhibition-based combination therapies attenuate MM phenotypes and prolong the survival of VQ recipients**

We further tested if VQ MM model can be used as a preclinical platform for evaluating established and potentially novel therapeutic agents. We treated VQ MM cell lines with AZD6244 (a potent MEK inhibitor (28)) (Fig. S12A) or bortezomib (a proteasome inhibitor commonly used in human MM treatment) (Fig. S12B). Both agents induced a dose-dependent inhibition of MM cell growth with IC50 at 1-10 □M (AZD6244) and 15-20 nM (bortezomib). The IC50 of bortezomib in VQ MM cell lines is notably higher than its IC50 for growth inhibition of bortezomib-sensitive human MM cell lines (<10 nM) (43), suggesting that VQ MM cells may show de novo resistance to bortezomib. To determine the effects of AZD6244 and bortezomib on MM development in vivo, we transplanted primary VQ-D1 MM cells into sub-lethally irradiated recipients (Fig. S12C). Once advanced MM was established as indicated by a high γ-globulin: Albumin (γ/A) ratio (average: 0.6-0.8), the mice were divided into 4 groups with comparable ratios and treated with vehicle, bortezomib alone, AZD6244 alone, or combined bortezomib and AZD6244 for 21 days. SPEP analysis was performed at day 28 or at a moribund stage before day 28. Our data showed that compared to vehicle-treated mice, combinatorial treatment of AZD6244 and bortezomib ameliorated MM phenotypes, including stabilizing γ/A ratio (average: 0.7) (Fig. S12D), and elevated red blood cell and platelet counts (Fig. S12E). Moreover, bortezomib/AZD6244 treatment prolonged the survival of VQ recipients (Fig. S12F). The effects of combination therapy tended to be better than single agent alone.

Encouraged by these results, we switched to trametinib, the MEK inhibitor approved by FDA for treating melanoma (44). Trametinib displayed a more potent inhibition of VQ MM cell growth in

vitro (IC50: 5-10 nM) (Fig. 7J). Moreover, upon trametinib treatment, surface-expression of PD-L1 was significantly reduced while CD155 expression was not changed (Fig. 7K). Because targeting MYC via bromodomain inhibition confers significant anti-myeloma benefit (9), we also tested GSK525762, a pan-BET (bromodomain and extra-terminal domain) inhibitor currently under clinical development (45,46). GSK525762 showed a moderate inhibition of MM cell growth in vitro (IC50: ~3 μM) (Fig. 7L) and had no effects on PD-L1 and CD155 surface expression in MM cells (Fig. 7M). Given a much better anti-leukemia effect of GSK525762 in vivo than in vitro (You, unpublished data), we moved forward to the in vivo study. We transplanted primary VQ-D1 MM cells into sub-lethally irradiated recipients. Upon development of an advanced MM characterized by a high γ/A ratio (average: ~0.5) (Fig. 7N), the mice were divided into 4 groups as described above and treated with vehicle, trametinib, GSK525762, or combined trametinib and GSK525762 until a moribund stage. SPEP analysis was performed at day 21 or at a moribund stage before day 21. Vehicle- or GSK525762-treated mice died within 6 weeks, while trametinib treatment significantly prolonged the survival of diseased mice (Fig. 7O). Combinatorial drug treatment outperformed both single agent treatments (Fig. 7N and 7O). Our results corroborate the clinical success of using trametinib in combination therapy regimens for some patients with advanced MM (47), suggesting that VQ MM model may serve as a robust platform for pre-clinical studies of therapeutic agents with novel modes of action.

**2.5 Discussion**

Activating mutations of RAS pathway genes constitute the most frequent genetic event in advanced and refractory MM. Here, we describe the first genetically-engineered Ras; MYC-driven model for advanced MM. This model displays many biological and clinical features characteristic for human advanced MM and thus provides a platform to investigate MM progression in vivo and evaluate potential therapeutic agents.

**KRAS mutations vs NRAS mutations in MM**

Despite the high degree of sequence identity between Kras and Nras proteins (>80%), we and others observed that oncogenic Kras is a much more potent oncogene than oncogenic Nras in myeloid diseases, demonstrated by earlier disease onset, more severe phenotypes, and shorter survival in KrasG12D/+ mice compared to NrasG12D/+, NrasG12D/G12D, and NrasQ61R/+ mice (reviewed in 48). Interestingly, when activated throughout the hematopoietic system, KrasG12D/+ mice never developed B cell malignancies while a fraction of oncogenic Nras mice did (22,28,49). One possibility could be that strong oncogenic Kras signaling is less favorable than oncogenic Nras in B cells. In human MM, KRAS and NRAS mutation frequencies are approximately equal (11,13,14). However, NRAS mutations occur in untreated advanced patients and relapsed patients at a 50:50 ratio, while ~2/3 KRAS mutations are acquired in relapsed patients, suggesting that NRAS signaling may be equally important in MM progression and drug resistance while KRAS signaling may be more involved in drug resistance.

Although mutations at codons G12, G13, and Q61 of RAS are all perceived oncogenic equivalents, they display distinct biochemical and functional properties. RAS G12 and G13 mutations affect the GTPase activity of RAS protein by preventing proper position of the RAS-GTPase activation protein arginine finger within the catalytic site, while Q61 mutations lead to more severe impairment of RAS intrinsic GTPase function (50). Therefore, G12 and G13 mutations are less activating than Q61 mutations. Not surprisingly, we and others found that the oncogenic activity of Nras is codon-dependent (16,27). Corroborating the mouse results, in human hematologic malignancies with NRAS mutations, G12 mutations are prevalent in myeloid leukemia, while Q61 mutations are predominant in MM (~75%) (27). In contrast, the codon preference in the KRAS gene is much less prominent. In MM patients with KRAS mutations, both codons G12 and Q61 are hot spots with an equal mutation rate based on MMRF data base (G12: 39% and Q61: 37%) and COSMIC data base (G12: 32% and Q61: 36%). Equal mutation rates

on KRAS G12 and Q61 may be due to the unique capability of KrasG12D, but not oncogenic Nras, to cross-activate WT Ras via Sos1, a Ras guanine nucleotide exchange factor (51), leading to a more potent hyperactivation of MEK/ERK than KrasG12D alone. This process could minimize the functional difference between KRAS G12 and Q61 mutations.

**Functional contribution of NrasQ61R to the VQ model**

Compared to the de novo Vκ*MYC model, which reflects a more indolent, less proliferative MM, VQ MM model shares similar developmental origins but displays distinct and more diversified antibody isotypes (8 and Table S1); VQ cells display several non-IgM isotypes, whereas Vκ*MYC cells are predominantly of IgG1 isotype. Of note, in all 3 VQ mice with both IgG and IgA clones, IgA clone became dominant upon transplantation and VQ-D2 cell lines were also derived from IgA clone (Table S1). The various isotypes in VQ model may reflect the demonstrated expression of Cre recombinase in non-IgG switched plasma cells from IgG-Cre transgene (18). VQ survival is significantly shorter than that of de novo Vκ*MYC mice (Fig. 3C), while VQ transplant recipients have a comparable survival to that of selected bortezomib-resistant Vκ*MYC lines (33). In contrast to Vκ*MYC and Vκ*MYC-derived transplantable lines, VQ2-derived MM cells were readily propagated in vitro and were efficiently infectible by standard lentiviral and retroviral vectors (Fig. 7A-7C).

We believe that NrasQ61R expression drives progression from the indolent Vκ*MYC model to the advanced, high-risk VQ model through hyperactivation of MEK/ERK pathway (27 and Fig. 2D and S7C), promoting MM hyperproliferation (Fig. 2C and S7B), upregulating MYC and E2F target genes (Fig. 5D, 6D, and 6G) and PD-L1 (Fig. 4A and 7M), and resulting in more resistance to bortezomib than the original Vκ*MYC mice (33) (Fig S12B and S12F). Consistent with this idea, NRAS Q61 mutations are significantly associated with bortezomib resistance in human MM patients (42).

## 2.6 Figures and Legends

**Figure 2-1. A fraction of NrasQ61R/+; Vκ*MYC mice develop multiple myeloma.** (A) Acronym of transgenic mouse lines and illustration of IgG1-Cre induction scheme. (B) Serum protein electrophoresis was performed on representative mice from each group serially bled at the indicated weeks. The brackets show the γ-globulin component of the serum. (C) Kaplan-Meier survival curves (left) and disease incidences (right) of different groups of animals. MM is defined as CD138+ B220- cells being >10% in bone marrow, spleen, and/or lymph node along with end-organ abnormalities. (D) Flow cytometric analysis of B220 and CD138 expression on cells from bone marrow (BM), spleen (SP) and lymph node (LN). Representative density plots from each group are shown. (E) Representative images of H&E stained BM, SP, liver, LN, and kidney sections. Red arrow indicates an area with protein deposition mimicking the histologic findings in myeloma kidney. (F) Complete Blood Count (CBC) of peripheral blood samples collected from moribund mice and age-matched control mice. WBC, white blood cell; RBC, red blood cell; Hb, hemoglobin. ns, not significant. (G) Clonality analysis of VQ1 and VQ2 CD138+ cells using DJH recombination PCR assay. *, $p<0.05$; **, $p<0.01$; ***, $p<0.001$.

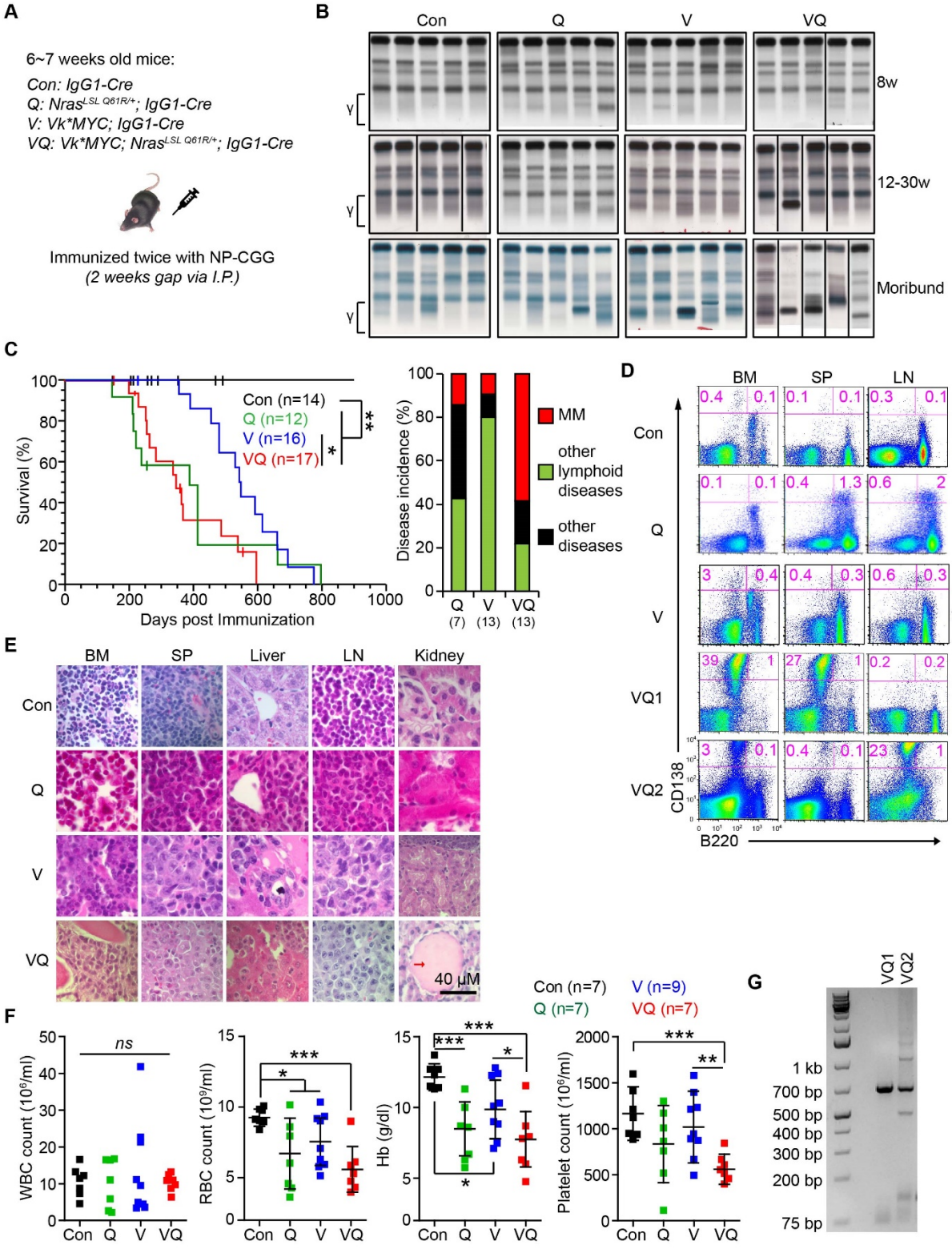
A
6~7 weeks old mice:
Con: IgG1-Cre
Q: Nras LSL Q61R/+; IgG1-Cre
V: Vk*MYC; IgG1-Cre
VQ: Vk*MYC; Nras LSL Q61R/+; IgG1-Cre
Immunized twice with NP-CGG
(2 weeks gap via I.P.)
B
Con
Q
V
VQ
8w
12-30w
Moribund
γ
C
Survival (%)
Days post Immunization
Con (n=14)
Q (n=12)
V (n=16)
VQ (n=17)
**
*
Disease incidence (%)
MM
other lymphoid diseases
other diseases
Q (7)
V (13)
VQ (13)
D
BM
SP
LN
Con
Q
V
VQ1
VQ2
CD138
B220
E
BM
SP
Liver
LN
Kidney
Con
Q
V
VQ
40 μM
F
Con (n=7)
Q (n=7)
V (n=9)
VQ (n=7)
WBC count (10⁶/ml)
ns
RBC count (10⁹/ml)
Hb (g/dl)
Platelet count (10⁶/ml)
***
**
*
G
VQ1
VQ2
1 kb
700 bp
500 bp
400 bp
300 bp
200 bp
75 bp

**Figure 2-2. Molecular characterization of VQ myeloma cells.** (A) Genotyping of NrasQ61R/+ and Vκ*MYC alleles to assess recombination efficiencies in VQ CD138+ cells. (B) hMYC expression in primary CD138+ plasma cells was detected using confocal immunofluorescence. The areas within the red rectangles were zoomed in. (C) Quantification of Ki67+ cells in primary CD138+ cells from moribund VQ MM mice and age-matched control IgG1-Cre, V, and Q mice. (D and E) Quantification of phosphorylated ERK (pERK) (D) and pAKT levels (E) in primary CD138+ cells from moribund VQ MM mice and age-matched control IgG1-Cre, V, and Q mice. *, p<0.05; **, p<0.01; ***, p<0.001.

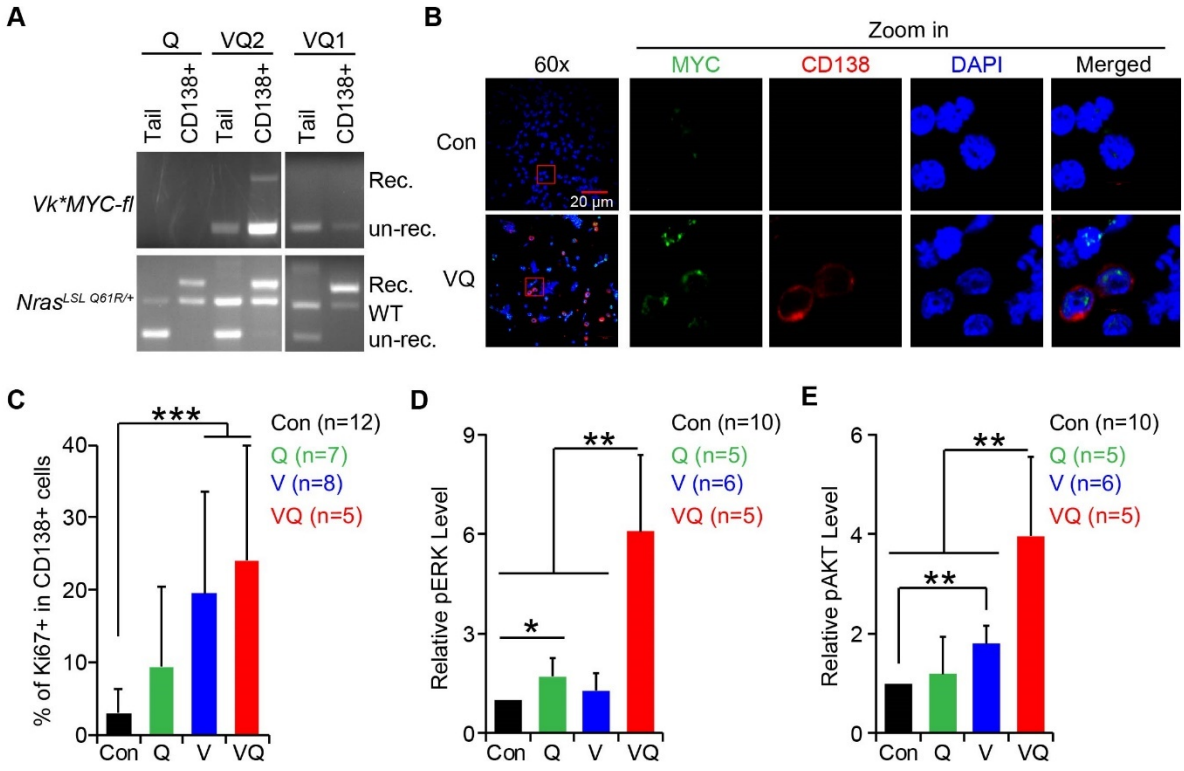

**Figure 2-3. VQ myeloma is readily transplantable to syngeneic secondary recipients.** (A) Schematic illustration of VQ myeloma transplantation strategy. (B) 8 X 106 of VQ1 bone marrow cells (VQ-D1-BM), 20 X 106 of VQ1 splenocytes (VQ-D1-SP), 5 X 106 of VQ2 bone marrow cells (VQ-D2-BM), or 20 X 106 of VQ2 lymph node cells (VQ-D2-LN) were transplanted into individual recipients. Serum protein electrophoresis was performed on recipient mice bled at the moribund stage. The brackets show the γ-globulin component of the serum. The donor cells were isolated from bone marrow (BM), spleen (SP), or lymph node (LN). (C) Kaplan-Meier survival curves of VQ-D1 and VQ-D2 recipient mice, which were transplanted with VQ1 and VQ2 myeloma cells respectively. Log-rank test was performed. **, $p<0.01$. (D) Representative X-ray images and H&E-stained sections of hind limb bones from moribund VQ-D1 and VQ-D2 recipient mice and age-matched control mice. The red arrows indicate the osteolytic lesions. (E) Representative photo of VQ-D1/D2 recipients with hind limb paralysis. (F) Flow cytometric analysis of B220 and CD138 expression on BM, SP, and LN cells from VQ-D1 and VQ-D2 recipient mice. Representative density plots are shown. (G) Representative images of H&E stained BM, SP, liver, LN, and kidney sections.

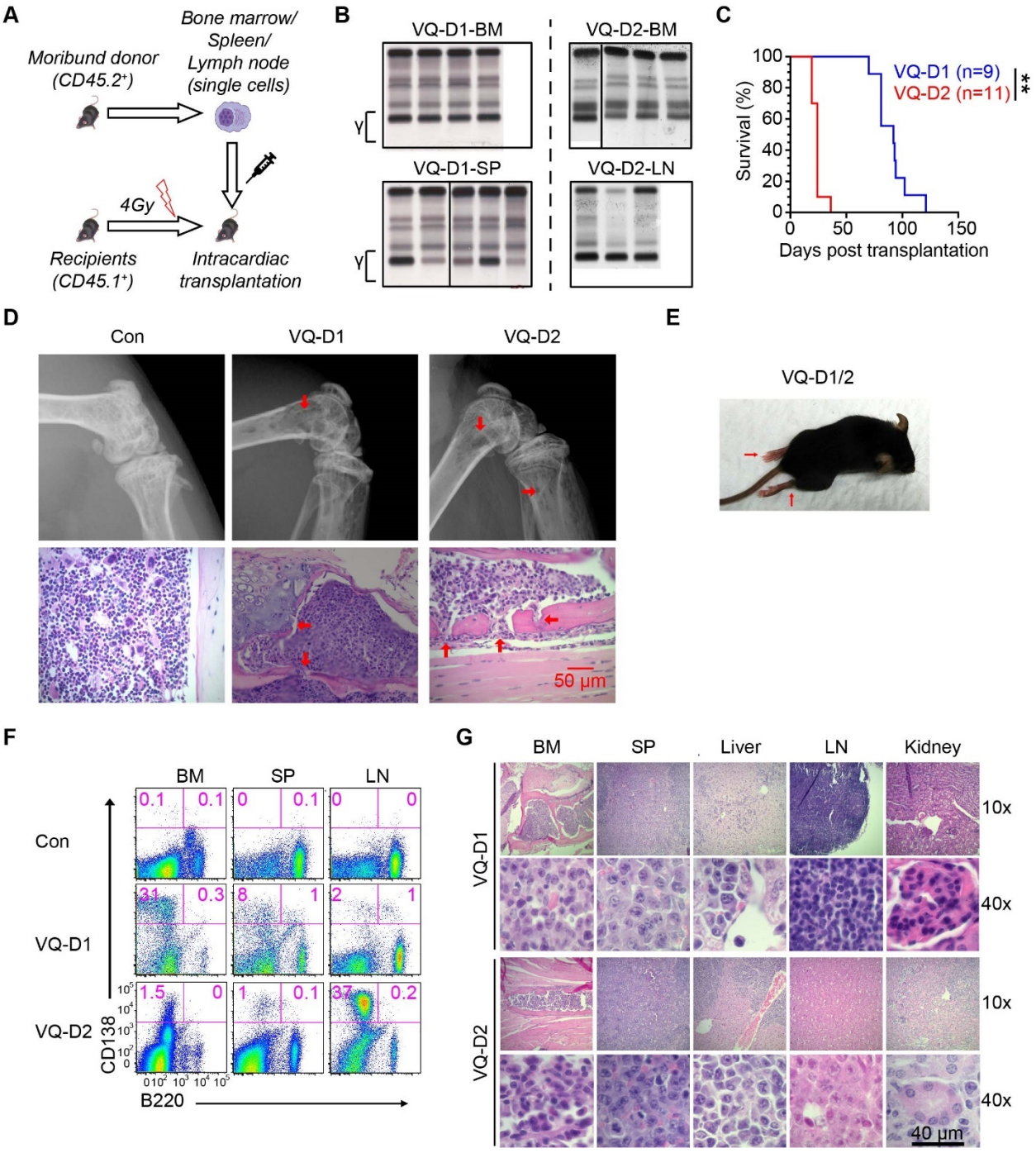
A
Moribund donor (CD45.2+)
Bone marrow/ Spleen/ Lymph node (single cells)
4Gy
Recipients (CD45.1+)
Intracardiac transplantation
B
VQ-D1-BM
VQ-D2-BM
VQ-D1-SP
VQ-D2-LN
γ
C
Survival (%)
Days post transplantation
VQ-D1 (n=9)
VQ-D2 (n=11)
**
D
Con
VQ-D1
VQ-D2
50 μm
E
VQ-D1/2
F
BM
SP
LN
Con
VQ-D1
VQ-D2
CD138
B220
G
BM
SP
Liver
LN
Kidney
VQ-D1
VQ-D2
10x
40x
40 μm

**Figure 2-4. PD-L1/PD1 and CD155/TIGIT immune checkpoint pathways are preserved in VQ myeloma model.** 1 X $10^6$ bone marrow cells from control (IgG1-Cre), VQ-D1 and VQ-D2 myeloma mice (>6 passages) were transplanted into sub-lethally irradiated recipients as described in Fig. 3. (A, B) Flow cytometric analysis of CD138, PD-L1, PD-L2, CD155 (A), MHC-I, and MHC-II (B) on bone marrow (BM) of VQ-D1 recipients and lymph node (LN) cells of VQ-D2 recipients. Representative density plots are shown. (C, D) Quantification of PD1+ and TIGIT+ T cells (CD8+ and CD4+) in bone marrow (BM), spleen (SP), and lymph node (LN) from age-matched control, VQ-D1 (C), and VQ-D2 (D) recipients. (E, F) Quantification of CD8+ and CD4+ T cells in BM, SP, and LN of control, VQ-D1 (E), and VQ-D2 (F) recipients. *, $p<0.05$; **, $p<0.01$; ***, $p<0.001$.

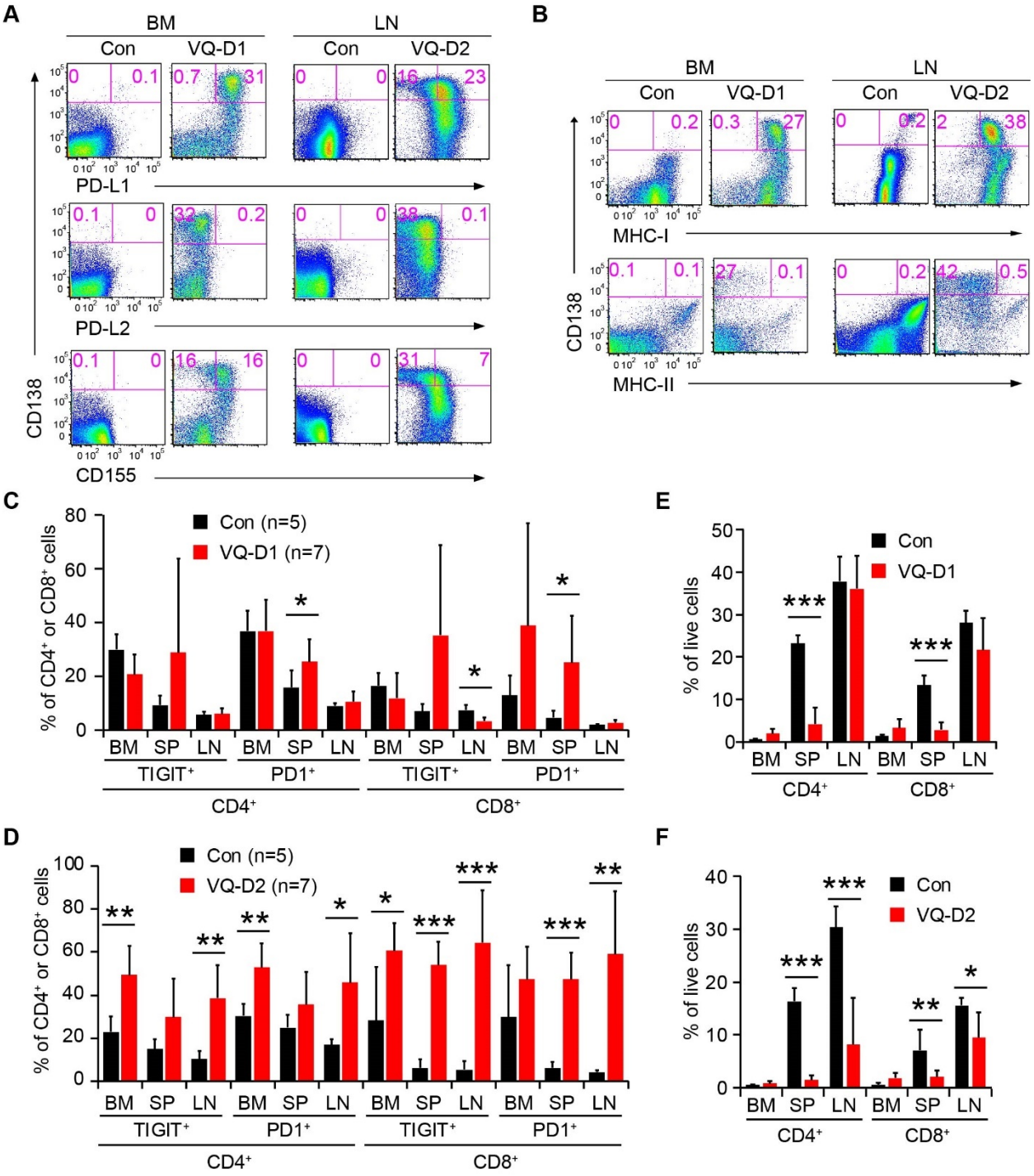
A
BM
LN
Con
VQ-D1
Con
VQ-D2
PD-L1
PD-L2
CD155
CD138
B
MHC-I
MHC-II
C
Con (n=5)
VQ-D1 (n=7)
% of CD4+ or CD8+ cells
BM SP LN BM SP LN BM SP LN BM SP LN
TIGIT+ PD1+ TIGIT+ PD1+
CD4+ CD8+
D
Con (n=5)
VQ-D2 (n=7)
% of CD4+ or CD8+ cells
E
Con
VQ-D1
% of live cells
CD4+ CD8+
F
Con
VQ-D2
% of live cells

**Figure 2-5. VQ myeloma cells display unique transcriptional signatures from normal plasma cells.** CD138+ B220- cells were sorted from age-matched control bone marrow (Con-BM) and VQ-D2 BM and lymph node (LN). scRNA-Seq analysis was performed as described in Methods. (A) tSNE plot depicting 749 single plasma cells derived from control and VQ-D2 mice. Each cluster is represented by a specific color and number. The top 20 genes expressed in each cluster are presented in the heatmap. (B) Samples are color-coded and projected on the tSNE plot (blue: Con-BM; red: VQ-BM; green: VQ-LN). (C) Cell cycle phases are color-coded and projected on the tSNE plot (red: G1; green: G2/M; blue: S). (D) GSEA was performed between VQ-BM and Con-BM plasma cells. Adjusted p value and normalized enrichment score (NES) are shown on each plot. (E) Signature module scores were calculated for each cell based on the expression levels of genes associated with high-risk MM and the average expression profile of each cell. P value was determined using Welch's t-test between VQ (BM + LN) and Con-BM.

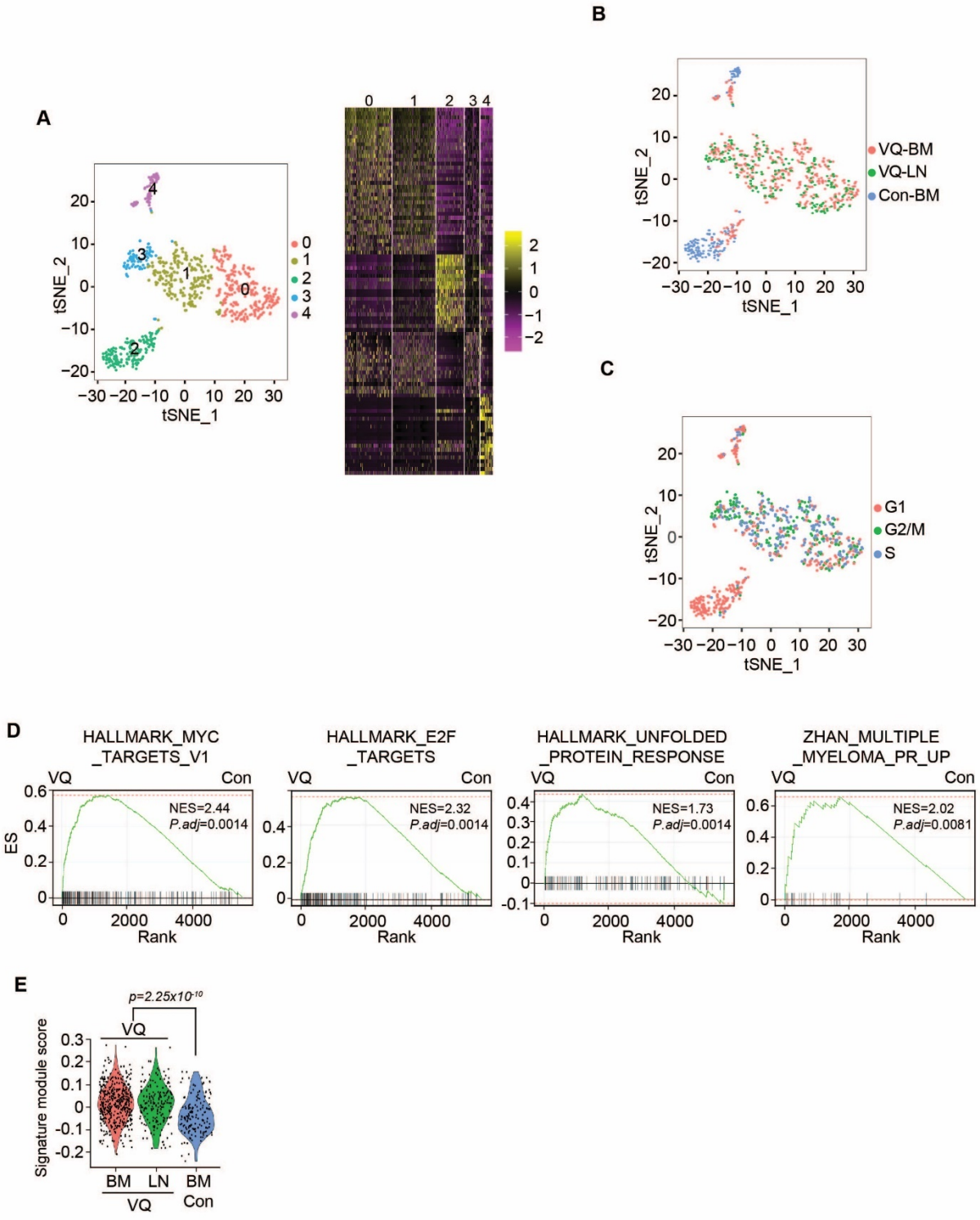
A
B
C
D
E
tSNE_1
tSNE_2
VQ-BM
VQ-LN
Con-BM
G1
G2/M
S
HALLMARK_MYC _TARGETS_V1
HALLMARK_E2F _TARGETS
HALLMARK_UNFOLDED _PROTEIN_RESPONSE
ZHAN_MULTIPLE _MYELOMA_PR_UP
VQ
Con
NES=2.44
P.adj=0.0014
NES=2.32
P.adj=0.0014
NES=1.73
P.adj=0.0014
NES=2.02
P.adj=0.0081
ES
Rank
p=2.25x10-10
Signature module score
BM
LN
BM
VQ
Con

**Figure 2-6. Transcriptomic profiling of normal plasma cells and MM models using bulk RNA-Seq.** Bulk RNA-Seq analysis was performed using 50,000 sorted CD138+ B220- CD45.2+ bone marrow cells of WT(n=3), V (n=3), recipients of tVk12653 (n=2), VQ-D1 (n=2), VQ-D4 (n=1), and VQ-D5 (n=2). (A) Normalized expression levels of Myc in all samples. FPKM, Fragments Per Kilobase of gene per Million mapped reads. *, p<0.05; **, p<0.01; ***, p<0.001. (B) Scatterplots of average log10 FPKM values of all mapped genes of V, tVk12653, or VQ samples vs WT samples. Red and blue dots represent differentially up- and down-regulated genes respectively for each comparison (log¬2FC >1 or <-1, P.adj <0.05). r2 value calculated from Pearson's correlation coefficient. (C) Volcano plots illustrating the differentially expressed genes in tVk12653 or VQ MM cells vs WT plasma cells. GSEA was performed between tVk12653 or VQ and WT plasma cells against Hallmark (D) or UAMS-70 (E) gene sets. (F) Volcano plots illustrating the differentially expressed genes in VQ vs tVk12653 MM cells. GSEA analysis was performed between VQ and tVk12653 MM cells against Hallmark (G) or C2 curated (H) gene sets. Adjusted P value (P. adj) and normalized enrichment score (NES) are shown on each GSEA plot.

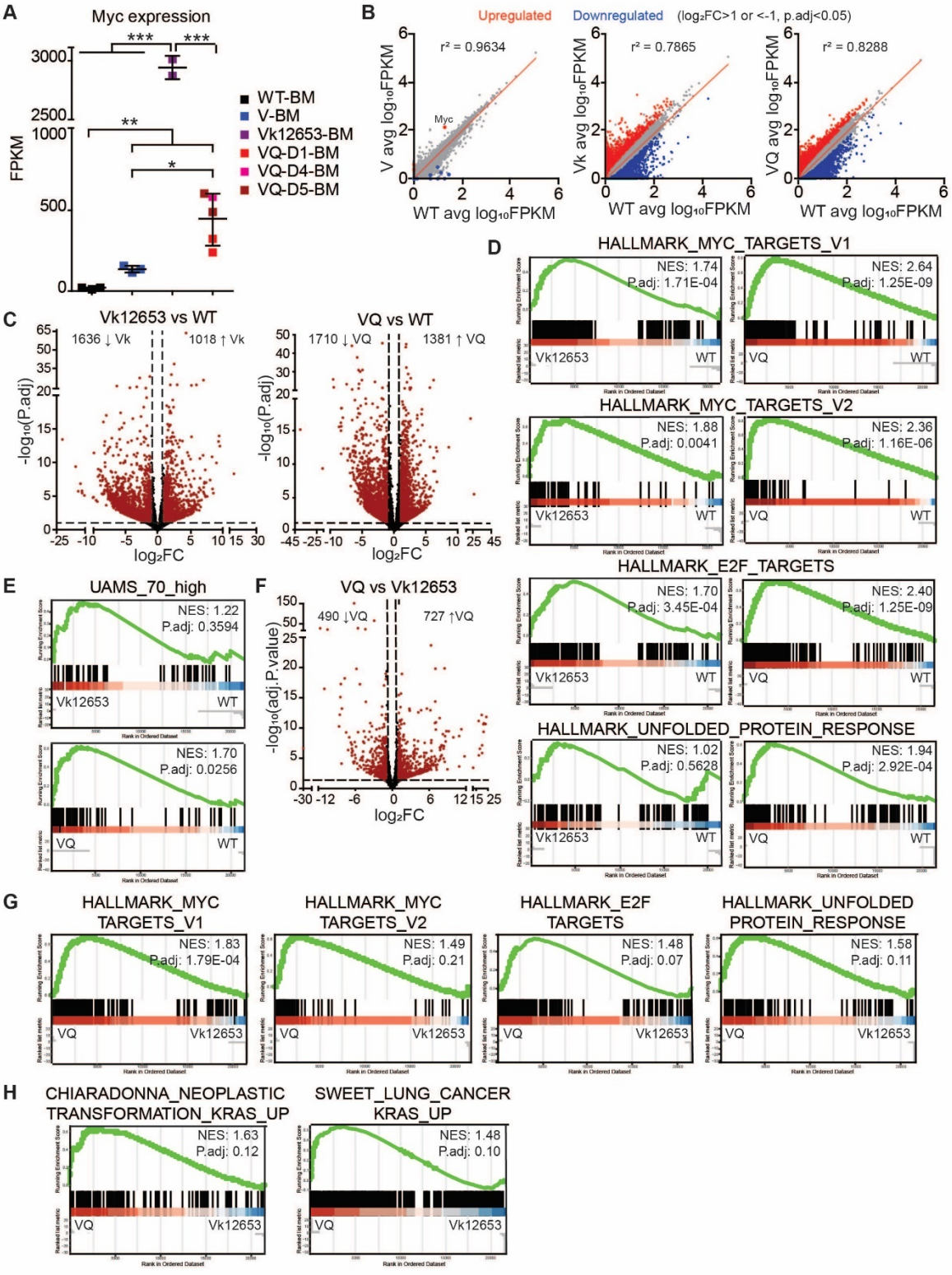
A
Myc expression
FPKM
WT-BM
V-BM
Vk12653-BM
VQ-D1-BM
VQ-D4-BM
VQ-D5-BM
B
Upregulated
Downregulated
(log2FC>1 or <-1, p.adj<0.05)
r² = 0.9634
r² = 0.7865
r² = 0.8288
V avg log10FPKM
Vk avg log10FPKM
VQ avg log10FPKM
WT avg log10FPKM
Myc
C
Vk12653 vs WT
1636 ↓ Vk
1018 ↑ Vk
VQ vs WT
1710 ↓ VQ
1381 ↑ VQ
-log10(P.adj)
log2FC
D
HALLMARK_MYC_TARGETS_V1
NES: 1.74
P.adj: 1.71E-04
NES: 2.64
P.adj: 1.25E-09
HALLMARK_MYC_TARGETS_V2
NES: 1.88
P.adj: 0.0041
NES: 2.36
P.adj: 1.16E-06
HALLMARK_E2F_TARGETS
NES: 1.70
P.adj: 3.45E-04
NES: 2.40
P.adj: 1.25E-09
HALLMARK_UNFOLDED_PROTEIN_RESPONSE
NES: 1.02
P.adj: 0.5628
NES: 1.94
P.adj: 2.92E-04
Vk12653
WT
VQ
E
UAMS_70_high
NES: 1.22
P.adj: 0.3594
NES: 1.70
P.adj: 0.0256
F
VQ vs Vk12653
490 ↓VQ
727 ↑VQ
-log10(adj.P.value)
log2FC
G
HALLMARK_MYC TARGETS_V1
NES: 1.83
P.adj: 1.79E-04
HALLMARK_MYC TARGETS_V2
NES: 1.49
P.adj: 0.21
HALLMARK_E2F TARGETS
NES: 1.48
P.adj: 0.07
HALLMARK_UNFOLDED PROTEIN_RESPONSE
NES: 1.58
P.adj: 0.11
H
CHIARADONNA_NEOPLASTIC TRANSFORMATION_KRAS_UP
NES: 1.63
P.adj: 0.12
SWEET_LUNG_CANCER KRAS_UP
NES: 1.48
P.adj: 0.10

**Figure 2-7. Combined MEK inhibitor and pan-BET inhibitor ameliorate MM phenotypes and prolong the survival of VQ myeloma mice.** (A-I) Two MM cell lines were established from VQ-D2 recipient mice. (A) Schematic illustration of the procedure to establish 2 VQ MM cell lines. (B) Representative images of H&E stained 4935 and 4938 cells. (C) Flow cytometric assay of B220 and CD138 expression on the two cell lines. (D) Genotyping of NrasQ61R and Vκ*MYC alleles in the two cell lines. (E) hMYC expression in the cell lines was detected using confocal immunofluorescence. (F) HA-tagged hMYC expression in the cell lines was validated using Western blot analysis. Left: rabbit anti-Myc antibody; Right: rat anti-HA antibody conjugated with HRP. (G, H) Flow cytometric analysis of CD138, PD-L1, CD155 (G), MHC-I, and MHC-II (H) expression on the cell lines. (I) Quantification of retroviral and lentiviral infection rate in the cell lines based on flow cytometric analysis of GFP. (J, K) VQ MM cell lines were treated with increasing concentrations of trametinib for 48 hours. (J) Cell growth was measured using Cell TiterGlo assay. (K) Quantification of surface expression of PDL1 and CD155 in the presence of 10 nM of trametinib. (L, M) VQ MM cell lines were treated with increasing concentrations of GSK525762 for 48 hours. (L) Cell growth was measured using Cell TiterGlo assay. (M) Quantification of surface expression of PDL1 and CD155 in the presence of 3 μM of GSK525762. (N, O) VQ recipients were treated with vehicle or drug(s) as described in Materials and Methods. Veh, vehicle; T, trametinib; G, GSK525762; TG, trametinib and GSK525762. (N) Serum protein electrophoresis was performed to quantify the γ-globulin/Albumin ratios in VQ recipient mice before treatment (Pre) and at day 21 of treatment or at moribund before day 21 (Post). Note: some of the recipients were found dead and unable to be analyzed. Paired two-tailed Student's t-tests were performed. (O) Kaplan-Meier survival curves were plotted against days after treatment. Log-rank test was performed. *, $p<0.05$; **, $p<0.01$.

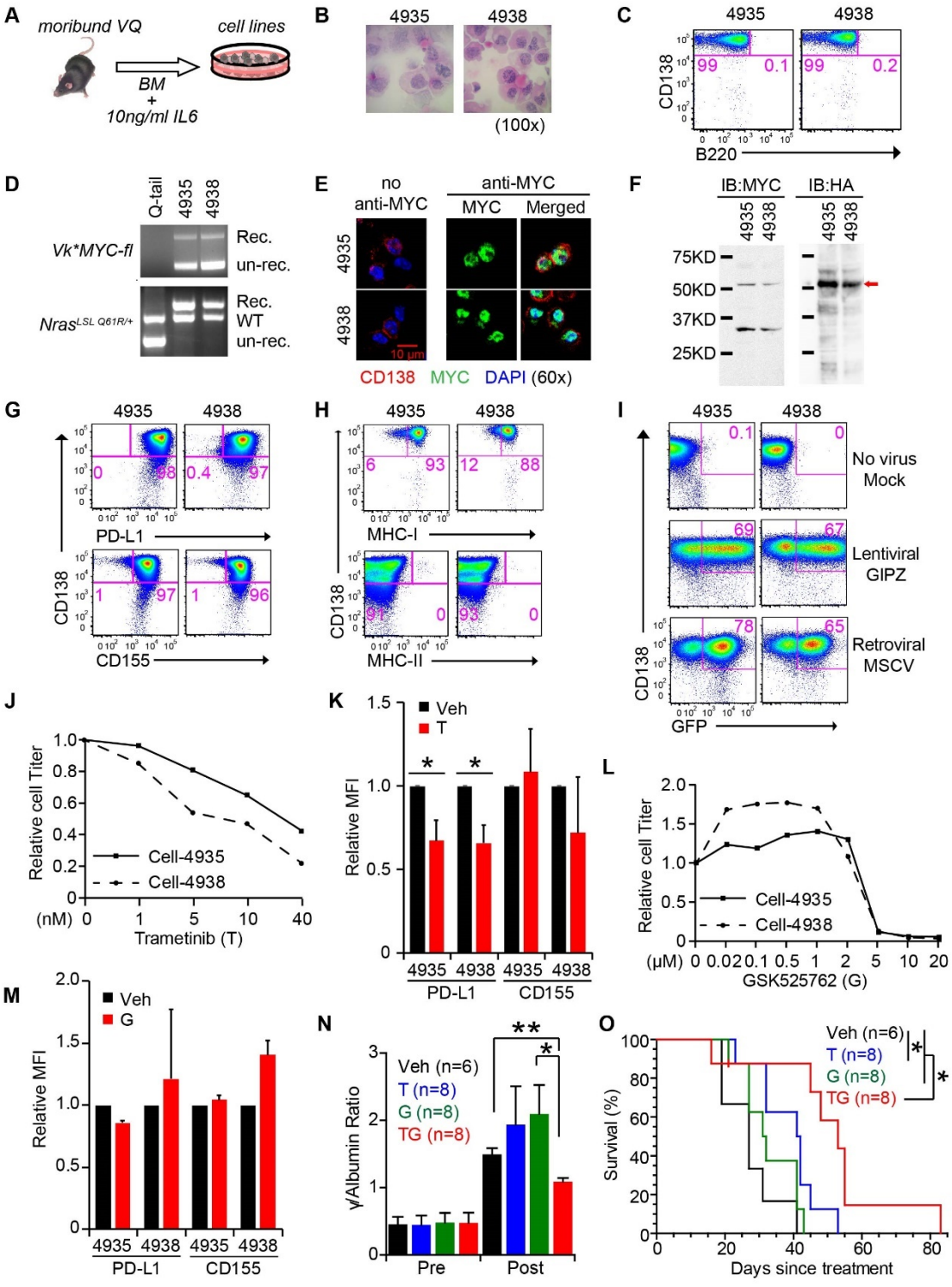
A
moribund VQ
cell lines
BM
+
10ng/ml IL6
B
4935
4938
(100x)
C
4935
4938
CD138
B220
99
0.1
99
0.2
D
Q-tail
4935
4938
Vk*MYC-fl
Rec.
un-rec.
Nras LSL Q61R/+
Rec.
WT
un-rec.
E
no anti-MYC
anti-MYC
MYC
Merged
4935
4938
10 μm
CD138 MYC DAPI (60x)
F
IB:MYC
IB:HA
4935
4938
4935
4938
75KD
50KD
37KD
25KD
G
4935
4938
PD-L1
CD138
CD155
0
88
0.4
97
1
97
1
96
H
4935
4938
MHC-I
CD138
MHC-II
6
93
12
88
91
0
93
0
I
4935
4938
No virus
Mock
Lentiviral
GIPZ
Retroviral
MSCV
CD138
GFP
0.1
0
69
67
78
65
J
Relative cell Titer
Cell-4935
Cell-4938
(nM) 0 1 5 10 40
Trametinib (T)
K
Veh
T
Relative MFI
4935 4938 4935 4938
PD-L1
CD155
L
Relative cell Titer
Cell-4935
Cell-4938
(μM) 0 0.02 0.1 0.5 1 2 5 10 20
GSK525762 (G)
M
Veh
G
Relative MFI
4935 4938 4935 4938
PD-L1
CD155
N
γ/Albumin Ratio
Veh (n=6)
T (n=8)
G (n=8)
TG (n=8)
Pre
Post
O
Veh (n=6)
T (n=8)
G (n=8)
TG (n=8)
Survival (%)
Days since treatment

**Figure 2-S1. Schematic illustration of the *Vκ*MYC* allele.** Asterisks indicate the introduced stop codons. 3' Kappa enhancers (3' kE) are floxed. The relative positions of genotyping PCR primers are shown.

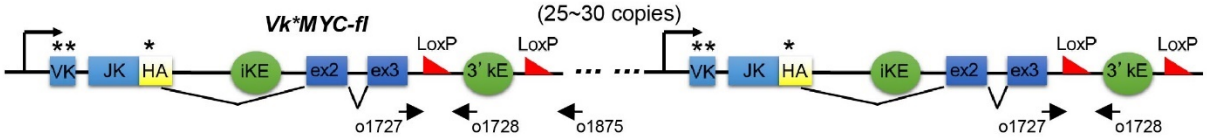


**Figure 2-S2. Histological evaluation of VQ mice.** (A) Representative 10X images of H&E stained sections of VQ bone marrow (BM), spleen (SP), liver, lymph node (LN), and kidney. The normal architecture of BM, SP, liver, and LN were completely destroyed by VQ MM cells, while VQ kidney preserved normal structure in general. (B) Four out of five VQ myeloma mice developed Rouleaux (red arrows indicate stacked red blood cells).

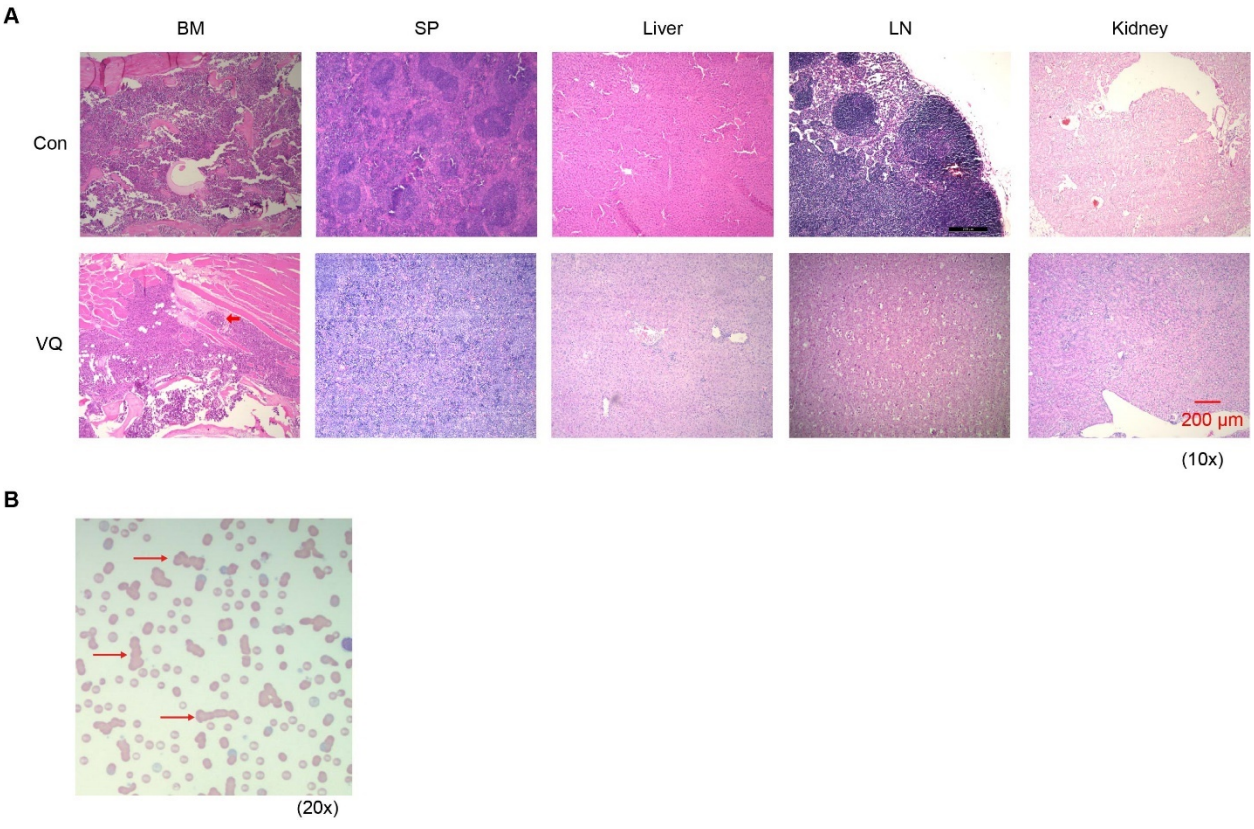

**Figure 2-S3. Clonality analysis of B220$^{+}$ cells sorted from Q and V mice with other lymphoid diseases.**

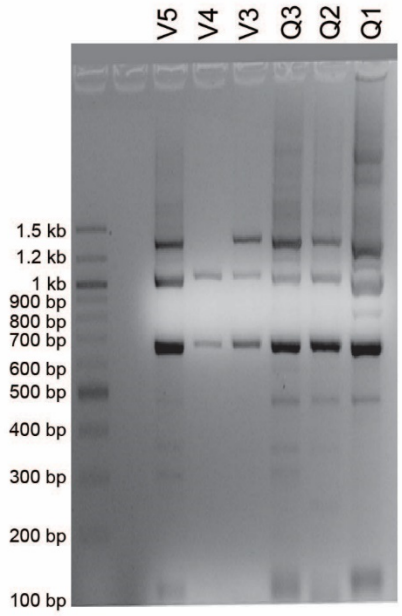


**Figure 2-S4. Characterization of V recipient mice.** 10 X $10^6$ bone marrow cells from three moribund V mice were transplanted into sub-lethally irradiated recipients as described in Fig. 3A. (A) SPEP analysis was performed on the moribund V donor mice. (B) Flow cytometric analysis of B220 and CD138 expression on bone marrow (BM), spleen (SP), and lymph node (LN) cells from moribund donor mice. (C) Complete blood count results of moribund donor mice. WBC, white blood cell; RBC, red blood cell; Hb, hemoglobin. (D) Kaplan-Meier survival curves of the recipient mice from different donors. (E) SPEP analysis was performed on the recipient mice 4 weeks post transplantation.

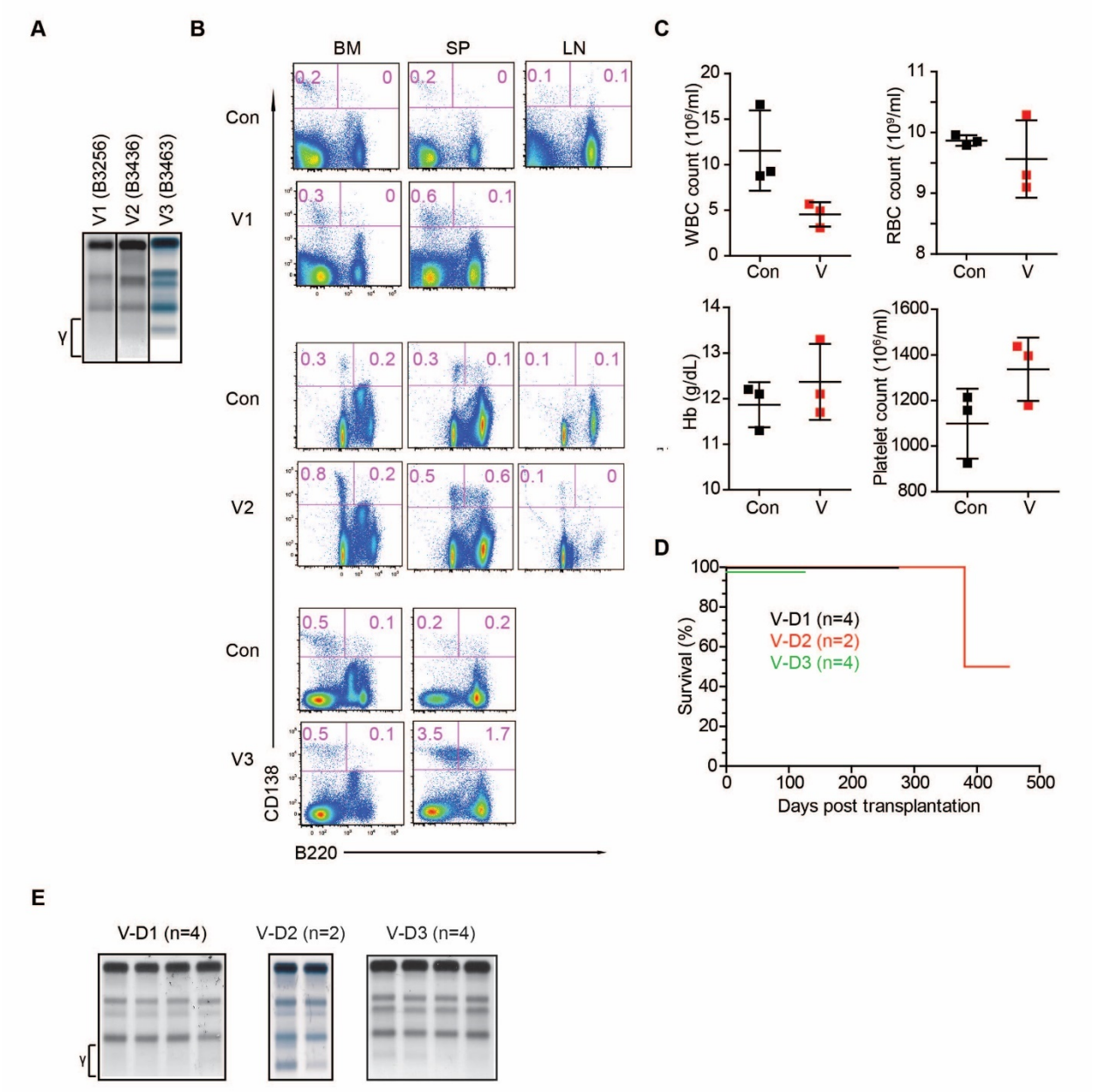


**Figure 2-S5. Characterization of Q recipient mice.** 10 X $10^6$ bone marrow cells or 20 x $10^6$ lymph node cells from 2 moribund Q mice were transplanted into sub-lethally irradiated recipients as described in Fig. 3A. (A) SPEP analysis was performed on the moribund Q donor mice. (B) Flow cytometric analysis of B220 and CD138 expression on bone marrow (BM), spleen (SP), and lymph node (LN) cells from moribund donor mice. (C) Complete blood count results of moribund donor mice. WBC, white blood cell; RBC, red blood cell; Hb, hemoglobin. (D) SPEP analysis was

performed on the Q recipients at the indicated times posttransplant. (E) Representative X-ray images of hind limb bones from moribund recipient mice and age-matched control mice. (F) Kaplan-Meier survival curves of the recipient mice from different donors. (G) Flow cytometric analysis of B220 and CD138 expression on BM, SP, and LN cells from moribund recipient mice. Representative density plots are shown. (H) Representative images of H&E stained BM, SP, liver, LN, and kidney tissue sections from moribund recipient mice.

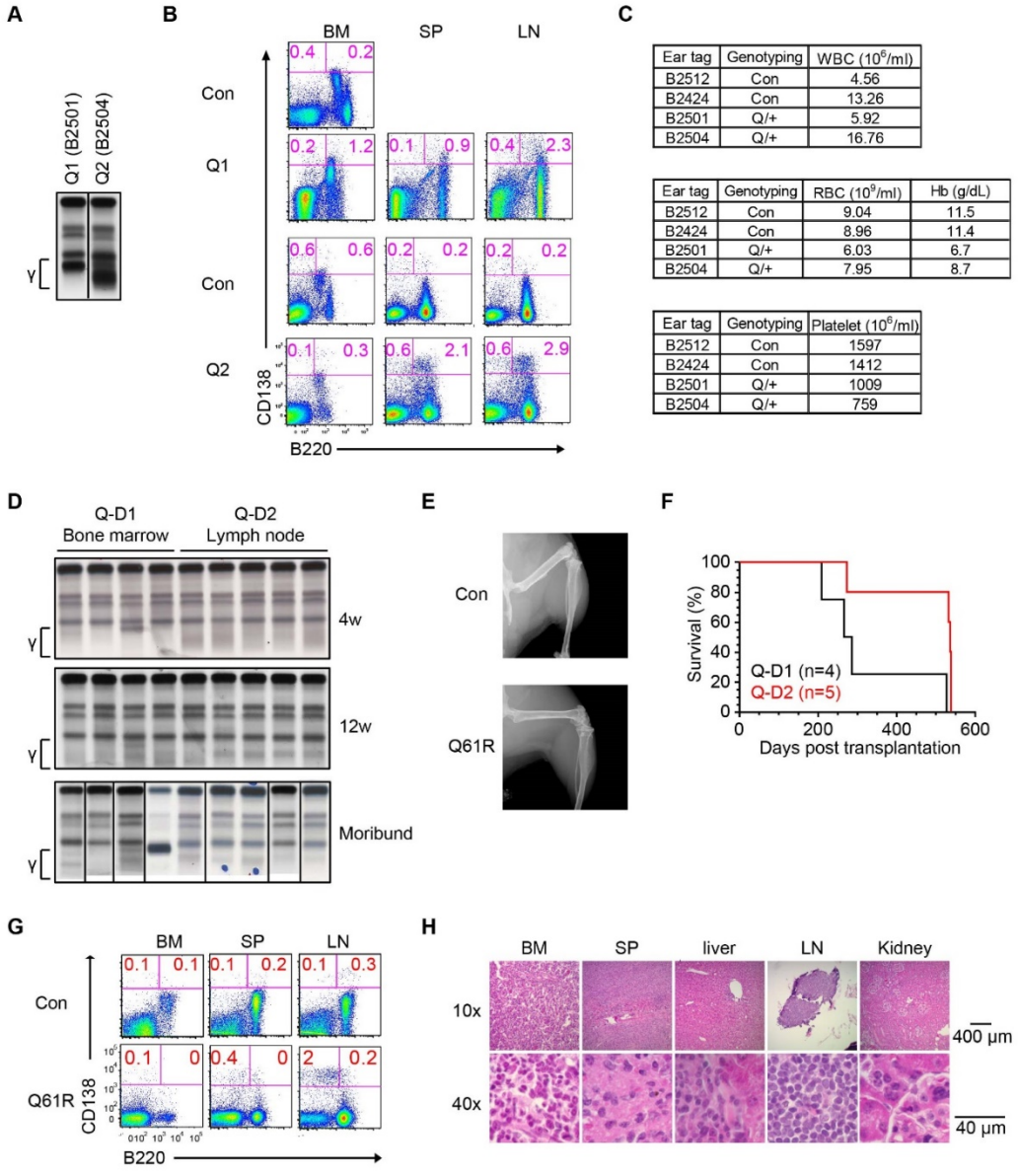

**Figure 2-S6. Characterization of additional VQ mice.** (A) Flow cytometric analysis of B220 and CD138 expression on cells of bone marrow (BM), spleen (SP) and lymph node (LN) from additional moribund VQ mice and their age-matched control mice. (B) ~5 X $10^6$ of VQ4 or VQ5 bone marrow cells were transplanted into individual recipients. Recipients were monitored for MM development and sacrificed for terminal evaluation upon moribund. Kaplan-Meier survival curves of VQ-D4 and VQ-D5 recipient mice were established. (C) Clonality analysis of $CD138^+$ $B220^-$ cells sorted from VQ recipient mice using $DJ_H$ recombination PCR assay.

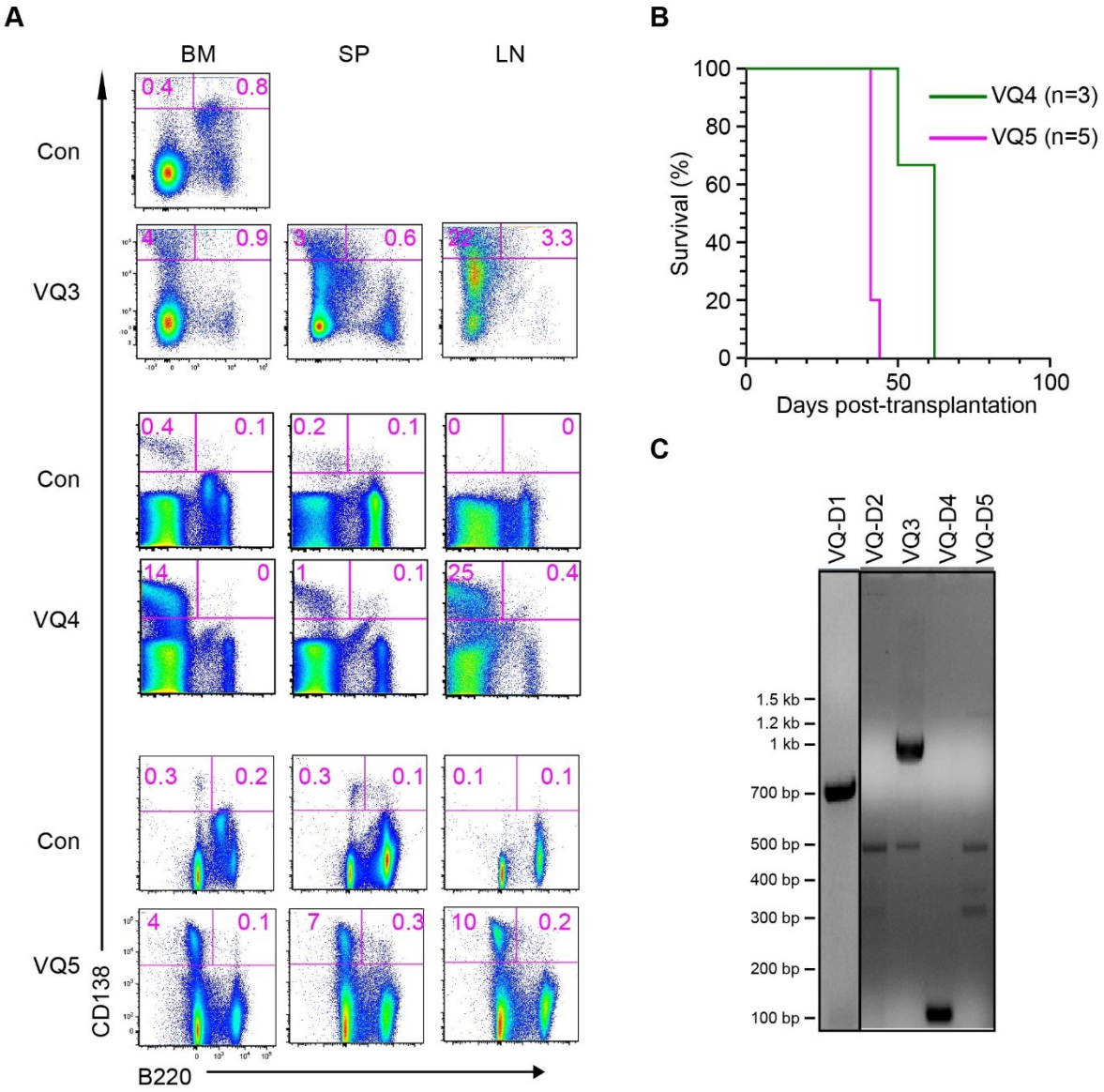

**Figure 2-S7. Molecular characterization of CD138⁺ cells from moribund VQ recipient mice.** (A) Flow cytometric assay of CD138 and CD19 expression on bone marrow (BM) or lymph node (LN) cells from moribund VQ-D1 and VQ-D2 recipients. (B) Quantification of Ki67⁺ cells in VQ-D1 and VQ-D2 CD138⁺ cells. (C) Quantification of phosphorylated ERK (pERK) and p-AKT levels in VQ-D1 and VQ-D2 CD138⁺ cells. Results of relative mean fluorescence intensity (MFI) are presented as average + SD. *, $p<0.05$; ***, $p<0.001$.

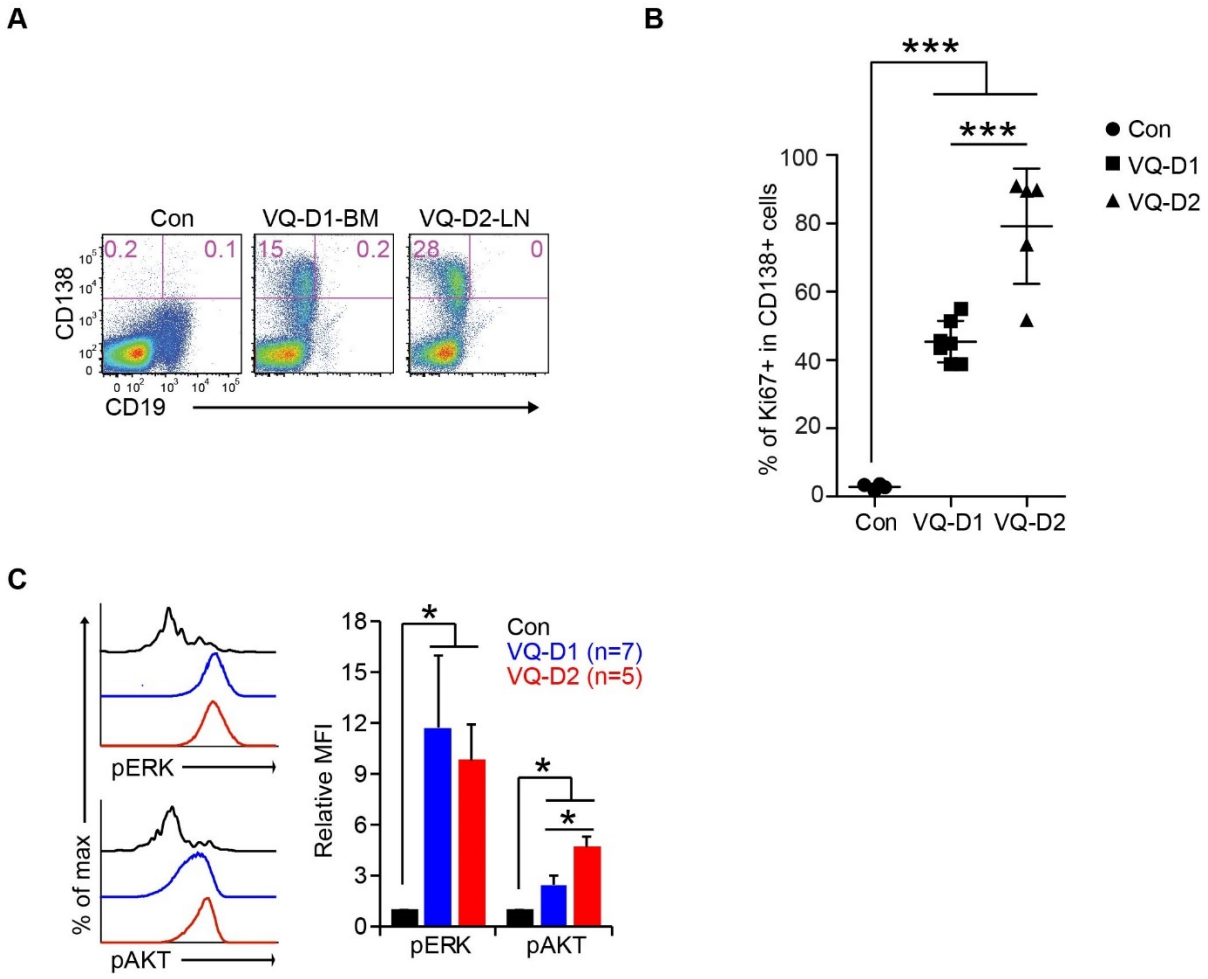

**Figure 2-S8. MM phenotypes are passaged *in vivo*.** (A) Freshly isolated VQ-D1 and VQ-D2 donor cells were passaged *in vivo* over six generations, each of which showed key MM phenotypes of their corresponding donors. Note: The numbers are the number of mice with M-spike out of the total number of mice transplanted (in brackets). * represents the percentage of $CD138^+$ $B220^-$ cells in bone marrow, spleen, and/or lymph node of each assayed mouse. N.A., not available. (B) At least two vials of cryopreserved VQ-D1 and VQ-D2 donor cells were recovered from liquid nitrogen and transplanted into sub-lethally irradiated recipient mice. All recipient mice recapitulated the MM phenotypes of their corresponding donors. (C) 10 X $10^6$ cryopreserved VQ-D1 and VQ-D2 bone marrow cells were transplanted into individual non-irradiated recipient mice as described above. Kaplan-Meier survival curves of the recipient mice were established.

**A**

| In vivo passage | VQ-D1 | | | | VQ-D2 | | | |
|---|---|---|---|---|---|---|---|---|
| | M spike | | CD138+B220- (>10%) | Survival (d) | M spike | | CD138+B220- (>10%) | Survival (d) |
| | number | assay time* | | | number | assay time* | | |
| 1 | 9 (9) | 61 | 100% | 78 ± 5 | 4 (4) | 19 | 100% | 23 ± 8 |
| 2 | 25 (25) | 56 | 100% | 92 ± 4 | 4 (4) | 24 | 100% | 24 ± 0 |
| 3 | 10 (10) | 57 | 100% | 79 ± 1 | 10 (10) | 14-26 | 100% | 23 ± 5 |
| 4 | 8 (8) | 56 | 100% | 100 ± 3 | N.A. (3) | | 100% | 25 ± 4 |
| 5 | N.A. (4) | | 100% | 84 ± 6 | 2 (2) | 25 | 100% | 25 ± 0 |
| 6 | 4 (4) | 54 | 100% | 64 ± 6 | N.A.(3) | | 100% | 32 ± 0 |

assay time*: samples were collected on the indicated days after transplantation.

**B**

| Frozen primary donor cells | VQ-D1 | VQ-D2 | VQ-D4 | VQ-D5 |
|---|---|---|---|---|
| | 2 donors | 3 donors | 1 donor | 1 donor |
| M spike | 9 (9) | 8 (8) | 2 (2) | 1 (3) |
| $CD138^+B220^-$ (>10%)* | 100% | 100% | 100% | 33% |
| # of cells injected | 5-8 $x10^6$ | 1-3 $x10^6$ | 2 $x10^6$ | 2 $x10^6$ |
| Survival (day) | 40-60 | 21-39 | 124-132 | 95- ongoing |

**C**

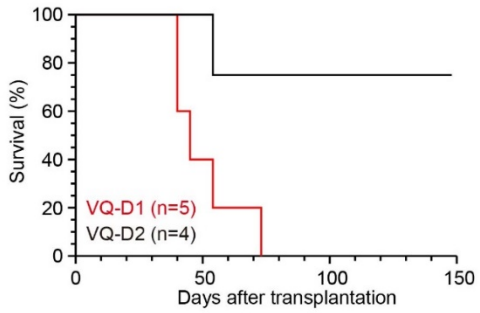

**Figure 2-S9. Myeloma initiating cells are enriched in CD138$^+$ B220$^-$ bone marrow cells.** (A) Bone marrow cells from moribund VQ-D1 recipients were analyzed for donor origin (CD45.2$^+$) in CD138$^+$ B220$^-$, CD138$^-$ B220$^+$, and CD138$^-$ B220$^-$ populations. (B, C) Bone marrow cells from moribund VQ-D1 recipients (B) and lymph node cells from VQ-D2 recipients (C) were flow sorted into CD138$^+$ B220$^-$ and CD138$^-$ B220$^-$ populations. The sorted cells were transplanted into sub-lethally irradiated recipient mice with different cell numbers as indicated. The recipient mice were closely monitored for up to 15 months and diagnosed at the moribund stage.

A

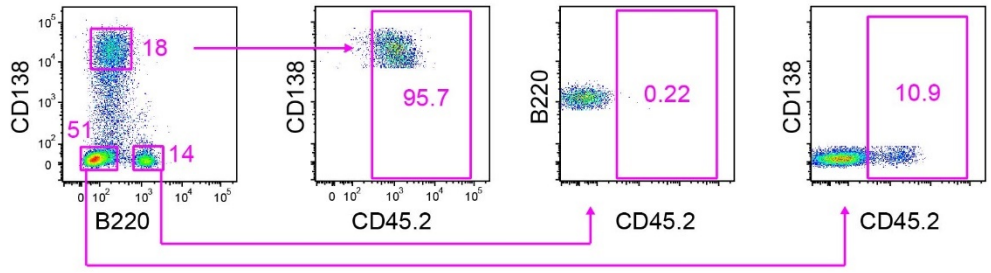


B

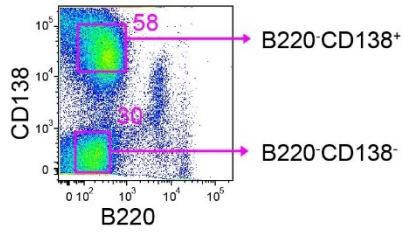


| VQ-D1 Cell type | # of Donor cells/recipient | # of recipients | # of Mice with MM | Survival (day) |
|---|---|---|---|---|
| CD138- B220- | 3, 500, 000 | 1 | 0 | N/A |
| CD138+ B220- | 2, 500 | 4 | 4 | 100 ± 3 |
| | 500 | 5 | 5 | 134 ± 9 |
| | 100 | 5 | 1 | 132 |

C

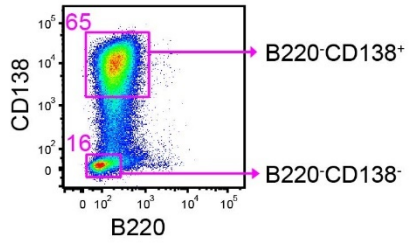


| VQ-D2 Cell type | # of Donor cells/recipient | # of recipients | # of Mice with MM | Survival (day) |
|---|---|---|---|---|
| CD138- B220- | 100, 000 | 4 | 0 | N/A |
| | 1, 000, 000 | 4 | 0 | N/A |
| CD138+ B220- | 17, 000 | 2 | 2 | 25 |
| | 10, 000 | 1 | 1 | 24 |
| | 2, 500 | 5 | 5 | 55 ± 23 |
| | 500 | 5 | 5 | 67 ± 19 |
| | 100 | 5 | 2 | 62 &137 |

**Figure 2-S10. Myeloma cells in bone marrow display distinct gene transcriptional profiles from those in lymph node.** CD138$^{+}$ B220$^{-}$ cells were sorted from age-matched control bone marrow (Con-BM) and VQ-D2 BM and lymph node (LN). scRNA-Seq analysis was performed as described in Methods. (A) Summary of the number of single cells analyzed from each sample. (B) Distribution of the number of genes and unique molecular identifiers (UMIs) in each cells from each sample. (C) GSEA analysis of VQ-BM vs VQ-LN. Adjusted p value and normalized enrichment score (NES) are shown on each plot.

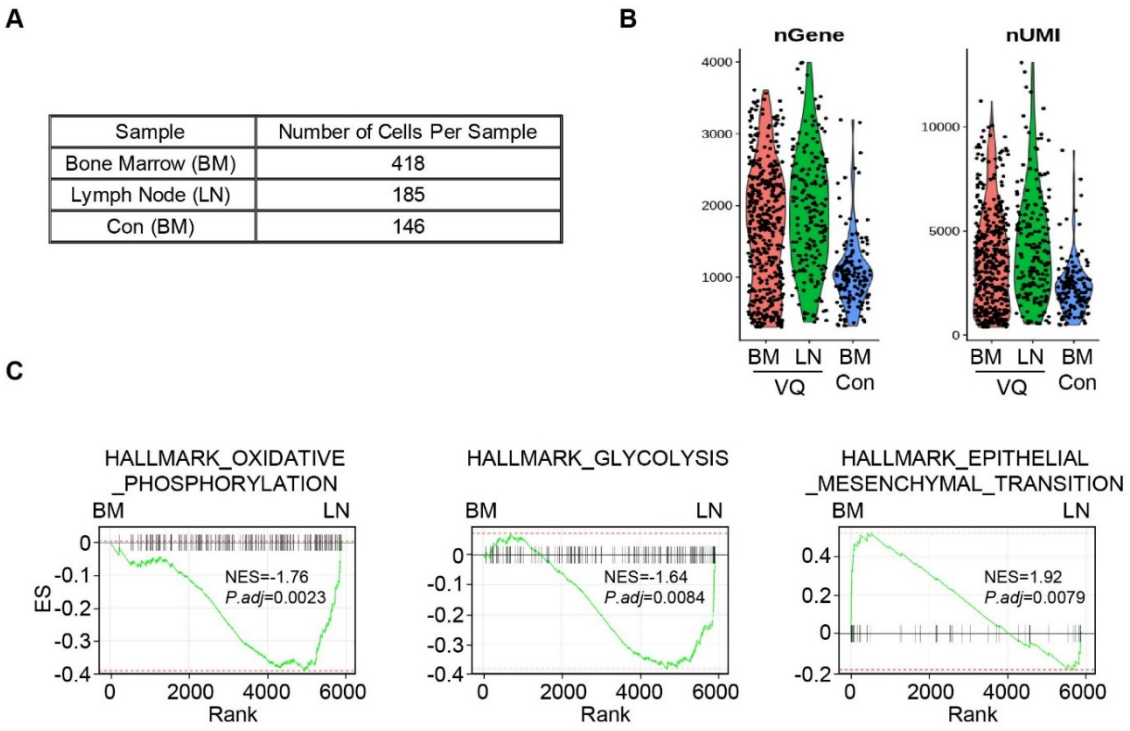


**Figure 2-S11. EMC-92 gene signature is not enriched in tVk12653 and VQ MM cells.**

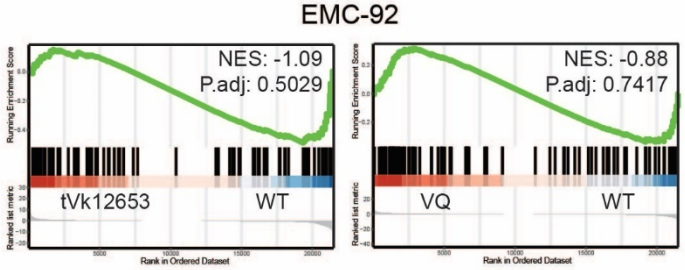

**Figure 2-S12. Combined MEK inhibitor and proteasome inhibitor ameliorate MM phenotypes and prolong the survival of VQ myeloma mice.** (A, B) VQ MM cell lines were treated with increasing concentrations of AZD6244 (A) or bortezomib (B) for 48 hours. Cell growth was measured using Cell TiterGlo assay. (C) Schematic illustration of pre-clinical study design. VQ recipients were treated with vehicle or drug(s) for 21 days as described in Materials and Methods. (D) Serum protein electrophoresis was performed to quantify the γ-globulin/Albumin ratio in VQ recipient mice before treatment, at the moribund stage, or at day 28. Note: some of the recipients were found dead and unable to be analyzed. AZD, AZD6244; BTZ, bortezomib; Combo, AZD+BTZ. (E) Complete blood count (CBC) was performed one week after treatment was over. (F) Kaplan-Meier survival curves of different treatment groups of animals were plotted against days after treatment. Log-rank test was performed. *, $p<0.05$; **, $p<0.01$; ***, $p<0.001$.

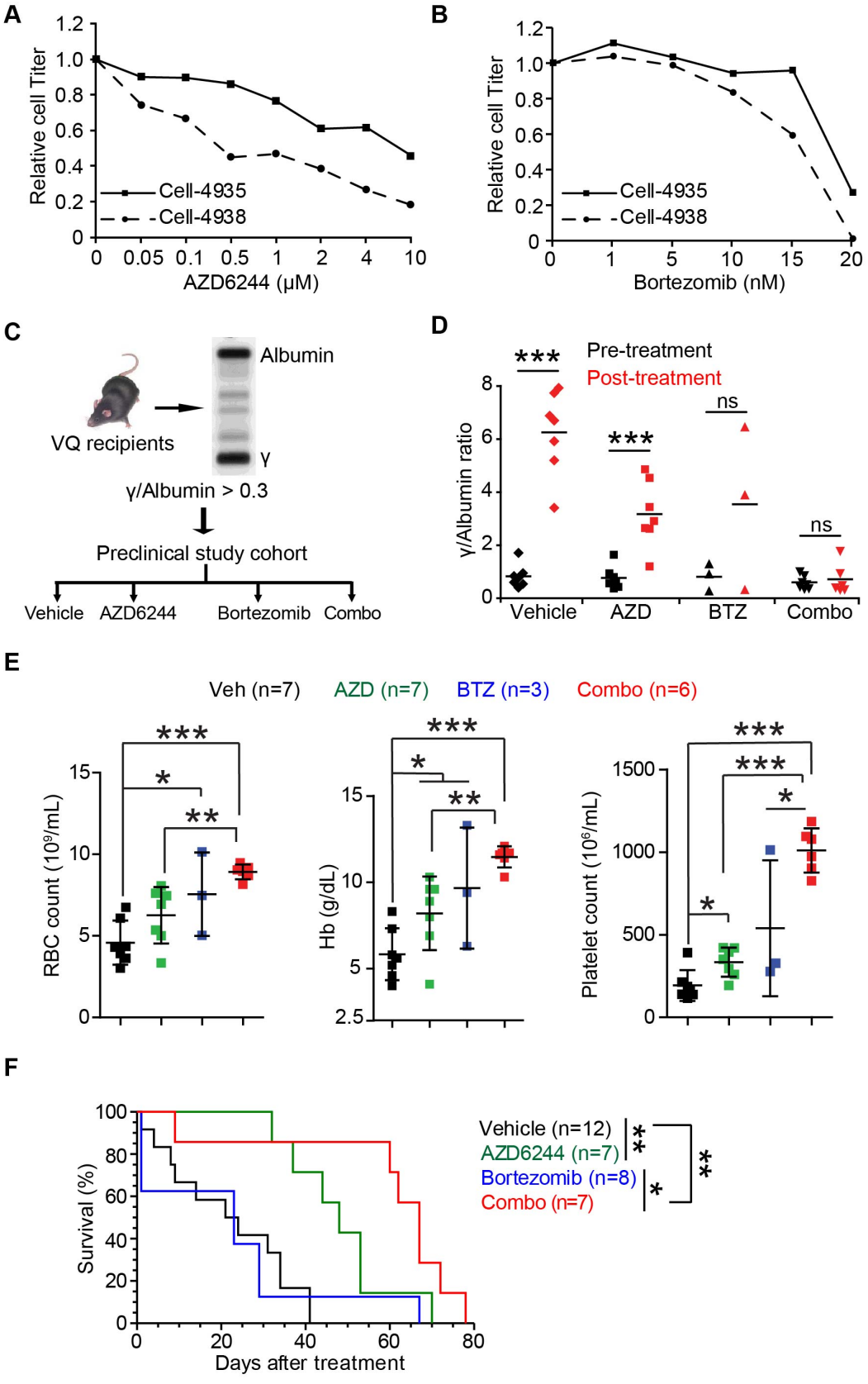
A
Relative cell Titer
1.2
1.0
0.8
0.6
0.4
0.2
0
Cell-4935
Cell-4938
0 0.05 0.1 0.5 1 2 4 10
AZD6244 (μM)
B
Relative cell Titer
1.2
1.0
0.8
0.6
0.4
0.2
0
Cell-4935
Cell-4938
0 1 5 10 15 20
Bortezomib (nM)
C
Albumin
γ
VQ recipients
γ/Albumin > 0.3
Preclinical study cohort
Vehicle
AZD6244
Bortezomib
Combo
D
Pre-treatment
Post-treatment
γ/Albumin ratio
8
6
4
2
0
***
***
ns
ns
Vehicle
AZD
BTZ
Combo
E
Veh (n=7)
AZD (n=7)
BTZ (n=3)
Combo (n=6)
RBC count (10⁹/mL)
15
10
5
0
***
*
**
Hb (g/dL)
15
10
5
2.5
***
*
**
Platelet count (10⁶/mL)
1500
1000
500
0
***
***
*
*
F
Survival (%)
100
80
60
40
20
0
0 20 40 60 80
Days after treatment
Vehicle (n=12)
AZD6244 (n=7)
Bortezomib (n=8)
Combo (n=7)
**
*
**

## 2.7 Tables

### Table 2-S1 Summary of VQ mice

**Table-S1 Summary of VQ mice**

| Genotyping | Mouse Types | Disease Types | Lambda | Kappa | IgA | IgM | IgG1 | IgG2a | IgG2b | IgG3 |
|---|---|---|---|---|---|---|---|---|---|---|
| IgG1-Cre | Primary | Healthy | | | | | | | | |
| B2518 (VQ1) | Primary | Multiple Myeloma | | Y | | | | | Y | |
| B2519 (VQ2) | Primary | Multiple Myeloma | | Y | Y | | | | | Y |
| B2576 (VQ3) | Primary | Multiple Myeloma | Y | Y | | | | | | |
| B3520 (VQ4) | Primary | Multiple Myeloma | | Y | Y | | | | | Y |
| B3518 (VQ5) | Primary | Multiple Myeloma | | Y | Y | | | | | Y |
| B2509 | Primary | Other Lymphoid Diseases | | Y | | Y | | Y | Y | |
| B3300 | Primary | Undefined Diseases | | Y | | Y | | | Y | Y |
| VQ-D1 | Recipient | Multiple Myeloma | | Y | | | | | Y | |
| VQ-D2 | Recipient | Multiple Myeloma | | Y | Y | | | | | |
| VQ-D4 | Recipient | Multiple Myeloma | | Y | Y | | | | | |
| VQ-D5 | Recipient | Multiple Myeloma | | Y | Y | | | | | |
| Cell Line | Recipient | Multiple Myeloma | | Y | Y | | | | | |

Note: All serum were diluted at 1:100,000 in PBS containing 1% BSA for isotyping. Y: detected; blank: not detected.

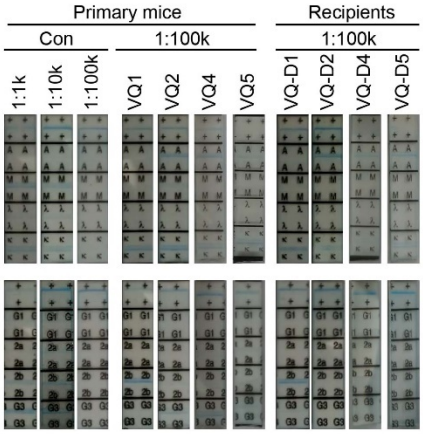


### Table 2-S2 Summary of V mice

**Table-S2 Summary of V mice**

| Ear tag | Survival | WBC (K/uL) | RBC (M/uL) | Hb (g/dL) | PLT (K/uL) | Y/A ratio | BM PC% | SP PC% | LN PC% | Diagnosis |
|---|---|---|---|---|---|---|---|---|---|---|
| N1951 | 659 | 4.16 | 6.12 | 8.8 | 882 | 1.278 | 2.3 | 0.7 | 10.6 | MM |
| B2499 | 590 | 9.56 | 9.34 | 12.8 | 891 | 0.569 | 2.7 | 0.4 | 0.5 | moderate plasma cell disease |
| B3436 (V2) | 388 | 4.92 | 9.1 | 12.1 | 1396 | 0.150 | 0.8 | 0.7 | | moderate plasma cell disease |
| B3224 | 541 | 23.56 | 5.26 | 7.3 | 1547 | 0.420 | 0.2 | 0.6 | 2.2 | moderate plasma cell disease |
| B3463 (V3) | 773 | 5.68 | 9.3 | 11.7 | 1437 | 0.352 | 0.4 | 2 | | moderate plasma cell disease |
| B2440 | 478 | 3.42 | 5.94 | 7.1 | 667 | 0.241 | 0.6 | 0.2 | 0.5 | Diffuse large B cell lymphoma |
| B2444 | 478 | 3.6 | 7.07 | 10.1 | 493 | 0.355 | 1.5 | 0.5 | 0.4 | Diffuse large B cell lymphoma |
| B2489 | 528 | 41.82 | 5.79 | 9 | 945 | 0.202 | 0.3 | 0.3 | 0.1 | Diffuse large B cell lymphoma |
| B3222 | 353 | 16.92 | 13.22 | 13.6 | 212 | 0.343 | 0.4 | 0.1 | 0.5 | Diffuse large B cell lymphoma |
| B3226 | 423 | 19.52 | 7.41 | 8.9 | 275 | 0.096 | 0.3 | 0.0 | 0.1 | Diffuse large B cell lymphoma |
| B3585 (V4) | 613 | 3.9 | 8.51 | 11 | 1086 | 0.406 | 0.50 | 1.00 | | Diffuse large B cell lymphoma |
| B3698 (V5) | 584 | 14.66 | 9.43 | 12.40 | 905.00 | 0.354 | 0.30 | 0.20 | | Diffuse large B cell lymphoma |
| B3256 (V1) | 692 | 3.08 | 10.29 | 13.3 | 1178 | 0.144 | 0.3 | 0.6 | | mild MPN |

**Table 2-S3 List of differentiately expressed genes included in the heatmap (Fig 2-5A)**

| Group-1 | Group-2 | Group-3 | Group-4 |
|---|---|---|---|
| Trf | Slpi | Gemin6 | Emb |
| Ssr2 | Prg2 | Anln | Ramp1 |
| Rps2 | Ly6a | Kif11 | Tyrobp |
| Ubr3 | B2m | Ccnb1 | Arhgdib |
| Ly6c2 | Ly6d | Dhx36 | Dntt |
| Ctsz | Jchain | Top2a | Lcp1 |
| Map4k1 | Mzb1 | Ndufc2 | S100a4 |
| Bmi1 | Trp53inp1 | Ccna2 | S100a6 |
| Epcam | Cd74 | Fabp5 | Ccr2 |
| Erp29 | Chst1 | Rabggtb | Thy1 |
| Rnf187 | Oosp1 | Uqcrb | AW112010 |
| Fkbp11 | Malat1 | Skil | Tmsb4 |
| Lrrn3 | Glipr1 | Ube2c | Lsp1 |
| Mydgf | Tmem154 | Map4k5 | Ifngr1 |
| Pgam2 | Fcrla | Nop58 | Plac8 |
| Selm | Slc3a2 | Myadm | Lgals3 |
| Nhp2 | H2.Ab1 | Ifi47 | Alox5ap |
| Khdc3 | Pqlc3 | | Id2 |
| Entpd1 | Fos | | H2afy |
| Arg1 | Hspa1b | | |
| Tex1001 | | | |
| Ybx3 | | | |
| Eif2a | | | |
| Myc | | | |
| Lyar | | | |
| Nap1l1 | | | |
| ppa1 | | | |
| Crygs | | | |
| Npm1 | | | |
| Slc7a1 | | | |
| Cct3 | | | |
| Gnl3 | | | |
| Ncl | | | |
| Cdt1 | | | |
| Gbp3 | | | |
| Tfdp1 | | | |
| Rrm2 | | | |
| Cyp2b10 | | | |

**Table 2- S4 Mouse orthologs of UAMS-70 gene signature**

**Table-S4 Mouse orthologs of UAMS-70 gene signature**

| Affymetrix probe set (High exp) | Human gene | Mouse gene |
|---|---|---|
| 1555274_a_at | *SELI* | *Ept1* |
| 1555864_s_at | *PDHA1* | *Pdha1* |
| 1565951_s_at | *OPN3* | *Opn3* |
| 200634_at | *PFN1* | *Pfn1* |
| 200638_s_at | *YWHAZ* | *Ywhaz* |
| 200750_s_at | *RAN* | *Ran* |
| 200916_at | *TAGLN2* | *Tagln2* |
| 200966_x_at | *ALDOA* | *Aldoa* |
| 201091_s_at | *CBX3* | *Cbx3* |
| 201105_at | *LGALS1* | *Lgals1* |
| 201231_s_at | *ENO1* | *Eno1* |
| 201614_s_at | *RUVBL1* | *Ruvbl1* |
| 201897_s_at | *CKS1B* | *Cks1B* |
| 201947_s_at | *CCT2* | *Cct2* |
| 202345_s_at | *FABP5* | *Fabp5* |
| 203432_at | *TMPO* | *Tmpo* |
| 204016_at | *LARS2* | *Lars2* |
| 204023_at | *RFC4* | *Rfc4* |
| 204033_at | *TRIP13* | *Trip13* |
| 204092_s_at | *STK6* | *Aurka* |
| 205235_s_at | *MPHOSPH1* | *Mpp1* |
| 206332_s_at | *IFI16* | *Ifi204, Ifi205* |
| 206364_at | *KIF14* | *Kif14* |
| 206513_at | *AIM2* | *Aim2* |
| 208117_s_at | *LAS1L* | *Las1L* |
| 208931_s_at | *ILF3* | *Ilf3* |
| 210334_x_at | *BIRC5* | *Birc5* |
| 210460_s_at | *PSMD4* | *Psmd4* |
| 211576_s_at | *SLCI19A1* | *Rfc1* |
| 212533_at | *WEE1* | *Wee1* |
| 213194_at | *ROBO1* | *Robo1* |
| 213310_at | *EIF2C2* | *Ago2* |
| 213535_s_at | *UBE2I* | *Ube2I* |
| 213607_x_at | *FLJ13052* | *Nadk* |
| 216194_s_at | *CKAP1* | *Tbcb* |
| 217901_at | *DSG2* | *Dsg2* |
| 218947_s_at | *PAPD1* | *Mtpap* |
| 219918_s_at | *ASPM* | *Aspm* |
| 220789_s_at | *TBRG4* | *Tbrg4* |
| 221970_s_at | *DKFZP586L0724* | *Nol11* |
| 222417_s_at | *SNX5* | *Snx5* |
| 224200_s_at | *RAD18* | *Rad18* |
| 224523_s_at | *MGC4308* | *Cmss1* |
| 225082_at | *CPSF3* | *Cpsf3* |
| 225834_at | *MGC57827* | *Fam72a* |
| 226936_at | *C6orf173* | *Cenpw* |
| 238952_x_at | *DKFZp779O175* | *Zfp383* |
| 242488_at | *CHRM3* | *Chrm3* |
| 243011_at | *MGC15606* | *Nxpe3* |
| 244686_at | *TCOF1* | *Tcof1* |
| 58696_at | *EXOSC4* | *Exosc4* |

| Affymetrix probe set (Low exp) | Human gene | Mouse gene |
|---|---|---|
| 1554736_at | *PARG1* | *Arhgap29* |
| 1557277_a_at | *NA* | |
| 200850_s_at | *AHCYL1* | *Ahcyl1* |
| 201921_at | *GNG10* | *Gng10* |
| 202729_s_at | *LTBP1* | *Ltbp1* |
| 202838_at | *FUCA1* | *Fuca1* |
| 209717_at | *EVI5* | *Evi5* |
| 209740_s_at | *PNPLA4* | *Pnpla4* |
| 212435_at | *TRIM33* | *Trim33* |
| 213628_at | *MCLC* | *Clcc1* |
| 218924_s_at | *CTBS* | *Ctbs* |
| 222495_at | *AD-020* | *Tmem167b* |
| 225582_at | *KIAA1754* | *Itprip* |
| 226954_at | *UBE2R2* | *Ube2R2* |
| 227278_at | *TAF13* | *Taf13* |
| 227547_at | *NA* | |
| 230192_at | *RFP2* | *Rfp2* |
| 237964_at | *NA* | |
| 48106_at | *FLJ20489* | *Slc48a1* |

## 2.8 References


1. Kumar SK, Rajkumar V, Kyle RA, et al. Multiple myeloma. Nat Rev Dis Primers. 2017;3:17046.
2. Cowan AJ, Allen C, Barac A, et al. Global Burden of Multiple Myeloma: A Systematic Analysis for the Global Burden of Disease Study 2016. JAMA Oncol. 2018;4(9):1221-1227.
3. Richter J, Jagannath S. Society of Hematologic Oncology State of the Art Update and Next Questions: Multiple Myeloma. Clin Lymphoma Myeloma Leuk. 2018;18(11):693-702.
4. Papadas A, Asimakopoulos F. Mechanisms of Resistance in Multiple Myeloma. Handb Exp Pharmacol. 2018;249:251-288.
5. Weinstock M, Aljawai Y, Morgan EA, et al. Incidence and clinical features of extramedullary multiple myeloma in patients who underwent stem cell transplantation. Br J Haematol. 2015;169(6):851-858.
6. Affer M, Chesi M, Chen WG, et al. Promiscuous MYC locus rearrangements hijack enhancers but mostly super-enhancers to dysregulate MYC expression in multiple myeloma. Leukemia. 2014;28(8):1725-1735.
7. Jovanovic KK, Roche-Lestienne C, Ghobrial IM, Facon T, Quesnel B, Manier S. Targeting MYC in multiple myeloma. Leukemia. 2018;32(6):1295-1306.
8. Chesi M, Robbiani DF, Sebag M, et al. AID-dependent activation of a MYC transgene induces multiple myeloma in a conditional mouse model of post-germinal center malignancies. Cancer Cell. 2008;13(2):167-180.
9. Delmore JE, Issa GC, Lemieux ME, et al. BET bromodomain inhibition as a therapeutic strategy to target c-Myc. Cell. 2011;146(6):904-917.
10. Chesi M, Stein CK, Garbitt VM, et al. Monosomic Loss of MIR15A/MIR16-1 Is a Driver of Multiple Myeloma Proliferation and Disease Progression. Blood Cancer Discovery. 2020.
11. Rasmussen T, Kuehl M, Lodahl M, Johnsen HE, Dahl IM. Possible roles for activating RAS mutations in the MGUS to MM transition and in the intramedullary to extramedullary transition in some plasma cell tumors. Blood. 2005;105(1):317-323.
12. Keats JJ, Fonseca R, Chesi M, et al. Promiscuous mutations activate the noncanonical NF-kappaB pathway in multiple myeloma. Cancer Cell. 2007;12(2):131-144.
13. Chng WJ, Gonzalez-Paz N, Price-Troska T, et al. Clinical and biological significance of RAS mutations in multiple myeloma. Leukemia. 2008;22(12):2280-2284.
14. Lohr JG, Stojanov P, Carter SL, et al. Widespread genetic heterogeneity in multiple myeloma: implications for targeted therapy. Cancer Cell. 2014;25(1):91-101.

15. Kortum KM, Mai EK, Hanafiah NH, et al. Targeted sequencing of refractory myeloma reveals a high incidence of mutations in CRBN and Ras pathway genes. Blood. 2016;128(9):1226-1233.
16. Burd CE, Liu W, Huynh MV, et al. Mutation-specific RAS oncogenicity explains NRAS codon 61 selection in melanoma. Cancer Discov. 2014;4(12):1418-1429.
17. Hennessey RC, Holderbaum AM, Bonilla A, et al. Ultraviolet radiation accelerates NRas-mutant melanomagenesis: A cooperative effect blocked by sunscreen. Pigment Cell Melanoma Res. 2017.
18. Casola S, Cattoretti G, Uyttersprot N, et al. Tracking germinal center B cells expressing germ-line immunoglobulin gamma1 transcripts by conditional gene targeting. Proc Natl Acad Sci U S A. 2006;103(19):7396-7401.
19. Chapman MA, Lawrence MS, Keats JJ, et al. Initial genome sequencing and analysis of multiple myeloma. Nature. 2011;471(7339):467-472.
20. Chan IT, Kutok JL, Williams IR, et al. Conditional expression of oncogenic K-ras from its endogenous promoter induces a myeloproliferative disease. J Clin Invest. 2004;113(4):528-538.
21. Braun BS, Tuveson DA, Kong N, et al. Somatic activation of oncogenic Kras in hematopoietic cells initiates a rapidly fatal myeloproliferative disorder. Proc Natl Acad Sci U S A. 2004;101(2):597-602.
22. Zhang J, Wang J, Liu Y, et al. Oncogenic Kras-induced leukemogeneis: hematopoietic stem cells as the initial target and lineage-specific progenitors as the potential targets for final leukemic transformation. Blood. 2009;113(6):1304-1314.
23. Wang JY, Liu YG, Li ZY, et al. Endogenous oncogenic Nras mutation leads to aberrant GM-CSF signaling in granulocytic/monocytic precursors in a murine model of chronic myelomonocytic leukemia. Blood. 2010;116(26):5991-6002.
24. Li Q, Haigis KM, McDaniel A, et al. Hematopoiesis and leukemogenesis in mice expressing oncogenic NrasG12D from the endogenous locus. Blood. 2011;117(6):2022-2032.
25. Wang JY, Liu YG, Li ZY, et al. Endogenous oncogenic Nras mutation initiates hematopoietic malignancies in a dose- and cell type-dependent manner. Blood. 2011;118(2):368-379.
26. Xu J, Haigis KM, Firestone AJ, et al. Dominant role of oncogene dosage and absence of tumor suppressor activity in Nras-driven hematopoietic transformation. Cancer Discov. 2013;3(9):993-1001.
27. Kong G, Chang YI, You X, et al. The ability of endogenous Nras oncogenes to initiate leukemia is codon-dependent. Leukemia. 2016;30(9):1935-1938.

28. Kong G, Wunderlich M, Yang D, et al. Combined MEK and JAK inhibition abrogates murine myeloproliferative neoplasm. J Clin Invest. 2014;124(6):2762-2773.
29. Lin YT, Way GP, Barwick BG, et al. Integrated phosphoproteomics and transcriptional classifiers reveal hidden RAS signaling dynamics in multiple myeloma. Blood Adv. 2019;3(21):3214-3227.
30. Chng WJ, Huang GF, Chung TH, et al. Clinical and biological implications of MYC activation: a common difference between MGUS and newly diagnosed multiple myeloma. Leukemia. 2011;25(6):1026-1035.
31. Chang Y, Paige CJ, Wu GE. Enumeration and characterization of DJH structures in mouse fetal liver. EMBO J. 1992;11(5):1891-1899.
32. Hsu J, Shi Y, Krajewski S, et al. The AKT kinase is activated in multiple myeloma tumor cells. Blood. 2001;98(9):2853-2855.
33. Chesi M, Matthews GM, Garbitt VM, et al. Drug response in a genetically engineered mouse model of multiple myeloma is predictive of clinical efficacy. Blood. 2012;120(2):376-385.
34. Kim D, Park CY, Medeiros BC, Weissman IL. CD19-CD45 low/- CD38 high/CD138+ plasma cells enrich for human tumorigenic myeloma cells. Leukemia. 2012;26(12):2530-2537.
35. Guillerey C, Harjunpaa H, Carrie N, et al. TIGIT immune checkpoint blockade restores CD8(+) T-cell immunity against multiple myeloma. Blood. 2018;132(16):1689-1694.
36. Harjunpaa H, Blake SJ, Ahern E, et al. Deficiency of host CD96 and PD-1 or TIGIT enhances tumor immunity without significantly compromising immune homeostasis. Oncoimmunology. 2018;7(7):e1445949.
37. Minnie SA, Kuns RD, Gartlan KH, et al. Myeloma escape after stem cell transplantation is a consequence of T-cell exhaustion and is prevented by TIGIT blockade. Blood. 2018;132(16):1675-1688.
38. Ledergor G, Weiner A, Zada M, et al. Single cell dissection of plasma cell heterogeneity in symptomatic and asymptomatic myeloma. Nat Med. 2018;24(12):1867-1876.
39. Lam WY, Jash A, Yao CH, et al. Metabolic and Transcriptional Modules Independently Diversify Plasma Cell Lifespan and Function. Cell Rep. 2018;24(9):2479-2492 e2476.
40. Zhan F, Huang Y, Colla S, et al. The molecular classification of multiple myeloma. Blood. 2006;108(6):2020-2028.
41. Shaughnessy JD, Jr., Zhan F, Burington BE, et al. A validated gene expression model of high-risk multiple myeloma is defined by deregulated expression of genes mapping to chromosome 1. Blood. 2007;109(6):2276-2284.

42. Mulligan G, Lichter DI, Di Bacco A, et al. Mutation of NRAS but not KRAS significantly reduces myeloma sensitivity to single-agent bortezomib therapy. Blood. 2014;123(5):632-639.
43. Besse A, Besse L, Kraus M, et al. Proteasome Inhibition in Multiple Myeloma: Head-to-Head Comparison of Currently Available Proteasome Inhibitors. Cell Chem Biol. 2019;26(3):340-351 e343.
44. Kakadia S, Yarlagadda N, Awad R, et al. Mechanisms of resistance to BRAF and MEK inhibitors and clinical update of US Food and Drug Administration-approved targeted therapy in advanced melanoma. Onco Targets Ther. 2018;11:7095-7107.
45. Mirguet O, Gosmini R, Toum J, et al. Discovery of epigenetic regulator I-BET762: lead optimization to afford a clinical candidate inhibitor of the BET bromodomains. J Med Chem. 2013;56(19):7501-7515.
46. Abedin SM, Boddy CS, Munshi HG. BET inhibitors in the treatment of hematologic malignancies: current insights and future prospects. Onco Targets Ther. 2016;9:5943-5953.
47. Heuck CJ, Jethava Y, Khan R, et al. Inhibiting MEK in MAPK pathway-activated myeloma. Leukemia. 2016;30(4):976-980.
48. Chang YI, Damnernsawad A, Kong G, You X, Wang D, Zhang J. The mystery of oncogenic KRAS: Lessons from studying its wild-type counter part. Small GTPases. 2016:1-4.
49. Wang J, Liu Y, Tan LX, et al. Distinct requirements of hematopoietic stem cell activity and Nras G12D signaling in different cell types during leukemogenesis. Cell Cycle. 2011;10(17):2836-2839.
50. Malumbres M, Barbacid M. RAS oncogenes: the first 30 years. Nat Rev Cancer. 2003;3(6):459-465.
51. You X, Kong G, Ranheim EA, Yang D, Zhou Y, Zhang J. Unique dependence on Sos1 in Kras (G12D) -induced leukemogenesis. Blood. 2018;132(24):2575-2579.

**Materials & Methods References**

1. Chesi M, Robbiani DF, Sebag M, et al. AID-dependent activation of a MYC transgene induces multiple myeloma in a conditional mouse model of post-germinal center malignancies. *Cancer Cell*. 2008;13(2):167-180.
2. Kong G, Chang YI, You X, et al. The ability of endogenous Nras oncogenes to initiate leukemia is codon-dependent. *Leukemia*. 2016;30(9):1935-1938.
3. Damnernsawad A, Kong G, Wen Z, et al. Kras is Required For Adult Hematopoiesis. *Stem Cells*. 2016;34(7):1859-1871.

4. Wang JY, Liu YG, Li ZY, et al. Endogenous oncogenic Nras mutation leads to aberrant GM-CSF signaling in granulocytic/monocytic precursors in a murine model of chronic myelomonocytic leukemia. *Blood*. 2010;116(26):5991-6002.
5. Kong G, Wunderlich M, Yang D, et al. Combined MEK and JAK inhibition abrogates murine myeloproliferative neoplasm. *J Clin Invest*. 2014;124(6):2762-2773.
6. Chang Y, Paige CJ, Wu GE. Enumeration and characterization of DJH structures in mouse fetal liver. *EMBO J*. 1992;11(5):1891-1899.
7. Wen Z, Pyeon D, Wang Y, Lambert P, Xu W, Ahlquist P. Orphan nuclear receptor PNR/NR2E3 stimulates p53 functions by enhancing p53 acetylation. *Mol Cell Biol*. 2012;32(1):26-35.
8. Butler A, Hoffman P, Smibert P, Papalexi E, Satija R. Integrating single-cell transcriptomic data across different conditions, technologies, and species. *Nat Biotechnol*. 2018;36(5):411-420.
9. Tirosh I, Izar B, Prakadan SM, et al. Dissecting the multicellular ecosystem of metastatic melanoma by single-cell RNA-seq. *Science*. 2016;352(6282):189-196.
10. Waltman L, van Eck NJ. A smart local moving algorithm for large-scale modularity-based community detection. *Eur Phys J B*. 2013;86:471.
11. Maaten Lvd, Hinton G. Visualizing Data using t-SNE. *J Mach Learn Res* 2008;9:2579–2605.
12. Subramanian A, Tamayo P, Mootha VK, et al. Gene set enrichment analysis: a knowledge-based approach for interpreting genome-wide expression profiles. *Proc Natl Acad Sci U S A*. 2005;102(43):15545-15550.
13. Liberzon A, Subramanian A, Pinchback R, Thorvaldsdottir H, Tamayo P, Mesirov JP. Molecular signatures database (MSigDB) 3.0. *Bioinformatics*. 2011;27(12):1739-1740.
14. Shaughnessy JD, Jr., Zhan F, Burington BE, et al. A validated gene expression model of high-risk multiple myeloma is defined by deregulated expression of genes mapping to chromosome 1. *Blood*. 2007;109(6):2276-2284.
15. Dobin A, Davis CA, Schlesinger F, et al. STAR: ultrafast universal RNA-seq aligner. *Bioinformatics*. 2013;29(1):15-21.
16. Love MI, Huber W, Anders S. Moderated estimation of fold change and dispersion for RNA-seq data with DESeq2. *Genome Biol*. 2014;15(12):550.
17. Stephens M. False discovery rates: a new deal. *Biostatistics*. 2017;18(2):275-294.
18. Yu G, Wang LG, Han Y, He QY. clusterProfiler: an R package for comparing biological themes among gene clusters. *OMICS*. 2012;16(5):284-287.

19. Ashburner M, Ball CA, Blake JA, et al. Gene ontology: tool for the unification of biology. The Gene Ontology Consortium. *Nat Genet*. 2000;25(1):25-29.
20. The Gene Ontology C. The Gene Ontology Resource: 20 years and still GOing strong. *Nucleic Acids Res*. 2019;47(D1):D330-D338.
21. Jassal B, Matthews L, Viteri G, et al. The reactome pathway knowledgebase. *Nucleic Acids Res*. 2020;48(D1):D498-D503.
22. Zhang J, Lodish HF. Identification of K-ras as the major regulator for cytokine-dependent Akt activation in erythroid progenitors in vivo. *Proc Natl Acad Sci U S A*. 2005;102(41):14605-14610.

# Chapter 3

# Mutant *p53* synergizes with oncogenic *Nras* to downregulate *Gata*-network and promote AML

Taylor Klungness (BS, Biochemistry, UW-Madison), Undergraduate Research Assistant has contributed to this study.

### 3.1 Abstract

Concurrent mutations in *TP53* and *RAS* pathway in acute myeloid leukemia patients confer an inferior overall survival compared to patients with single pathway mutations. Majority of these *TP53* mutations in occur in the DNA-binding domain region, resulting in a single amino acid substitution at 'hot spots'. Though several studies have demonstrated a neomorphic function of *p53* missense mutants in solid tumors, there is still a lack of consensus in the context of hematological malignancies. Previously, we reported that loss of *p53* synergizes with oncogenic *Nras* to promote AML. In this study, we investigated the genetic interaction between *p53* missense mutant ($p53^{R172H}$) and endogenous $Nras^{G12D}$. We found that $p53^{mut}$ synergizes with oncogenic *Nras* to induce a fully penetrant AML in primary mice that is serially transplantable. Surprisingly, moribund AML mice retained the wild-type alleles of both *Nras* and *p53.* Underlying cellular and molecular mechanisms through which $p53^{mut}$ promotes transformation of $Nras^{G12D}$ were distinct from loss of *p53*. Unlike $p53^{-/-}$, $p53^{mut}$ did not further expand $Nras^{G12D}$ myeloid progenitor populations or alter cell cycle status. $p53^{mut}$; $Nras^{G12D}$ had hyperactivated basal and cytokine induced ERK signaling. While $p53^{mut}$; $Nras^{G12D}$ LSK were fully transformed, both MEP & GMP were partially transformed. RNA-sequencing revealed a strong MPP gene signature displayed by $p53^{mut}$ driven AML in the background of oncogenic *Nras*. There is minimal overlap between the transformed $Nras^{G12D}$ transcriptomes driven by *p53* loss and *p53* missense mutant, thus suggesting distinct mechanisms of synergism. $p53^{mut}$; $Nras^{G12D}$ upregulated expression of several receptor tyrosine kinases potentially driving hyperactivated ERK signaling. Interestingly, we found a strong inflammatory signature in $p53^{mut}$; $Nras^{G12D}$ transcriptome with activation of Toll-like receptor pathways. We identify dysregulation of key hematopoietic transcription factor networks (*Gata2* and *Runx1*) as an underlying molecular mechanism in $p53^{mut}$ transformed $Nras^{G12D}$ AML.

### 3.2 Introduction

Acute myeloid leukemia (AML) is an aggressive hematopoietic cancer characterized by infiltration of bone marrow and other secondary hematopoietic organs by malignantly transformed cells of myeloid origin leading to bone marrow failure and death (1). Accumulation of recurrent genetic alterations with age results in clonal expansion of myeloblasts, with >20% in marrow or blood designated as AML by World Health Organization (WHO) guidelines. Based on clinical ontogeny, AML can be classified into 3 distinct categories: secondary AML (s-AML) refers to transformation of a previous diagnosis of myelodysplastic syndrome (MDS) or myeloproliferative neoplasm (MPN), therapy-related AML (t-AML) occurs after a previous exposure to leukemogenic therapy, and de novo AML is not preceded by any hematologic disorder or therapy exposure (13). Current standard of care for AML includes induction therapy with cytarabine and an anthracycline, a regimen dubbed '7+3', referring to the 7-day continuous infusion of cytarabine and daunorubicin (anthracycline) on days 1-3. Post induction therapy, patients are advised to either continue consolidative chemotherapy or allogeneic hematopoietic stem cell transplantation (HSCT) based on risk-stratification. Although this approach is curative for 35-40% of younger patients (60 years of age or younger), the outcome for older patients still remains dismal with a median survival of only 5-10 months (2, 3). Poor therapeutic outcomes may be partly attributed to the complex genetic heterogeneity whose mechanisms need to be properly understood in order to be capitalized on for therapeutic benefit.

The tumor suppressor protein p53 plays an important role in regulating key processes such as cell cycle progression, senescence, and apoptosis to prevent tumorigenesis in response to cellular stressors such as DNA damage (4). p53 regulates quiescence and self-renewal of hematopoietic stem/progenitor cells and hence is crucial for maintenance of a normal stem cell pool (5). Disruption of normal p53 function can occur due to loss of wild type allele(s) and/or mutations that can exert dominant-negative or confer gain-of-function properties (6, 7). While rare

in CMML (<1%), somatic *TP53* mutations in AML range from ~8% in de novo cases to over 20% in t-AML (27-28, 8-9). In AML, *TP53* mutations are more commonly associated with a complex karyotype (presence of at least three distinct chromosomal abnormalities in more than one metaphase) with a mutation rate of ~70% (10). *TP53* mutations with complex karyotype and independently correlate with poor overall survival and resistance to chemotherapy (10, 11). Furthermore, MDS patients with *TP53* mutations have high rate of relapse after allogeneic transplantation (12). Mice engineered to lack or express mutant form of p53 are prone to early onset of tumor development of which a high percentage are T or B cell lymphomas (14-17*).* This suggests that p53 mutations may require additional genetic events to promote myeloid cancers as evidenced by previous studies from our lab and others (18, 19, 41).

*RAS* pathway mutations are more prevalent in MDS/MPN overlap disorders such as chronic myelomonocytic leukemia (CMML) and its juvenile counterpart JMML, with *NRAS* alone mutated in ~19% and ~17% respectively (20). While these mutations are founding events in JMML, they can be either initiating or secondary events in CMML (21, 22-23). In CMML, *RAS* pathway mutations are predominant in the proliferative subtype and predict inferior survival (24-25, 26-27). *RAS* mutations are common in AML with a frequency range of 15-40%, of which *NRAS* is most predominant (≥ 10%) (8, 20, 29, 31). Though the prognostic effect of *NRAS* mutations on patient survival is inconclusive, they have been associated with high co-mutational rate and therapy resistance suggesting an underlying complex molecular mechanism (30-35, 36- 38). We and others have shown that mice transplanted with $Nras^{G12D}$ bone marrow cells develop a highly penetrant CMML-like disease after a prolonged latency (39, 40). However, none of the diseased mice spontaneously transform to AML, suggesting requirement of additional genetic events to promote malignancy.

*NRAS* and *TP53* mutations co-occur in a subset of MDS patients (3/43) and deletion of negative regulators of *RAS* pathway (*NF1*, *SPRY4*) co-occur with deletion and/or mutation of

*TP53* in a subset of AML patients (41,42). Detailed examination of recurring driver gene mutations in a large cohort of 1540 AML patients yielded a frequency of ~1.5% (23/1540) of concurrent *TP53* and *RAS* pathway (*NRAS, KRAS, CBL, PTPN11, NF1 and BRAF)* mutations (Table S5, (11)). Although the combined effect of these mutations on patient survival is unclear, the majority of the 23 samples (~70%) harbored a complex karyotype, an adverse prognostic factor (Table S6, (11)). Previously, we reported that a small fraction of patients (8/1238) had mutations in both *TP53* and *RAS* pathway (*NRAS, KRAS, CBL*) genes (19). Majority of these patients were diagnosed with sAML or AML with MDS related changes and had a complex karyotype, thus alluding to a possible cooperation between the two pathways to aid malignant transformation. Despite the low frequency, the combination of *TP53-RAS* pathway mutations predicted a poor overall survival (median 85 days), significantly shorter than that of single mutant patients (*TP53* mutations: 271 days, *RAS* pathway mutations: undetermined). Majority of the mutations in *TP53* were missense or nonsense mutations. We further validated this observation through analysis of publicly available AML dataset from The Cancer Genome Atlas (TCGA), where 6 out of 191 evaluated samples had genetic alterations in both *TP53* and *RAS* pathway with a short overall survival of 3 months, compared to 7 and 19 months for *TP53* (n=11) or *RAS* pathway (n=29) altered patients, respectively. Taken together, these data suggest that co-occurrence of mutations in both *TP53* and *RAS* pathway may predict a dismal overall survival in human AML.

Mutations in *TP53* gene occur mostly in the DNA binding domain region, majority of which are missense mutations that result in a single amino acid substitution at hot spots e.g., R175, R248, R273 (43, 44, 10). These missense mutations can be broadly classified into two types- mutations in amino acids that directly contact DNA (e.g., R273H) and thus disrupt wild-type p53 transcriptional activity without affecting the protein conformation are called DNA-contact mutants, while those that alter the three-dimensional structure are called structural/conformational mutants (e.g., R172H). Previous studies have shown that these missense mutations can confer distinct

gain-of-function properties at molecular, cellular and organism level (16, 17, 45, 46). We previously showed that loss of *p53* and oncogenic *Nras*$^{G12D}$ synergize to transform megakaryocyte-erythroid progenitors (MEP) and promote AML in mice (19). In this study, we investigated whether *p53*$^{R172H}$ missense mutation can cooperate with endogenous oncogenic Nras signaling to promote hematological malignancy. Our research shows a strong synergy between *p53* missense mutant and oncogenic *Nras* that promotes a fully penetrant, aggressive AML through mechanisms distinct from loss of *p53.*

### 3.3 Materials and methods

#### Mice

All mouse lines were maintained in a pure C57BL/6 genetic background (>N10). Mice bearing a conditional oncogenic Nras (Nras $^{\text{Lox-stop-Lox (LSL) G12D/+}}$) were crossed to Mx1-Cre mice to generate mice carrying both alleles (Nras$^{\text{LSL G12D/+}}$; Mx1-Cre). The p53 conditional mutant mice (p53$^{\text{Lox-stop-Lox (LSL) R172H/+}}$) were obtained from NCI (strain number 01XAF) and crossed with Mx1-Cre to generate p53$^{\text{LSL-R172H/+}}$; Mx1-Cre mice which were crossed with Nras$^{\text{LSL-G12D/+}}$ or Nras$^{\text{LSL-G12D/LSL-G12D}}$ mice to generate compound mice Nras$^{\text{LSL-G12D/+}}$; p53$^{\text{R172H/+}}$; Mx1-Cre. Genotyping of NrasG12D/+ and Mx1-Cre was done as previously described [19]. Genotyping of p53$^{\text{R172H}}$ and recombined allele was performed per the instructions of NCI, and as previously described [16]. CD45.1+ congenic recipient mice were purchased from NCI.

To induce Cre expression, 6-7 week old mice were injected intraperitoneally (i.p.) with 100 µg of polyinosinic-polycytidylic acid (pI-pC; GE Healthcare) every other day for three times. The day of the first pI-pC injection was defined as Day 1. All experiments were performed on Day 12. The PCR analysis of recombination efficiency at the p53 locus was performed as previously described [16]. All experiments were conducted in accordance with the Guide for the Care and Use of Laboratory Animals and approved by Animal Care and Use Committee at the University of

Wisconsin, Madison. The program is accredited by the Association for Assessment and Accreditation of Laboratory Animal Care.

**Murine bone marrow transplantation**

1 x $10^6$ total bone marrow cells (CD45.2+) were mixed with same number of congenic bone marrow cells (CD45.1+) and injected into individual lethally irradiated mice (8Gy) as previously described [19]. MEPs and GMPs were sorted using a FACS AriaII (BD Biosciences) as described in [19]. Purified MEPs or GMPs (CD45.2+) were transplanted with 2 x $10^5$ whole bone marrow cells (CD45.1+) into individual lethally irradiated mice.

At the moribund stage, 1 x $10^6$ bone marrow or spleen cells from recipients with AML were transplanted into individual sublethally irradiated mice (4 Gy).

**Flow cytometric analysis of hematopoietic tissues**

For lineage analysis of bone morrow, spleen and peripheral blood, flow cytometric analyses were performed as previously described [19]. HSCs, MPPs, LSK and MPs in bone marrow and spleen were analyzed as previously described [19]. LT-HSC, ST-HSC, MPP2, MPP3, MPP4 in bone marrow and spleen were analyzed as previously described [50]. Stained cells were analyzed on a FACS Fortessa or LSRII (BD Biosciences).

Directly conjugated or biotin conjugated antibodies against the following surface antigens were purchased from eBioscience: CD45.1 (A20), CD45.2 (104), Mac-1 (M1/70), Gr-1 (RB6-8C5), CD3 (145-2C11), CD4 (RM4-5), CD8 (53-6.7), CD19 (eBio1D3), Thy1.2 (53-2.1), TER119 (TER-119), B220 (RA3-6B2), IgM (eB121-15F9), IL-7Rα (B12-1), CD41 (eBioMWReg30), CD48 (HM48-1), Sca1 (D7), c-Kit (2B8), and CD34 (clone RAM34). FcγRII/III (2.4G2) was purchased from BD Biosciences. CD150 (TC15-12F12.2) was purchased from Biolegend.

**Cell cycle analysis**

Cell cycle analysis was performed essentially as described [19]. Fixed cells were simultaneously stained with PECy7-conjugated antibodies against CD48, B220, TER119 and Gr1, PE-CD150, APC-c-Kit, PerCP Cy5.5-Sca1, FITC-Ki67 (BD Biosciences), and DAPI (Invitrogen). The stained cells were analyzed on a Fortessa or LSRII (BD Biosciences).

**Flow cytometric analysis of phospho-ERK1/2 and phosphor-Stat5**

Phosphorylated ERK1/2 and Stat5 (p-ERK1/2 and p-Stat5) were analyzed in defined Lin-/low c-Kit+ and Lin-/low c-Kit- cells essentially as previously described [19]. Surface proteins were detected with FITC-conjugated antibodies (BD Biosciences unless specified) against B220 (6B2), Gr-1 (RB6-8C5), CD3 (17A2, Biolegend), CD4 (RM4-5), CD8 (53-6.7), and TER119, and PE-conjugated anti-CD117/c-Kit antibody (eBiosciences, San Diego, CA). p-ERK1/2 was detected by a primary antibody against p-ERK (Thr202/Tyr204; Cell signaling Technology) followed by APC conjugated donkey anti-rabbit F(ab')2 fragment (Jackson ImmunoResearch). p-Stat5 (pY694) was detected by Alexa 647 conjugated primary antibody against p-Stat5 (BD Biosciences).

**Complete blood count and histopathology**

Complete blood count analysis was performed using a Hemavet 950FS (Drew Scientific). Mouse tissues were fixed in 10% neutral buffered formalin (Sigma-Aldrich) and further processed at the UWCCC Histology Lab.

**Colony assay and replating assay**

5 x $10^4$ bone marrow cells were plated in duplicate in semisolid medium MethoCult M3234 (StemCell Technologies) supplemented with mGM-CSF or mIL-3 (Peprotech, Rocky Hill, NJ) according to the manufacture's protocol. The colonies were counted after 7 to 10 days in culture. Then colonies were harvested to repeat the same procedure for serial replating.

**RNA-Seq and data analysis**

Total RNAs were isolated from 50,000 sorted Lin$^-$ cKit$^+$ bone marrow cells of age-matched control (n=3), *p53$^{mut}$* (n=3), *Nras$^{G12D}$* (n=3) and moribund *p53$^{mut}$; Nras$^{G12D}$* (n=4) mice using RNeasy Micro Kit (Qiagen). RNA-Seq libraries were prepared using SMARTer® Stranded Total RNA-Seq Kit v1 - Pico Input Mammalian (Takara Bio USA/Clontech). Sequencing was performed on an Illumina HiSeq 4000 system at the NUSeq Core facility. The raw sequence reads were mapped to the genome using Subjunc aligner from Subread. The alignment bam files were compared against the gene annotation GFF file, and raw counts for each gene were generated using the featureCounts tool from subread. The raw counts data were normalized using voom method from the R Limma package, then used for differential expression analysis. Statistics for differential expression analysis were computed using R Limma package. The statistics values include log fold change (logFC), p-value, and false discovery rate (FDR, shown as adj.p.value). The FDR values comes from P-values corrected for multiple hypothesis testing with Benjamini-Hochberg procedure. Gene sets from the Broad Institute's Molecular Signatures Database or published datasets were used to perform GSEA analysis to identify enriched functional categories.

**qRT-PCR validation of differentially expressed genes**

Lin$^-$ cKit$^+$ cells from moribund *p53$^{mut}$; Nras$^{G12D}$* (n=4) with AML and age-matched control were flow sorted into RNAprotect Cell Reagent (Qiagen). Total RNAs were extracted using RNeasy Micro Kit (Qiagen). cDNAs were synthesized using iScript™ Reverse Transcription Kit (Bio-Rad). Real-time PCR reactions were performed on a CFX96 Real-Time System (Bio-Rad) using the primers specific for Lgals3 (F: 5'- TTGAAGCTGACCACTTCAAGGTT-3', R: 5'-AGGTTCTTCATCCGATGGTTGT-3'), CD74 (F: 5'- CATGGATGACCAACGCGAC-3', R: 5'-TGTACAGAGCTCCACGGCTG-3'), Klf4 (F: 5'- GTGCCCCGACTAACCGTTG-3', R: 5'-GTCGTTGAACTCCTCGGTCT-3'), Ctss (F: 5'- ATGGCTGTTTTGGATGCCCC-3', R: 5'-TTCCCAGATGAGACGCCGTA-3'), Nfkbia (F: 5'- GAAGCCGCTGACCATGGAA-3', R: 5'-

GATCACAGCCAAGTGGAGTGGA-3'), Csf1r (F: 5'- CAGTTCAGAGTGATGTGTGGTC-3', R: 5'-CTTGTTGTTCACTAGGATGCCG-3'), (Integrated DNA Technologies, Inc). The cycling condition is: 95 °C 3 min, (95 °C 15 sec, 60 °C 1 min) x 40 cycles). GAPDH was chosen as the house keeping gene as previously described (72).

**Quantification of inflammatory cytokines**

Serum was collected from ~8 week old primary *p53$^{mut}$; Nras$^{G12D}$*, age matched control, and *p53$^{mut}$; Nras$^{G12D}$*- BMT mice (8 weeks post transplantation) and diluted 3 fold before assaying with MSD Cytokine Assays Proinflammatory Panel 1 V-Plex (mouse) kits (Cat # K15048D). A panel of 10 pro-inflammatory cytokines were measured with the diluted serum sample by first pre-incubating with detection antibodies conjugated with electrochemiluminescent labels, then adding to a plate pre-coated with capture antibodies on independent spots and read on an MSD MESO QUICKPLEX SQ 120 multiplex cytokine plate reader to quantify cytokine levels.

## 3.4 Results

### Expression of *p53$^{mut}$* and oncogenic *Nras* synergize to induce a highly penetrant AML

To explore potential genetic interactions between *p53* missense mutant and oncogenic Nras signaling, we generated *Mx1-Cre*, *Mx1-Cre; p53$^{LSL-R172H/+}$, Mx1-Cre; Nras$^{LSL-G12D/+}$, and Mx1-Cre; p53$^{LSL-R172H/+}$; Nras$^{LSL-G12D/+}$* mice (Figure S1A). At 6 to 8 weeks old, these mice were given pI-pC as described in "Materials and methods" to induce the expression of oncogenic *Nras* and *p53* missense mutant from their respective endogenous loci simultaneously. The day of the first pI-pC injection was assigned as day 1 and the mice were monitored till moribundity. Unexpectedly, ~90% of *Mx1-Cre; p53$^{LSL-R172H/+}$; Nras$^{LSL-G12D/+}$* mice did not survive pI-pC injections; they were either found dead or became moribund (Figure S1B). Upon evaluation of recombination efficiency in whole bone marrow cells (WBM) of these mice, we found that majority of the cells expressed the recombined 1loxp alleles of both oncogenic *Nras* and *p53* missense mutant (Figure S1C). This is reminiscent of the *Kras$^{LSL-G12D/+}$; Dnmt3$^{fl/fl}$; Mx1-Cre* mice that died rapidly after 1$^{st}$ pI-pC injection, likely due to leaky expression of Cre and amplified responses to the interferon signaling (63). Therefore, we refrained from administering pI-pC to *Mx1-Cre; p53$^{LSL-R172H/+}$; Nras$^{LSL-G12D/+}$* mice throughout this study. As the other groups of mice do not have sufficient recombination efficiency without pI-pC injection (data not shown), we continued to treat these mice. We refer to the pI-pC treated mice as Control (*Mx1-Cre*), *p53$^{mut}$* and *Nras$^{G12D}$*, and untreated double mutant mice as *p53$^{mut}$; Nras$^{G12D}$* for the rest of the study. As expected, majority of *p53$^{mut}$; Nras$^{G12D}$* WBM cells from moribund mice expressed the recombined 1loxp *Nras$^{G12D}$* and *p53$^{R172H}$* alleles and, more importantly, retained the wild-type *Nras* and *p53* alleles (Figure S1D).

Expression of *p53* missense mutant significantly decreased the survival of *Nras$^{G12D}$* mice (Figure 1 A). The median survival days of *p53$^{mut}$* mice and *Nras$^{G12D}$* mice were ~530 days and 480 days respectively, consistent with our and others' previous reports (19, 40). By contrast, all

*p53*$^{mut}$*; Nras*$^{G12D}$ mice died rapidly with a median survival of ~80 days, significantly shorter than control, *p53*$^{mut}$ and *Nras*$^{G12D}$ groups.

We next evaluated the *p53*$^{R172H}$*; Nras*$^{G12D}$ mice at the moribund stage and compared their characteristics with age-matched control. The moribund *p53*$^{R172H}$*; Nras*$^{G12D}$ mice had increased monocytes and neutrophils in the bone marrow and peripheral blood respectively, with a concomitant decrease in lymphoid compartments (Figure 1 B-C). We observed marked hepatosplenomegaly, expansion of myeloid compartment in the spleen with both spleen and liver infiltrated with myeloid blast cells, indicating an AML-like disease (Figure 1D-E, Figure S2). Unlike the disease spectrum of moribund *p53*-null, *p53*$^{R172H/-}$, and *p53*$^{-/-}$*; Nras*$^{G12D}$ mice (19, 46, (Donehower et al., 1995)), we did not observe any T-cell lymphoblastic leukemia/lymphoma (T-ALL) in *p53*$^{mut}$*; Nras*$^{G12D}$ mice. Rather, none of these mice had an observable thymus (Figure 1D). To determine whether the AML was transplantable, we injected 1 x $10^6$ WBM cells from moribund *p53*$^{mut}$; *Nras*$^{G12D}$ mice or age-matched control with equal number of CD45.1$^+$ helper cells into lethally irradiated recipients. Analysis of peripheral blood every 4 weeks after transplantation showed that percentage of donor-derived cells (CD45.2$^+$) in *p53*$^{mut}$; *Nras*$^{G12D}$ recipients was higher (>60%) compared to recipients with control cells (Figure S3A). All the *p53*$^{mut}$; *Nras*$^{G12D}$ recipient mice succumbed to AML within 100 days with characteristics similar to primary mice, including splenomegaly, myeloid-cell-infiltrated liver, and lack of thymus (Figure 1G, data not shown). The AML is also serially transplantable into secondary recipients from both WBM and splenocytes of moribund primary recipients (Figure S3B). Additionally, to determine whether the induced AML was the result of cell-autonomous interaction between mutant *p53*$^{R17H/+}$ and oncogenic *Nras*$^{G12D/+}$, we repeated the transplantation with 2.5 x $10^5$ bone marrow cells isolated from ~6 weeks old *p53*$^{mut}$*; Nras*$^{G12D}$ and age-matched control into individual lethally irradiated CD45.1$^+$ recipient mice. 100% of recipients developed AML with hepatosplenomegaly (data not shown). Consistent with our and previous reports, the *p53*$^{mut}$ primary mice developed a combination of sarcoma and

myeloid diseases while *Nras*$^{G12D}$ mice predominantly developed only myeloid diseases (data not shown) (16, 40, 47). Taken together, we report that *p53*$^{mut}$ cooperates with oncogenic *Nras* to promote AML.

### *p53*$^{mut}$; *Nras*$^{G12D}$ mice display a similar expansion of multipotent progenitors as seen in *Nras*$^{G12D}$ mice

To understand the underlying cellular mechanisms contributing to the highly penetrant AML in *p53*$^{mut}$; *Nras*$^{G12D}$ mice, we analyzed the hematopoietic cell compartment of control, *p53*$^{mut}$, *Nras*$^{G12D}$ and *p53*$^{mut}$; *Nras*$^{G12D}$ mice on Day 12 when most of double mutant mice were still alive (Figure S4A). After acute induction of Cre expression, the *p53*$^{mut}$ mice were largely similar to control, while *Nras*$^{G12D}$ and *p53*$^{mut}$; *Nras*$^{G12D}$ mice displayed signs of myeloid diseases to different degrees (data not shown). Interestingly, *p53*$^{mut}$; *Nras*$^{G12D}$ mice still had an observable thymus at this stage, albeit relatively smaller in size, indicating that thymic regression probably occurred gradually during leukemogenesis (Figure S4B).

We investigated how *p53*$^{mut}$ affects hematopoietic stem and progenitor cells (HSPCs), using the definition of hematopoietic stem cells (HSCs) and multipotent progenitors (MPPs) delineated in Pietras et al (50) (Figure 2A). Briefly, within LSK population (Lin$^-$ Sca1$^+$ cKit$^+$), long-term HSCs (LT-HSC) and short-term HSCs (ST-HSC) are defined as Flk2$^-$ CD48$^-$ CD150$^+$ LSK and Flk2$^-$ CD48$^-$ CD150$^-$ LSK respectively. The myeloid-biased MPPs are defined as megakaryocyte biased MPP2: Flk2$^-$ CD150$^+$ CD48$^+$ LSK, granulocyte-macrophage biased MPP3: Flk2$^-$ CD150$^-$ CD48$^+$ LSK, and the lymphoid primed MPP4 is gated as: Flk2$^+$ CD150$^-$ CD48$^{+/-}$ LSK. Both *Nras*$^{G12D}$ bone marrow and spleen had a significantly expanded LSK compartment compared to control as previously noted (Figure 2B) (19). *p53*$^{mut}$; *Nras*$^{G12D}$ LSK numbers were comparable to *Nras*$^{G12D}$ in both spleen and marrow. Unexpectedly, cell cycle analysis using Ki67 and DAPI showed that despite being as proliferative as control LSKs, *p53*$^{mut}$; *Nras*$^{G12D}$ LSK compartment expanded as much as the more proliferative *Nras*$^{G12D}$ (Figure S5A). Both LT-HSCs and ST-HSCs

in *Nras*$^{G12D}$ and *p53*$^{mut}$*; Nras*$^{G12D}$ were increased in spleen compared to control and/or *p53*$^{mut}$ (Figure 2C, D). Importantly, *p53*$^{mut}$ did not further expand the population beyond *Nras*$^{G12D}$. We profiled cell cycle distribution of marrow HSCs (defined by SLAM markers as CD48$^{-}$ CD150$^{+}$ LSK) (Figure S5B). As reported before, *Nras*$^{G12D}$ HSCs were more proliferative than control HSCs. But surprisingly, *p53*$^{mut}$; *Nras*$^{G12D}$ HSCs were as quiescent as control, suggesting that the expansion of these HSCs was through a mechanism distinct from hyperproliferation. As before, both *Nras*$^{G12D}$ and *p53*$^{mut}$*; Nras*$^{G12D}$ had significant expansion of all MPP subsets in bone marrow and/or spleen compared to control (Figure 2E). However, cell cycle analysis did not reveal significant changes in MPPs (defined by SLAM markers as CD48$^{-}$ CD150$^{-}$ LSK) (Figure S5C). Taken together, we show that *p53*$^{mut}$ expands HSPCs in *Nras*$^{G12D}$ mice potentially by regulating mechanisms other than proliferation.

### *p53*$^{mut}$*; Nras*$^{G12D}$ mice have expanded myeloid compartment with hyperactivated ERK1/2 signaling

To investigate how *p53*$^{mut}$ affects the downstream progenitors, we first analyzed myeloid progenitors (MP) defined as Lin$^{-}$ IL7R$\alpha^{-}$ Sca1$^{-}$ c-Kit$^{+}$, and its subsets common myeloid progenitor (CMP), granulocyte-macrophage progenitors (GMP) and megakaryocyte-erythroid progenitor (MEP) compartments (based on the surface expression of CD34 and CD16/32) in control, *p53*$^{mut}$, *Nras*$^{G12D}$, and *p53*$^{mut}$*; Nras*$^{G12D}$ mice (Figure S4A). Compared to control, *p53*$^{mut}$ alone induced a slight MP expansion in bone marrow, though this increase cannot be definitively attributed to significant expansion of any one downstream progenitor (Figure 3A). In the spleen, *p53*$^{mut}$ had significant expansion of CMP and its downstream MEP in comparison to control, though the expansion was insufficient to increase MPs overall. In agreement with our previous results (19, 48), all MP compartments of *Nras*$^{G12D}$ mice, including CMP, GMP and MEP, were significantly expanded in both bone marrow and spleen compared to control. Surprisingly, despite larger spleen size, expression of *p53*$^{mut}$ did not further expand number of MPs in *Nras*$^{G12D}$ spleen.

Rather, it decreased number of MPs in *Nras*$^{G12D}$ bone marrow back to control level. Consistent with our previous report (47), cell cycle analysis of *Nras*$^{G12D}$ MPs showed similar profile as control, suggesting that expanded *Nras*$^{G12D}$ MPs may come from expanded MPPs (Figure 3B). By contrast, the expanded MPP compartments in *p53*$^{mut}$; *Nras*$^{G12D}$ bone marrow yielded expanded CMPs but not GMPs and MEPs, suggesting a differentiation defect from CMP to GMP and MEP in these mice.

In sharp contrast to the moderate phenotypes in *p53*$^{mut}$; *Nras*$^{G12D}$ MPs, flow analysis of phosphorylated signaling proteins showed significant hyperactivation of ERK signaling, the major signaling component downstream of oncogenic *Nras*, in *p53*$^{mut}$; *Nras*$^{G12D}$ Lin$^{-}$ cKit$^{+}$ cells (enriched for MPs) compared to all three groups in the absence of serum and cytokine stimuli (Figure 3C). Upon cytokine stimulation (murine granulocyte-macrophage colony stimulating factor, mGM-CSF), phosphorylated ERK1/2 levels further increased compared to all three groups. In line with the quantitative results from multiparameter flow cytometry, *in vitro* colony assay in a semi-solid methylcellulose medium showed that *p53*$^{mut}$; *Nras*$^{G12D}$ MPs formed significantly higher number of colonies in the presence of murine IL-3 (mIL-3) or mGM-CSF compared to both control but unexpectedly on par with *Nras*$^{G12D}$ MPs (Fig 3D, E). To evaluate replating capability of MPs, the mIL-3 treated cells were re-plated in culture after counting for two additional rounds *in vitro*. *p53*$^{mut}$ MPs were indistinguishable from control cells, while both *Nras*$^{G12D}$ and *p53*$^{mut}$; *Nras*$^{G12D}$ MPs showed significantly higher replating ability compared to control but were comparable to each other (Figure 3E). Interestingly, despite expansion of the lymphoid primed MPP4 cells in *p53*$^{mut}$*; Nras*$^{G12D}$ bone marrow (Figure 2E), downstream common lymphoid progenitor (CLP, defined as Lin$^{-}$ IL7R$\alpha^{+}$ Sca1$^{lo}$ cKit$^{lo}$) numbers were significantly diminished in *p53*$^{mut}$*; Nras*$^{G12D}$ compared to both control and *Nras*$^{G12D}$ (Figure 3F). This may be due to a differentiation defect in *p53*$^{mut}$*; Nras*$^{G12D}$ MPPs. Taken together, our data suggest that *p53*$^{mut}$ does not promote expansion and

replating capability in *Nras*$^{G12D}$ MPs *in vitro* and *in vivo*, in a sharp departure from how loss of *p53* could further enhance these properties in *Nras*$^{G12D}$ MPs.

### *p53*$^{mut}$; *Nras*$^{G12D}$ HSPCs display an MPP gene signature

To investigate how *p53*$^{mut}$ cooperates with oncogenic *Nras* to promote leukemogenesis, we performed bulk RNA-sequencing of sorted Lin$^-$cKit$^+$ bone marrow cells from moribund *p53*$^{mut}$; *Nras*$^{G12D}$ as well as pI-pC treated age-matched control, *p53*$^{mut}$ and *Nras*$^{G12D}$ mice. RNA-seq analysis of *p53*$^{mut}$; *Nras*$^{G12D}$ and control revealed 716 differentially expressed genes (DEGs), with 258 and 458 genes significantly upregulated and downregulated respectively in *p53*$^{mut}$; *Nras*$^{G12D}$ (fold change ≥ 2, false discovery rate (FDR)/ adjusted P value < 0.05) (Figure 4A). We first looked at potential mechanisms underlying hyperactivation of ERK1/2 pathway. Consistent with the genotyping results (Figure S1D), we found that transcripts from both wild-type *Nras* allele and oncogenic *Nras*$^{G12D}$ allele were approximately equally represented and *Nras* itself was not differentially upregulated compared to control (data not shown). Evaluation of known positive or negative regulators of ERK1/2 signaling pathway show moderate upregulation of RAS-GEF *Rasgrp4* and downregulation of RAS-GAP *Dab2ip* in *p53*$^{mut}$; *Nras*$^{G12D}$ transcriptome (Figure S6 A, B). In addition to this, upon further examination of the 258 differentially upregulated genes, we identified increased expression of several receptor tyrosine kinases (RTKs) upstream of ERK1/2 pathway, which can potentially contribute to the basal hyperactivation of the MEK/ERK pathway in MPs (Figure 4B).

To identify the cell type(s) enriched in Lin$^-$cKit$^+$ *p53*$^{mut}$; *Nras*$^{G12D}$ cells, we first aligned LT-HSC and MPP gene signatures previously defined using a published microarray dataset with control and *p53*$^{mut}$; *Nras*$^{G12D}$ transcriptomes (19, 51). We found that *p53*$^{mut}$; *Nras*$^{G12D}$ Lin$^-$cKit$^+$ cells were enriched for MPP gene signature (Figure 4C). This is in stark contrast to the partial HSC gene signature displayed by the leukemia initiating cells of *p53*$^{-/-}$; *Nras*$^{G12D}$ (19). Consistent with

the gene expression heatmap, Gene Set Enrichment Analysis (GSEA) of the MPP gene signature showed that *p53$^{mut}$; Nras$^{G12D}$* was enriched for gene set upregulated in MPP (vs LT-HSC) (NES= 2.95, FDR=0) and conversely, genes downregulated in MPP were enriched in control samples (NES=-2.9, FDR=0) (Figure 4D). Next, we tried to align the *p53$^{mut}$; Nras$^{G12D}$* transcriptome against MEP and GMP gene signatures defined as before using another published microarray dataset (19, 52). In contrast to the distinct MEP gene signature enriched in *p53$^{-/-}$; Nras$^{G12D}$* AML, we found that there is only a partial enrichment of MEP gene signature in *p53$^{mut}$; Nras$^{G12D}$* compared to control (MEP: NES=1.88, FDR=0) (Figure 4D). Surprisingly, we found that GMP gene signature is also enriched in *p53$^{mut}$; Nras$^{G12D}$* (GMP: NES=2.79, FDR=0) (Figure 4D).

To further validate this observation, we transplanted 4000 LSKs or 4000 GMPs or 2000 MEPs isolated from ~7-8 week old *p53$^{mut}$; Nras$^{G12D}$* mice into lethally irradiated syngeneic recipients with 0.25x $10^6$ competitor cells (CD45.1$^+$) and monitored up to 400 days post transplantation. All 4/4 LSK recipients successfully developed AML whereas only 2/4 GMP recipients and 3/5 MEP recipients developed AML. This suggests that while LSKs are fully competent to become leukemia initiating cells (LICs), both MEPs and GMPs are only partially transformed (Table S1). On the whole, *p53* missense mutant altered distinct oncogenic *Nras* cell populations compared to loss of *p53* to promote leukemia.

## *p53$^{mut}$* dysregulates key hematopoietic transcription factor networks and promotes inflammation

Genes differentially expressed between control and *p53$^{mut}$; Nras$^{G12D}$* (AML signature) were hierarchically clustered and a heatmap of the gene expression values in all four groups was obtained. The expression of the AML signature genes in *p53$^{mut}$* and *Nras$^{G12D}$* was largely indistinguishable from that of control, indicating that the transcriptional changes driving leukemogenesis in *p53$^{mut}$; Nras$^{G12D}$* is a product of genetic synergism rather than an additive effect

(Figure 5A). We next performed a systematic and unbiased GSEA analysis comparing *p53$^{mut}$; Nras$^{G12D}$* and control samples against the gene sets available on Molecular Signature Database (MSigDB) (59). Overall, several gene sets related to enhanced inflammation, innate immunity were enriched in *p53$^{mut}$; Nras$^{G12D}$*, while gene sets associated with extra-cellular matrix reorganization were predominantly negatively enriched (Figure 5B). In particular, inflammation associated signaling pathways such as Toll-like-Receptor (TLR) signaling pathway and IL6-JAK-STAT3 signaling were overrepresented in *p53$^{mut}$; Nras$^{G12D}$* (Figure 5C). Gene transcripts of several key regulatory components of both pathways such as *Nfkbia*, *Csf1r*, *Tlr12*, *Tlr13, Il6ra* were significantly upregulated in *p53$^{mut}$; Nras$^{G12D}$* transcriptome (Figure 4B, 5D), some of which were further validated by q-PCR (Figure 5E).

Activation of TLR pathway(s) by various stimuli including molecular patterns found in pathogens can trigger a cascade of signaling pathways resulting in production of several inflammatory cytokines (64, 65). We measured the levels of secreted inflammatory cytokines in the serum of ~8 week old primary *p53$^{mut}$; Nras$^{G12D}$* mice or recipients of *p53$^{mut}$; Nras$^{G12D}$* WBM (8 weeks after transplantation). We used a multiplex sandwich immunoassay where a plate pre-coated with capture antibodies against a panel of 10 proinflammatory cytokines was used to detect and quantitate all 10 cytokines simultaneously in the serum pre-incubated with detection antibodies conjugated to electrochemiluminescent labels. We found elevated levels of several inflammatory cytokines such as IL-6, TNF-α and IL-2 (Figure S7). Thus, *p53* missense mutant sustains a distinctly pro-inflammatory environment with upregulated TLR pathway signaling in oncogenic *Nras* mice.

We noticed that the predominant inflammatory gene signature seen in *p53$^{mut}$* AML was absent in *p53$^{-/-}$* AML suggesting distinct molecular mechanisms driving leukemogenesis. To delineate these unique mechanisms, we first compared *p53$^{mut}$* and loss of *p53* driven *Nras$^{G12D}$*-AML transcriptomes. In comparison to the massive number of genes differentially regulated by

*p53*$^{-/-}$*; Nras*$^{G12D}$ to promote AML (2,453 upregulated and 3,604 downregulated, fold change>2 and FDR<0.05), *p53*$^{mut}$ differentially regulated only 716 genes in synergy with *Nras*$^{G12D}$ ((19), Figure 4A). We compared these DEGs from both *p53* loss driven and *p53*$^{mut}$ driven *Nras*$^{G12D}$ AML transcriptomes to identify common genes (Figure 6A). Despite the wide-range of genes regulated by *p53*$^{-/-}$*; Nras*$^{G12D}$, only a small subset of genes overlapped with *p53*$^{mut}$*; Nras*$^{G12D}$ AML gene signature, suggesting distinct molecular mechanisms. Common upregulated genes between both AML transcriptomes were enriched for RAS pathway related molecular signatures that include classic oncogenic RAS activated transcription factors (TFs) such as *Junb*, whereas common downregulated genes were enriched for NPM1 mutated or MLL1 driven AML related gene sets (data not shown). These results show that *p53*$^{mut}$ indeed drives AML via distinct mechanisms compared to *p53*$^{-/-}$ in oncogenic *Nras* background.

To understand how these DEGs were transcriptionally regulated, we used Metascape, an online tool that integrates information from several databases (e.g., TRRUST) to identify key transcription factor regulatory networks enriched in DEGs based on curated literature (54, 55) (Figure 6B). In *p53*$^{-/-}$; *Nras*$^{G12D}$ AML, NF-κB pathway TF (*Rela* and *Nfkb1*) networks were enriched in downregulated genes, suggesting that NF-κB pathway target genes are predominantly downregulated. By contrast, in *p53*$^{mut}$*; Nras*$^{G12D}$ driven AML, both *Rela* and *Nfkb1* networks were enriched in upregulated genes. This is consistent with the upregulation of TLR signaling pathway which culminates in the activation of NF-κB to promote inflammatory cytokine gene expression.

In addition, both *Gata1* and *Gata2* TF networks were uniquely downregulated only in *p53*$^{mut}$*; Nras*$^{G12D}$ AML, suggesting potential loss of *Gata* TF activity. Consistent with this, we found that both *Gata1* and *Gata2* TFs were differentially downregulated in *p53*$^{mut}$; *Nras*$^{G12D}$ AML (Figure 6C). Comparing the loss of *Gata2* enhancer transcriptome (-77$^{-/-}$ CMP) with *p53*$^{mut}$*; Nras*$^{G12D}$, we found that genes downregulated upon *Gata2* loss were enriched in control compared to *p53*$^{mut}$*; Nras*$^{G12D}$, thus suggesting that *p53*$^{mut}$*; Nras*$^{G12D}$ AML transcriptome mimics loss of *Gata2* (57)

(Figure 6D). Indeed, we found that several *Gata2* target genes essential for erythroid differentiation were also downregulated in *p53$^{mut}$; Nras$^{G12D}$* (Figure S8) (56).

In addition to *Gata* TF family, *Runx1* TF network was also found to be differentially regulated in *p53$^{mut}$; Nras$^{G12D}$* AML, with potential *Runx1* target genes present in both upregulated and downregulated genes (Figure 6B). Concordantly, GSEA results showed that genes upregulated in *Runx1* KO LSK cells were partially enriched in *p53$^{mut}$; Nras$^{G12D}$* AML and conversely, genes downregulated in *Runx1* KO cells were enriched in control (Figure 6E) (58). As *Runx1* is not differentially expressed, this suggests downregulation of its network potential through post-transcriptional mechanisms in *p53$^{mut}$; Nras$^{G12D}$* driven AML. Taken together, our results show that *p53$^{mut}$* synergizes with oncogenic *Nras* to disrupt key hematopoietic transcription factor networks and promote AML.

### 3.5 Discussion

Missense mutations in the tumor suppressor gene *p53* and RAS pathway mutations concurrently occur in a subset of AML patients, whose survival is much shorter than patients with mutations in either of the pathways. We have shown in the past that loss of *p53* can cooperate with oncogenic *Nras*, but extrapolation of this observation to hotspot *p53* missense mutations warrants further investigation due to the gain-of-function nature of these mutations. In this study, we show that p53 missense mutant (*p53$^{R172H/+}$*) synergizes with oncogenic Nras signaling to induce a highly penetrant AML (Figure S9). Although expression of *p53* missense mutant in *Nras$^{G12D/+}$* cells did not further expand bone marrow HSPCs, it hyperactivated ERK1/2 signaling beyond *Nras$^{G12D/+}$* levels. Mutant *p53* transformed cells are enriched for MPP gene signature, and both MEPs and GMPs are partially transformed to initiate leukemia. Although our study does not specifically address whether the *p53* missense mutant herein is gain-of-function, it definitely calls attention to distinct mechanisms of cooperation by *p53* missense mutant and loss of *p53* with concurrent genetic mutations such as oncogenic *Nras*.

We identified some key differences in how *p53* missense mutant cooperates with oncogenic *Nras* versus loss of *p53* to promote AML (19). First, while a fraction $p53^{-/-}$; $Nras^{G12D}$ or its whole bone marrow (WBM) recipients developed T-ALL, none of $p53^{mut}$; $Nras^{G12D}$ or its WBM recipients had any instance of T-ALL and only developed a highly penetrant AML (Figure 1). In fact, almost none of the $p53^{mut}$; $Nras^{G12D}$ AML mice had an observable thymus organ at moribundity (Figure 1E).

Second, loss of *p53* further expanded $Nras^{G12D}$ MPs, increased their replating ability and quiescence of both $Nras^{G12D}$ MPs and MEPs. $p53^{-/-}$; $Nras^{G12D}$ MEPs are transformed to leukemia initiating cells (LICs) and display a partial HSC gene signature. In contrast, $p53^{mut}$ does not further expand $Nras^{G12D}$ progenitor cells or increase their replating capability or proliferation (Figure 3 A-E). $p53^{mut}$; $Nras^{G12D}$ MEPs and GMPs are partially transformed, while HSPCs display a strong MPP gene signature (Figure 4, Table S1). $p53^{mut}$ fully transformed LSKs as LICs. Despite loss of *p53* increasing self-renewal of AML cells, we did not see loss of wild-type *p53* allele in $p53^{mut}$ AML, perhaps due to rapid lethality in our model (Figure S1D).

Though both loss of *p53* and *p53* missense mutant hyperactivated ERK-1/2 signaling in myeloid progenitors, the underlying mechanisms are distinct. The MEK/ERK hyperactivation in oncogenic *Nras* cells transformed by loss of *p53* is primarily due to selection of homozygosity of oncogenic *Nras* allele and overexpression of oncogenic *Nras* itself. In contrast, both genotyping and RNA-seq results of $p53^{mut}$; $Nras^{G12D}$ AML show no selection of loss of *Nras wt* allele loss or *Nras* overexpression. We believe the hyperactivated ERK signaling is predominantly due to aberrant upregulation of upstream receptor tyrosine kinases (RTKs) (65-68) (Figure 4B). However, it is surprising that despite the manifold hyperactivation of ERK1/2 signaling in $p53^{mut}$; $Nras^{G12D}$ progenitors, it does not result in hyperproliferation. Consistent with this observation, we did not find cell cycle related gene sets to be enriched in $p53^{mut}$; $Nras^{G12D}$ AML.

At molecular level, bulk RNA-sequencing revealed a much smaller network of 716 genes associated with AML in *p53*$^{mut}$*; Nras*$^{G12D}$ compared to the massive (6,057 genes) *p53*$^{-/-}$*; Nras*$^{G12D}$ AML transcriptome (Figure 4A). Despite the size of *p53*$^{-/-}$*; Nras*$^{G12D}$ AML DEGs, there was minimal overlap with *p53*$^{mut}$*; Nras*$^{G12D}$ AML DEGs, indicating distinct molecular mechanisms. In particular, NF-κB pathway genes are downregulated in *p53*$^{-/-}$*; Nras*$^{G12D}$ AML, whereas, NF-κB pathway driven inflammatory pathway and genes therein are upregulated in *p53*$^{mut}$*; Nras*$^{G12D}$ AML. Thus, our results show that in the context of oncogenic *Nras*, mutant p53 can promote leukemogenesis in distinct manner compared to loss of *p53*, in line with recent reports (46)

A prominent phenotype displayed by the *p53*$^{mut}$*; Nras*$^{G12D}$ mice is the severe inflammatory environment potentially driven by aberrant Toll-like Receptor signaling. This was evidenced early on by their inability to survive pI-pC injections to induce Cre expression (Figure S1B). Administration of pI-pC stimulates TLR3 pathway resulting in production of type I interferon and other inflammatory cytokines (71). Consistent with this observation, our whole transcriptome analysis revealed over-representation of inflammatory pathways such as TLR signaling, IL-6/JAK-STAT (Figure 5B). In congruence with the ability of mutant *p53* to aberrantly regulate transcription factor activity to promote leukemogenesis (46), we found that prominent hematopoietic transcriptions such as *Gata2* and *Runx1* networks are predominantly downregulated in *p53*$^{mut}$ driven AML in the background of oncogenic *Nras* (Figure 6). A recent study of loss of *Gata2* enhancer (-77kb upstream of *Gata2* transcription start site (-77$^{-/-}$)) in hematopoietic system showed that *Gata2* loss in MPs resulted in downregulation of *Gata1*, upregulation of several TLR pathway receptors and consequently, enrichment of a spectrum of inflammatory mechanisms (66). In addition, loss of *Runx1* in the hematopoietic system results in increased inflammatory cytokine production by neutrophils as a consequence of aberrant response to TLR4 signaling (60). In response to lipopolysaccharide (LPS), a TLR4 agonist, several inflammatory cytokines including TNF, IL-6 were highly elevated in the bronchoalveolar lavage (BAL) of *Runx1* KO mice

compared to control. This was in part due to upregulation of several TLR4 pathway components in *Runx1* KO neutrophils, resulting in over-response to TLR4 stimulation. Taken together, our results support the idea that $p53^{mut}$ uniquely synergizes with oncogenic *Nras* by potentially dysregulating key hematopoietic transcription factor networks and promotes an inflammatory microenvironment (Figure S9). Although the precise mechanism of regulation of these transcription factors is yet to be determined in our model, future work may shed some light in this regard.

### 3.6 Figures and Legends

**Figure 3-1: p53 missense mutant cooperates with oncogenic NrasG12D to induce a highly penetrant AML**

(A-F) 6-8 week old control (con), *p53*$^{mut}$, *Nras*$^{G12D}$ mice were treated with pI-pC as described in "Materials and methods" section and monitored along with untreated *p53*$^{mut}$; *Nras*$^{G12D}$. (A) Kaplan-Meier comparative survival analysis of pI-pC treated and untreated experimental mice. Percent survival was plotted against number of days since birth. *P* value was determined by log-rank test. (B) Quantification of myeloid and lymphoid cells as % of total live cells in bone marrow (BM), spleen (SP) and peripheral blood (PB) of moribund AML *p53*$^{mut}$*; Nras*$^{G12D}$ and age-matched control. Note: red blood cells were lysed using RBC lysis buffer prior to flow analysis. (C) Complete blood count was performed on peripheral blood samples collected from moribund AML *p53*$^{mut}$*; Nras*$^{G12D}$ and age-matched control mice. (D) Spleen and thymus weight of moribund AML *p53*$^{mut}$*; Nras*$^{G12D}$ and age-matched control. (E) Representative spleen histologic hematoxylin and eosin-stained sections from moribund AML *p53*$^{mut}$*; Nras*$^{G12D}$ and age-matched control mice. (F) 1X10$^{6}$ bone marrow cells from moribund primary AML *p53*$^{mut}$*; Nras*$^{G12D}$ mice or age-matched control were transplanted into lethally irradiated syngeneic recipients along with equal number of helper CD45.1$^{+}$ cells. Kaplan-Meier comparative survival curve was plotted against days post transplantation. All bar graphs and scatter plots are presented as mean ± standard deviation (SD). * *P*< 0.05, ***P*< 0.01, ****P*< 0.001. AML, acute myeloid leukemia; BMT, bone marrow transplantation.

Figure 1

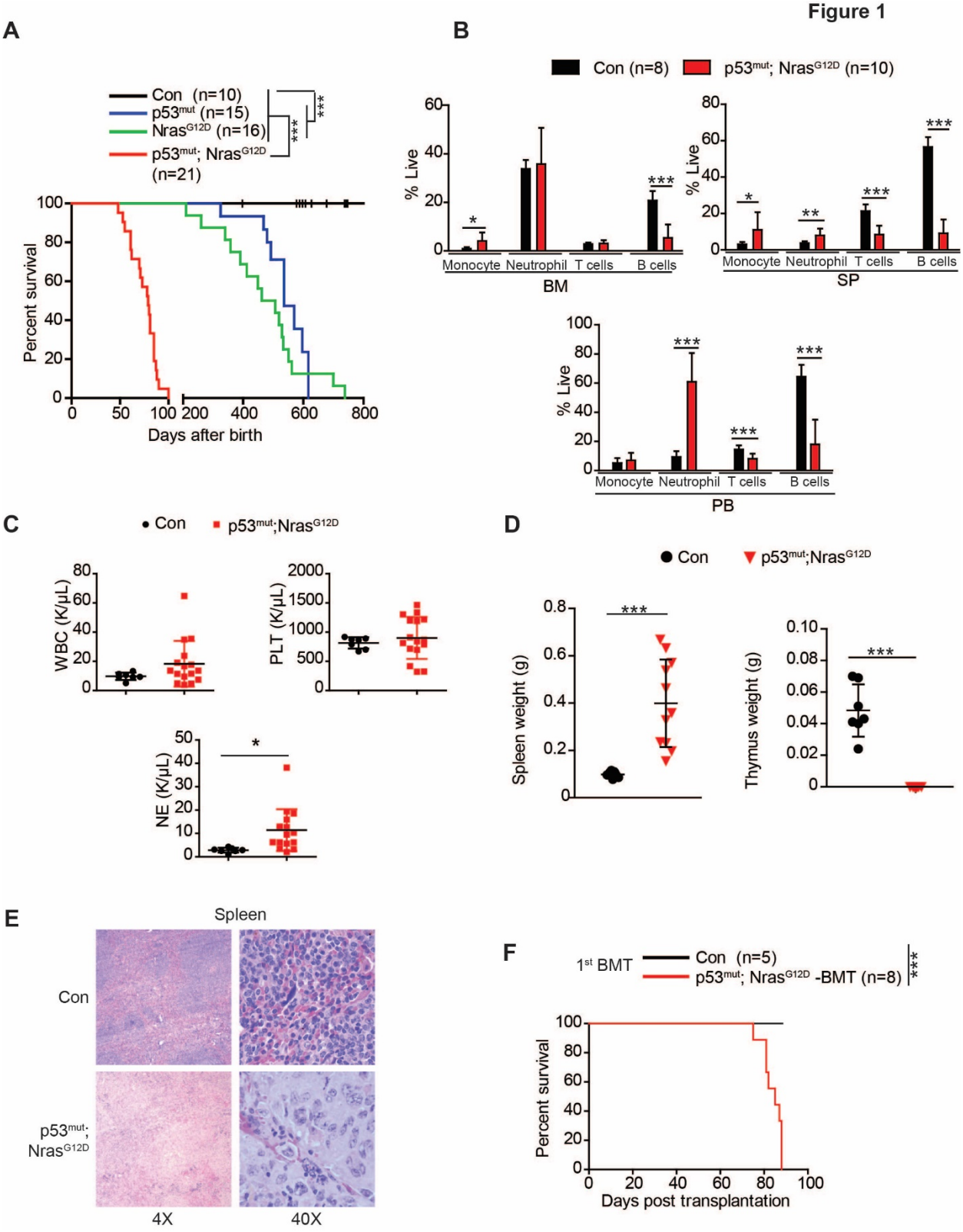
A
Con (n=10)
p53mut (n=15)
NrasG12D (n=16)
p53mut; NrasG12D (n=21)
***
***
Percent survival
Days after birth
B
Con (n=8)
p53mut; NrasG12D (n=10)
% Live
Monocyte
Neutrophil
T cells
B cells
BM
SP
PB
C
Con
p53mut;NrasG12D
WBC (K/μL)
PLT (K/μL)
NE (K/μL)
D
Spleen weight (g)
Thymus weight (g)
E
Spleen
Con
p53mut; NrasG12D
4X
40X
F
1st BMT
Con (n=5)
p53mut; NrasG12D -BMT (n=8)
Percent survival
Days post transplantation

**Figure 3-2: *p53*$^{mut}$ leads to expansion of multipotent progenitor cells in *Nras*$^{G12D}$ mice**

(B-E) Control, *p53*$^{mut}$, *Nras*$^{G12D}$ were treated with pI-pC and euthanized on day 12 along with untreated *p53*$^{mut}$*; Nras*$^{G12D}$ mice for downstream analysis as described in "Materials and methods" section. (A) Schematic representation of hematopoiesis at steady state (B-E) Quantification of absolute numbers of (B) LSKs (Lin$^-$ Sca1$^+$ cKit$^+$) (C) LT-HSC (Flk2$^-$ CD48$^-$ CD150$^+$ LSK) (D) ST-HSC (Flk2$^-$ CD48$^-$ D150$^-$ LSK) (E) MPP-2 (Flk2$^-$ CD150$^+$ CD48$^+$ LSK), MPP-3 (Flk2$^-$ CD150$^-$ CD48$^+$ LSK) and MPP-4 (Flk2$^+$ CD150$^-$ CD48$^{+/-}$ LSK) in bone marrow (BM) and spleen (SP) based on bone marrow or spleen cell numbers and frequencies of cell populations of total live cells. Absolute numbers of cell populations in BM were calculated for 6 bones (4 hind limb + 2 front limbs). Data is presented as mean ± standard deviation (SD). * $P< 0.05$, ** $P< 0.01$, *** $P< 0.001$.

Figure 2

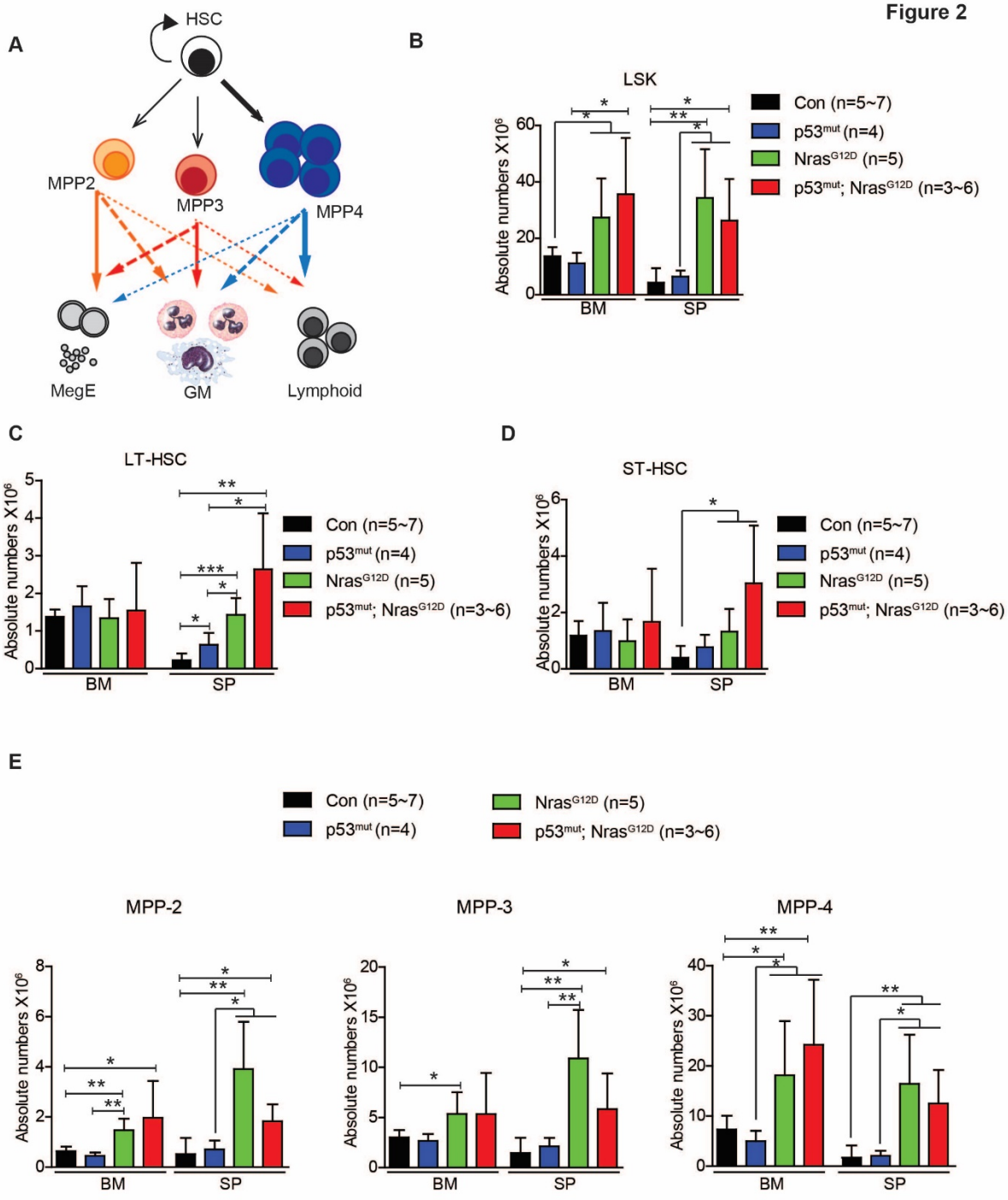
A
HSC
MPP2
MPP3
MPP4
MegE
GM
Lymphoid
B
LSK
Absolute numbers X10⁶
Con (n=5~7)
p53mut (n=4)
NrasG12D (n=5)
p53mut; NrasG12D (n=3~6)
BM
SP
C
LT-HSC
D
ST-HSC
E
MPP-2
MPP-3
MPP-4

**Figure 3-3: *p53$^{mut}$; Nras$^{G12D}$* mice have expanded myeloid compartment with hyperactivated ERK1/2 signaling**

(A-F) Control, *p53$^{mut}$*, *Nras$^{G12D}$* were treated with pI-pC and euthanized on day 12 along with untreated *p53$^{mut}$; Nras$^{G12D}$* mice for downstream analysis as described in "Materials and methods" section. (A) Quantification of absolute numbers of myeloid progenitors (MP), common myeloid progenitors (CMP), granulocyte-macrophage progenitors (GMP) and megakaryocyte-erythroid progenitors (MEP) in BM and SP based on bone marrow or spleen cell numbers and frequencies of cell populations of total live cells. Absolute numbers of cell populations in BM were calculated for 6 bones (4 hind limb + 2 front limbs). (B) Cell cycle analysis of bone marrow MPs using Ki-67/ 4',6-diamidino-2-phenylindole (DAPI) staining. (C) Whole bone marrow cells isolated from all four groups were serum and cytokine starved for 2 hours and stimulated with various concentrations of murine GM-CSF (0, 0.16 and 2 ng/mL) at 37$^{o}$C for 10 minutes. Levels of phosphorylated ERK1/2 (p-ERK1/2) were measured using phosphor-specific flow cytometry. Lin$^{-}$cKit$^{+}$ bone marrow cells enriched for myeloid progenitors were gated for data analysis. To quantify activation of ERK1/2, median intensities of p-ERK1/2 at different GM-CSF concentrations are compared with their respective control cells at 0 ng/mL, which is arbitrarily set at 1. (D, E) 5 X $10^4$ bone marrow cells isolated from all four groups were plated in semisolid methylcellulose medium with either 0.2 ng/mL murine GM-CSF (D) or 10 ng/mL murine IL-3 (E). Colonies were counted 7-9 days after culture. Methylcellulose culture of 5 X $10^4$ bone marrow cells over 2 (D) or 3 (E) rounds of re-plating. (F) Quantification of absolute numbers of common lymphoid progenitors (CLPs) (Lin$^{-}$ / IL7R$\alpha^{+}$/ Sca1$^{lo}$/ cKit$^{lo}$) in bone marrow (BM) and spleen (SP) based on bone marrow or spleen cell numbers and frequencies of CLPs of total live cells. Absolute numbers of cell populations in BM were calculated for 6 bones (4 hind limb + 2 front limbs). Data is presented as mean ± standard deviation (SD). * $P< 0.05$, ** $P< 0.01$, *** $P< 0.001$.

Figure 3

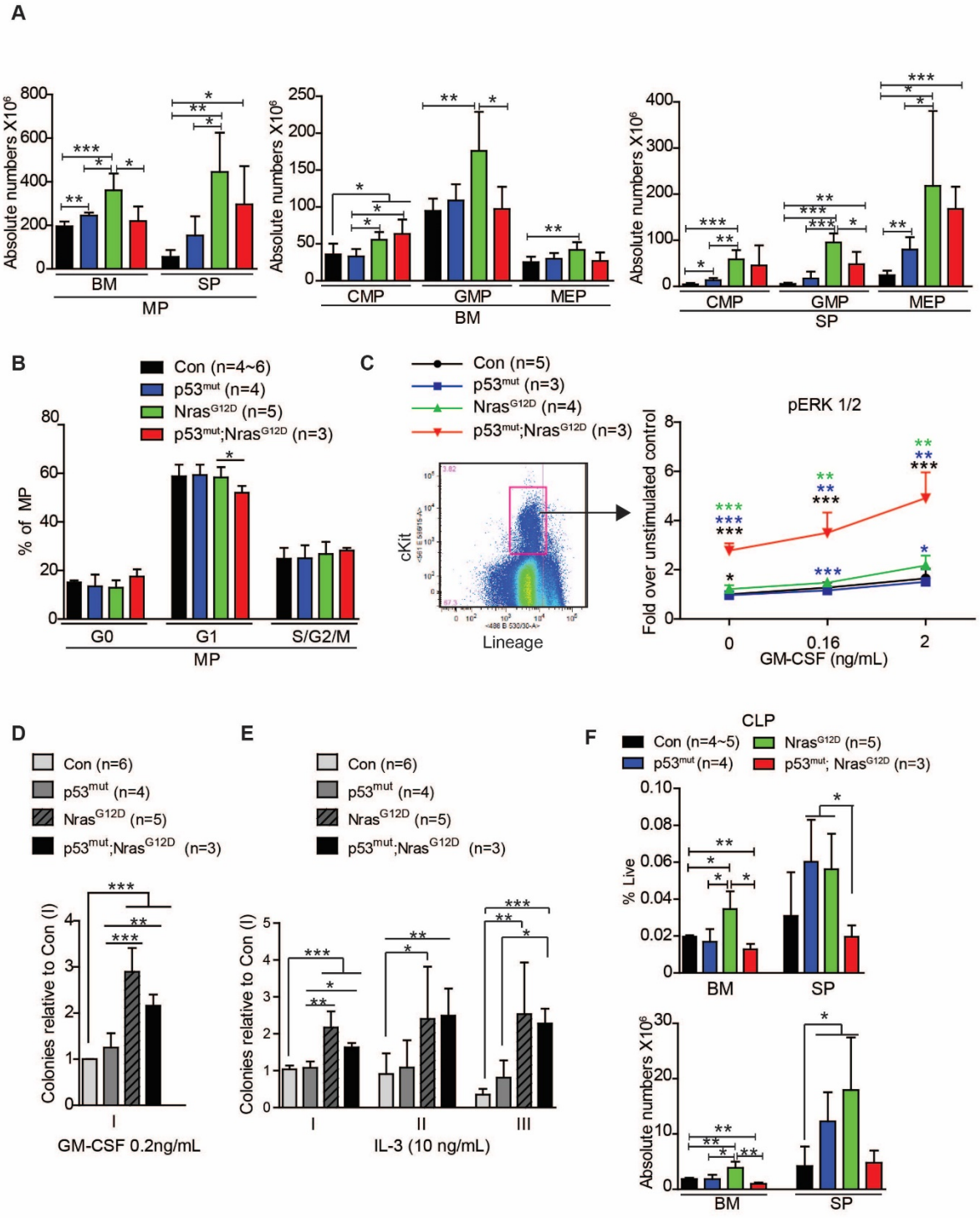
A
Absolute numbers X10^6
BM
SP
MP
CMP
GMP
MEP
BM
SP
B
Con (n=4~6)
p53mut (n=4)
NrasG12D (n=5)
p53mut;NrasG12D (n=3)
% of MP
G0
G1
S/G2/M
MP
C
Con (n=5)
p53mut (n=3)
NrasG12D (n=4)
p53mut;NrasG12D (n=3)
cKit
Lineage
pERK 1/2
Fold over unstimulated control
GM-CSF (ng/mL)
D
Con (n=6)
p53mut (n=4)
NrasG12D (n=5)
p53mut;NrasG12D (n=3)
Colonies relative to Con (I)
GM-CSF 0.2ng/mL
E
IL-3 (10 ng/mL)
F
CLP
Con (n=4~5)
p53mut (n=4)
NrasG12D (n=5)
p53mut; NrasG12D (n=3)
% Live
Absolute numbers X10^6

**Figure 3-4: *p53*$^{mut}$; *Nras*$^{G12D}$ HSPCs display an MPP gene signature**

(A-E) Bulk transcriptome analysis was performed using 50,000 sorted Lin$^-$ cKit$^+$ cells sorted from moribund AML *p53*$^{mut}$*; Nras*$^{G12D}$ (n=4) and pI-pC treated age-matched control (n=3) bone marrow. (A) Volcano plot of differentially expressed genes in *p53*$^{mut}$*; Nras*$^{G12D}$ compared to control, plotted as log 2 fold change ($Log_2FC$) versus -log 10 adjusted P value (FDR). Differentially expressed genes are defined as $Log_2FC > 1$ and FDR <0.05, yielding 258 upregulated and 458 downregulated genes. (B) RPKM values of receptor tyrosine kinases from RNA-seq analysis. *P* values were calculated using R Limma package statistics for differential expression analysis (C) Heatmap depicting relative gene expression profiles of MPP signature genes (genes DE in MPP vs long-term HSCs (LT-HSCs) previously defined in (19) in control and *p53*$^{mut}$*; Nras*$^{G12D}$ samples (D, E) Gene Set Enrichment Analysis (GSEA) was performed between *p53*$^{mut}$*; Nras*$^{G12D}$ versus control samples against (D) MPP or (E) MEP and GMP gene signatures previously defined in (19). Normalized Enrichment Score (NES) and False Discovery Rate (FDR) are shown on each GSEA plot.

Figure 4

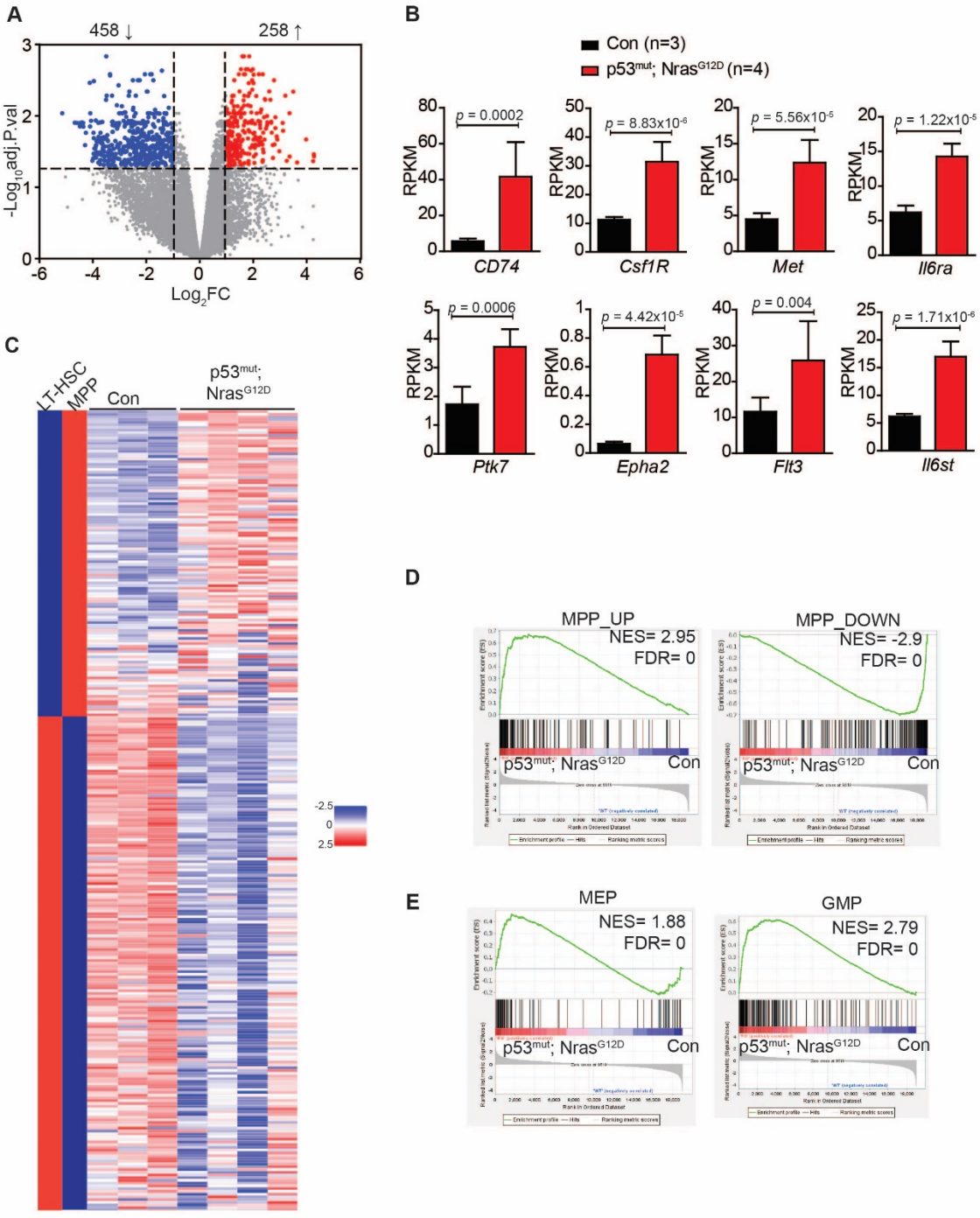
A
458 ↓
258 ↑
-Log10adj.P.val
Log2FC
B
Con (n=3)
p53mut; NrasG12D (n=4)
p = 0.0002
p = 8.83x10-6
p = 5.56x10-5
p = 1.22x10-5
RPKM
CD74
Csf1R
Met
Il6ra
p = 0.0006
p = 4.42x10-5
p = 0.004
p = 1.71x10-6
Ptk7
Epha2
Flt3
Il6st
C
LT-HSC
MPP
Con
p53mut; NrasG12D
-2.5
0
2.5
D
MPP_UP
NES= 2.95
FDR= 0
MPP_DOWN
NES= -2.9
FDR= 0
p53mut; NrasG12D
Con
E
MEP
NES= 1.88
FDR= 0
GMP
NES= 2.79
FDR= 0

**Figure 3-5: *p53$^{mut}$* promotes a distinct inflammatory environment in oncogenic *Nras$^{G12D}$* mice**

(A-D) Bulk transcriptome analysis was performed using 50,000 sorted Lin$^-$ cKit$^+$ cells sorted from moribund AML *p53$^{mut}$; Nras$^{G12D}$* (n=4) and pI-pC treated age-matched control (n=3), *p53$^{mut}$* (n=3), and *Nras$^{G12D}$* bone marrow. (A) Heatmap depicting gene expression values of 716 differentially expressed genes (DEG) between *p53$^{mut}$; Nras$^{G12D}$* versus control in all four sample groups. Genes are hierarchically clustered and their Z-score ($\log_2$ (FPKM +0.5)) is plotted. FPKM, Fragments per kilobase per million mapped reads. (B, C) Unbiased Gene Set Enrichment Analysis (GSEA) was performed between *p53$^{mut}$; Nras$^{G12D}$* versus control samples against various datasets from Molecular Signatures Database (MSigDB). (B) Top positive and negative enriched gene signatures in *p53$^{mut}$; Nras$^{G12D}$* versus control transcriptome are depicted as a plot of Normalized Enrichment Score (NES) vs False Discovery Rate (FDR). Similar pathways are grouped under the same category relevant to current study and highlighted on the graph with corresponding colored dot. (C) Relevant GSEA plots for various pathways under “inflammation” are depicted. Normalized Enrichment Score (NES) and False Discovery Rate (FDR) are shown on each GSEA plot. (D) Volcano plot depicting key genes belonging to various inflammation- related pathways superimposed on differentially upregulated genes between *p53$^{mut}$; Nras$^{G12D}$* versus control samples. (E) Validation of a subset of differentially expressed genes in AML *p53$^{mut}$; Nras$^{G12D}$* vs control samples using quantitative reverse transcriptase polymerase chain reaction (qRT-PCR). Total RNA was extracted from sorted control and AML Lin$^-$ cKit$^+$ cells, complementary DNAs (cDNAs) were synthesized using iScript cDNA Synthesis Kit (Bio-Rad). qRT-PCR was performed by using iTaq Universal SYBR® Green Supermix with published primers pairs on a CFX96 Real-Time System (Bio-Rad) according to the manufacturer’s instructions. Quantification results of 6 upregulated genes in *p53$^{mut}$; Nras$^{G12D}$* vs control samples are shown here. Data is presented as

mean ± standard deviation (SD). * *P*< 0.05, ***P*< 0.01, ****P*< 0.001. N values indicate biological replicates.

**Figure 5**

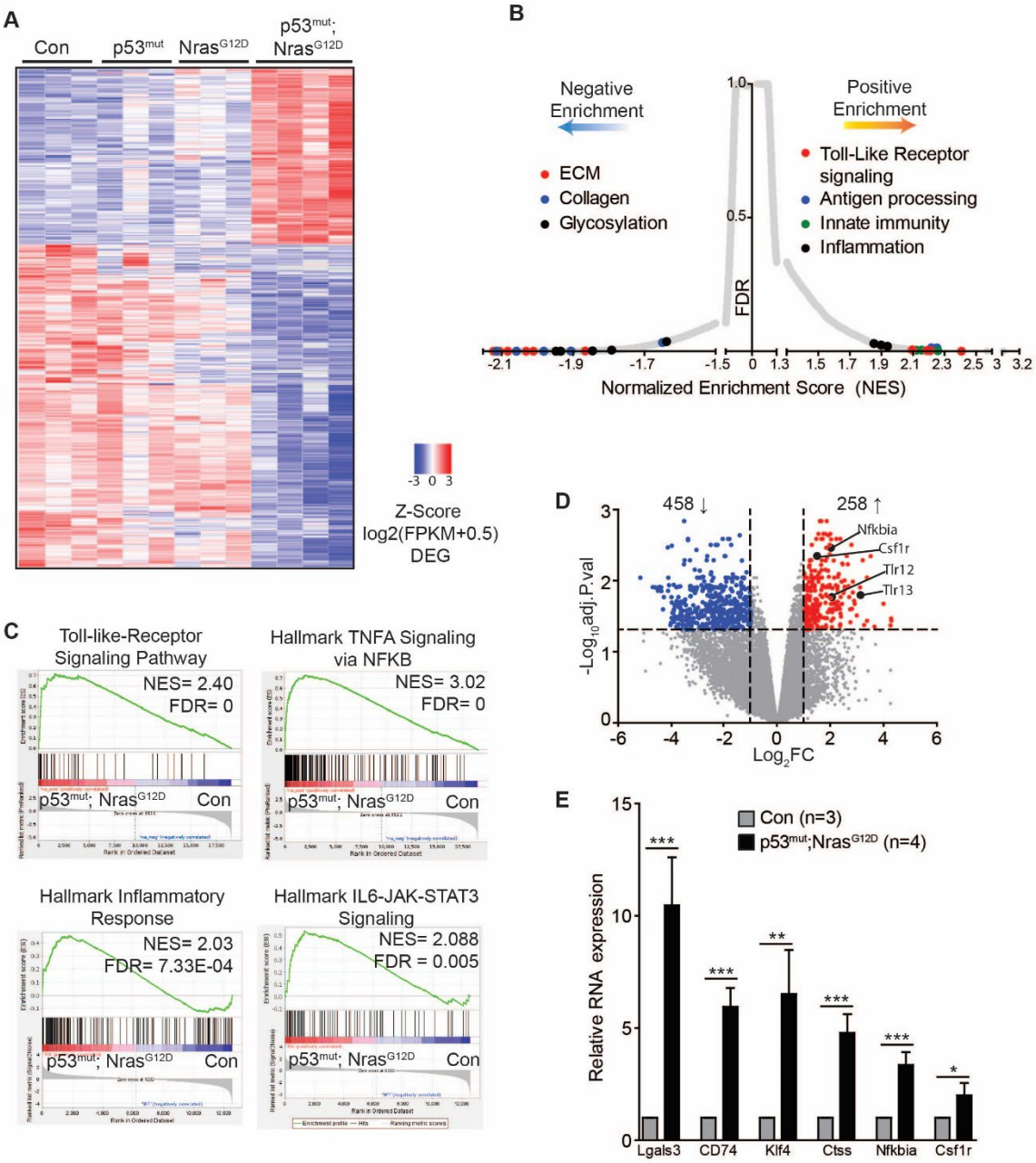

**Figure 3-6: *p53$^{mut}$* dysregulates key hematopoietic transcription factor networks**

(A-E) Bulk transcriptome analysis was performed using 50,000 sorted Lin$^-$ cKit$^+$ cells sorted from moribund AML *p53$^{mut}$; Nras$^{G12D}$* (n=4) and pI-pC treated age-matched control (n=3) bone marrow. (A) Venn diagram illustrating the overlap among differentially upregulated (or downregulated) genes in AML *p53$^{mut}$; Nras$^{G12D}$* and AML *p53$^{-/-}$; Nras$^{G12D}$* (19). (B) Transcription Factor Enrichment analysis results from Metascape depicting different transcription factors (TF) enriched in up (or down) regulated genes in AML *p53$^{mut}$; Nras$^{G12D}$* and AML *p53$^{-/-}$; Nras$^{G12D}$* along with -log10 P value. Red horizontal bars indicate -$\log_{10}$(P) of TF enriched in upregulated genes, blue horizontal bars indicate -$\log_{10}$(P) of TF enriched in downregulated genes. TF of interest to current study indicated in red. (C) RPKM values of *Gata1* and *Gata2* from RNA-seq analysis. *P* values were calculated using R Limma package statistics for differential expression analysis (D, E) Gene Set Enrichment Analysis (GSEA) was performed between *p53$^{mut}$; Nras$^{G12D}$* versus control samples against (D) genes downregulated in -77$^{-/-}$ CMPs (57), (E) genes up or downregulated in *Runx1* knockout Lin$^-$ Sca1$^+$ cKit$^+$ (LSK) cells (58). Normalized Enrichment Score (NES) and False Discovery Rate (FDR) are shown on each GSEA plot.

**Figure 6**

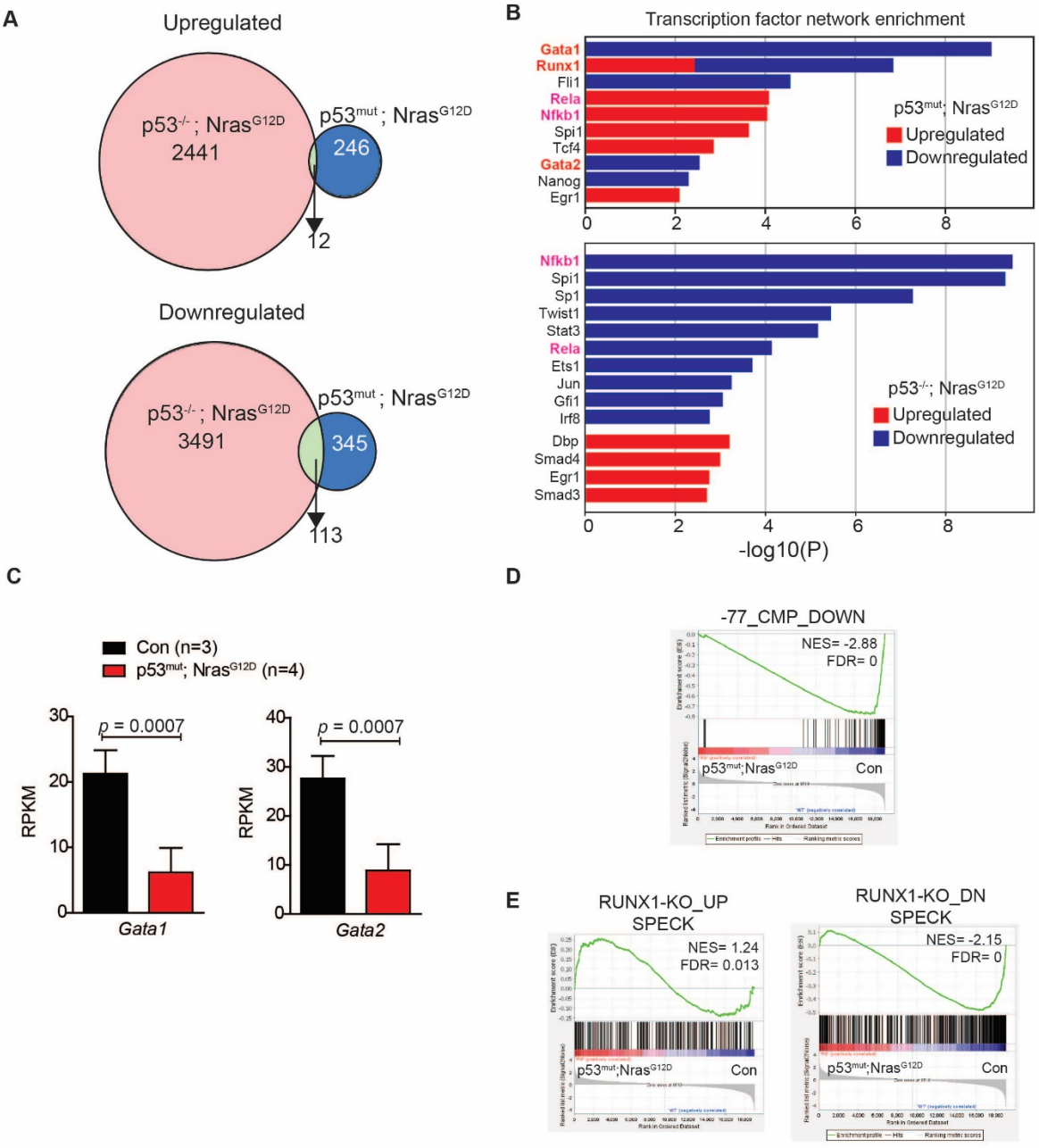
A
Upregulated
p53-/- ; NrasG12D
2441
p53mut ; NrasG12D
246
12
Downregulated
p53-/- ; NrasG12D
3491
p53mut ; NrasG12D
345
113
B
Transcription factor network enrichment
Gata1
Runx1
Fli1
Rela
Nfkb1
Spi1
Tcf4
Gata2
Nanog
Egr1
p53mut; NrasG12D
Upregulated
Downregulated
Nfkb1
Spi1
Sp1
Twist1
Stat3
Rela
Ets1
Jun
Gfi1
Irf8
Dbp
Smad4
Egr1
Smad3
p53-/-; NrasG12D
Upregulated
Downregulated
-log10(P)
C
Con (n=3)
p53mut; NrasG12D (n=4)
RPKM
p = 0.0007
Gata1
Gata2
D
-77_CMP_DOWN
NES= -2.88
FDR= 0
p53mut;NrasG12D
Con
E
RUNX1-KO_UP
SPECK
NES= 1.24
FDR= 0.013
RUNX1-KO_DN
SPECK
NES= -2.15
FDR= 0

**Figure 3-S1: Generation and characterization of experimental animals**

(A) Schematic of breeding strategy used to generate experimental mice used in this study. Acronyms used for pI-pC treated or untreated experimental mice are highlighted in different colors. (B) Kaplan-Meier survival curve of pI-pC treated *p53$^{mut}$; Nras$^{G12D}$* mice. Percent survival was plotted against number of days since birth. (C, D) Genotyping analysis to evaluate recombination efficiency of *Nras$^{G12D}$* and *p53$^{mut}$* alleles in whole bone marrow cells in (C) pI-pC treated *p53$^{mut}$; Nras$^{G12D}$* mice or (D) without pI-pC treatment in moribund *p53$^{mut}$; Nras$^{G12D}$* and age-matched *p53$^{mut}$*, *Nras$^{G12D}$* and control mice. Appropriate tail DNA was used as negative control.

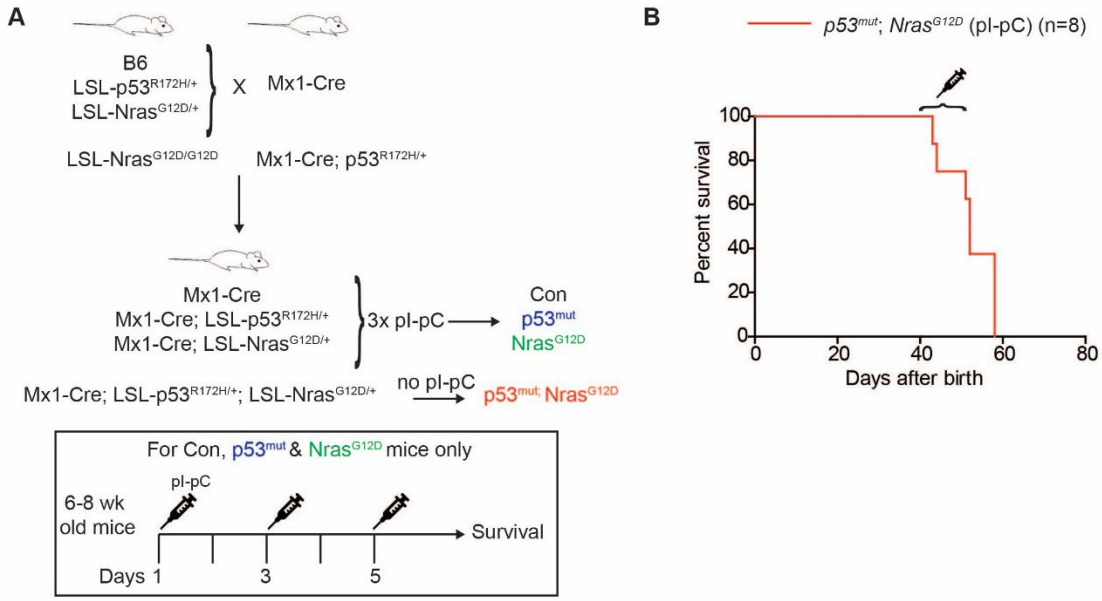
A
B6
LSL-p53R172H/+
LSL-NrasG12D/+
X
Mx1-Cre
LSL-NrasG12D/G12D
Mx1-Cre; p53R172H/+
Mx1-Cre
Mx1-Cre; LSL-p53R172H/+
Mx1-Cre; LSL-NrasG12D/+
3x pI-pC
Con
p53mut
NrasG12D
Mx1-Cre; LSL-p53R172H/+; LSL-NrasG12D/+
no pI-pC
p53mut; NrasG12D
For Con, p53mut & NrasG12D mice only
pI-pC
6-8 wk
old mice
Survival
Days 1
3
5
B
p53mut; NrasG12D (pI-pC) (n=8)
Percent survival
Days after birth
0
20
40
60
80
100

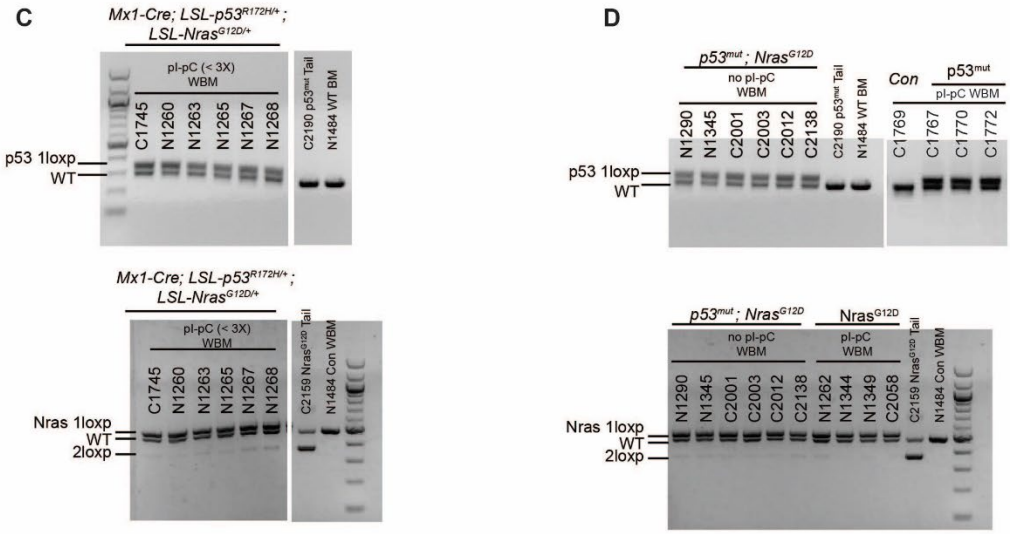
C
Mx1-Cre; LSL-p53R172H/+; LSL-NrasG12D/+
pI-pC (< 3X) WBM
C1745
N1260
N1263
N1265
N1267
N1268
C2190 p53mut Tail
N1484 WT BM
p53 1loxp
WT
Nras 1loxp
2loxp
C2159 NrasG12D Tail
N1484 Con WBM
D
p53mut; NrasG12D
no pI-pC WBM
N1290
N1345
C2001
C2003
C2012
C2138
Con
p53mut
pI-pC WBM
C1769
C1767
C1770
C1772
NrasG12D
pI-pC WBM
N1262
N1344
N1349
C2058

**Figure 3-S2: Myeloid cell infiltration of liver in moribund *p53$^{mut}$; Nras$^{G12D}$* AML mice**

(A) Representative image of moribund *p53$^{mut}$; Nras$^{G12D}$* liver infiltrated with myeloid cells (white) compared with age-matched control liver. (B) Liver/body weight of moribund *p53$^{mut}$; Nras$^{G12D}$* mice and age-matched pI-pC treated control. Data is presented as mean ± standard deviation (SD). **P*< 0.05

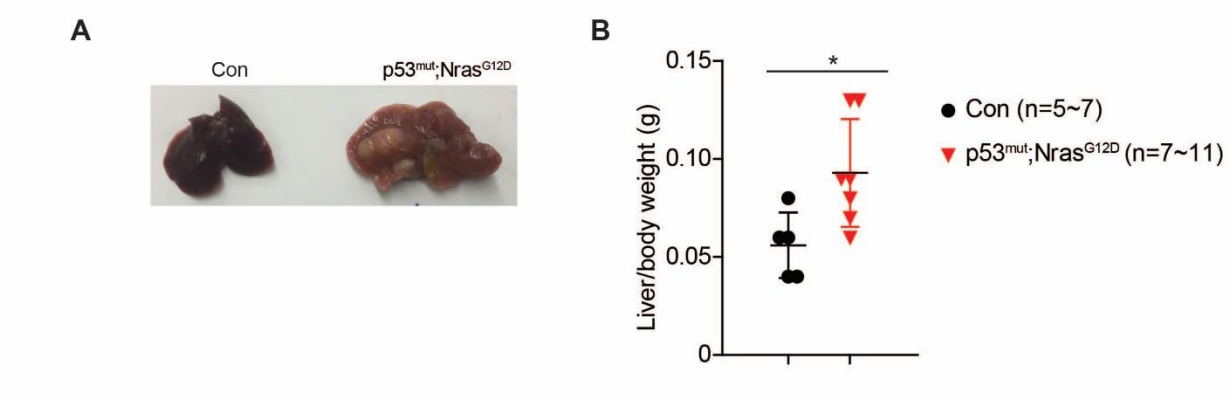

**Figure 3-S3: *p53$^{mut}$*; *Nras$^{G12D}$* induced AML is transplantable**

1X10$^6$ bone marrow cells from moribund primary AML *p53$^{mut}$; Nras$^{G12D}$* or age-matched control mice were transplanted into lethally irradiated syngeneic recipients (*p53$^{mut}$; Nras$^{G12D}$*-BMT or con-BMT) along with equal number of CD45.1$^+$ helper cells. (A) Percentage of donor derived cells in peripheral blood of recipients over time. (B) Kaplan-Meier comparative survival analysis of lethally irradiated recipients transplanted with either 0.5 X 10$^6$ bone marrow or splenocytes from moribund *p53$^{mut}$; Nras$^{G12D}$*- BMT mice along with equal number of CD45.1$^+$ helper cells**.** Percent survival was plotted against number of days after transplantation. *P* value was determined by log-rank test. * *P*< 0.05, ***P*< 0.01, ****P*< 0.001.

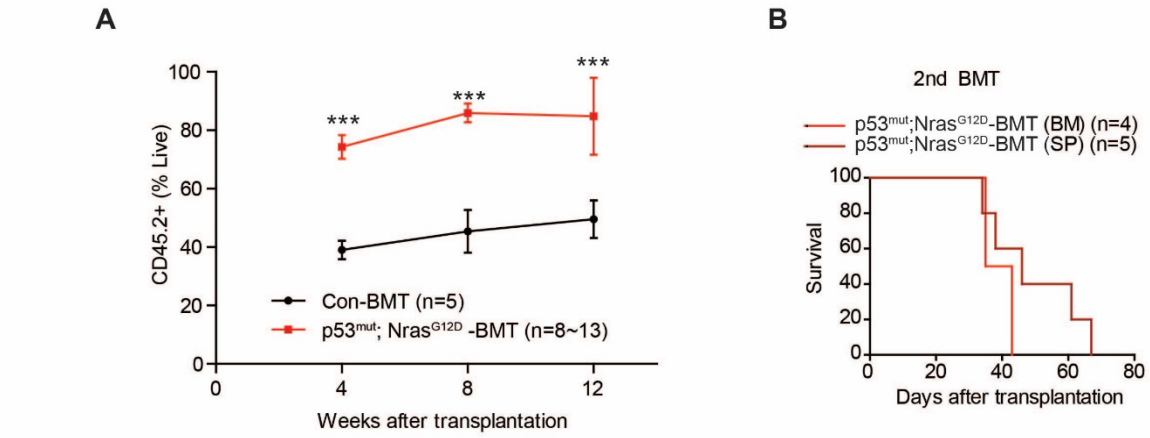

**Figure 3-S4: *p53*$^{mut}$; *Nras*$^{G12D}$ mice retain thymus at early stage**

(A) Schematic of experimental procedure: 6-7 week old Control, *p53*$^{mut}$, *Nras*$^{G12D}$ were treated with pI-pC and euthanized on day 12 along with untreated *p53*$^{mut}$*; Nras*$^{G12D}$ mice for downstream analyses (B-D). (B) Thymus weight of all four groups of euthanized mice. Data is presented as mean ± standard deviation (SD). * *P*< 0.05, ***P*< 0.01, ****P*< 0.001.

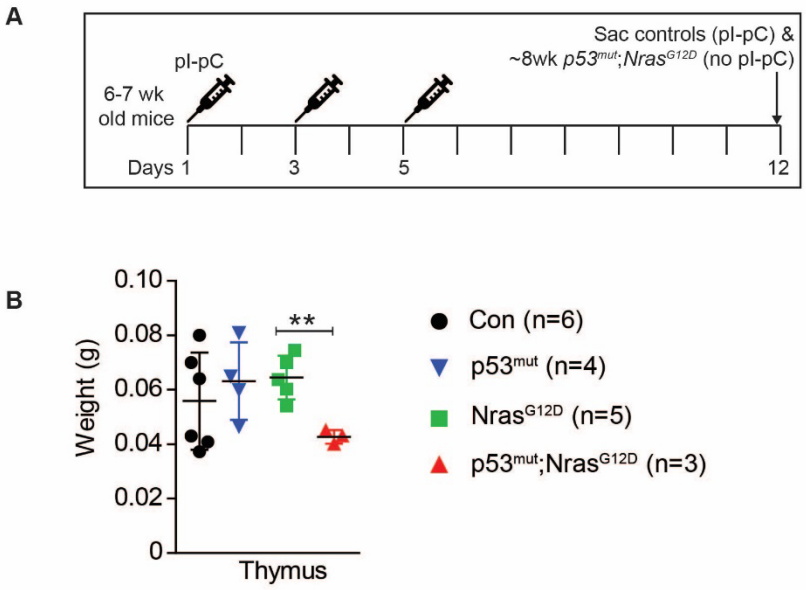

**Figure 3-S5: Cell cycle analysis of LSK, HSC and MPP cell populations**

Cell cycle analysis of bone marrow (A) LSK (B) HSC (defined as $CD48^{-}$ $CD150^{+}$ LSK) or (C) MPPs ($CD48^{-}$ $CD150^{-}$ LSK) using Ki-67/ 4',6-diamidino-2-phenylindole (DAPI) staining. Data is presented as mean ± standard deviation (SD). * $P< 0.05$, ** $P< 0.01$, *** $P< 0.001$.

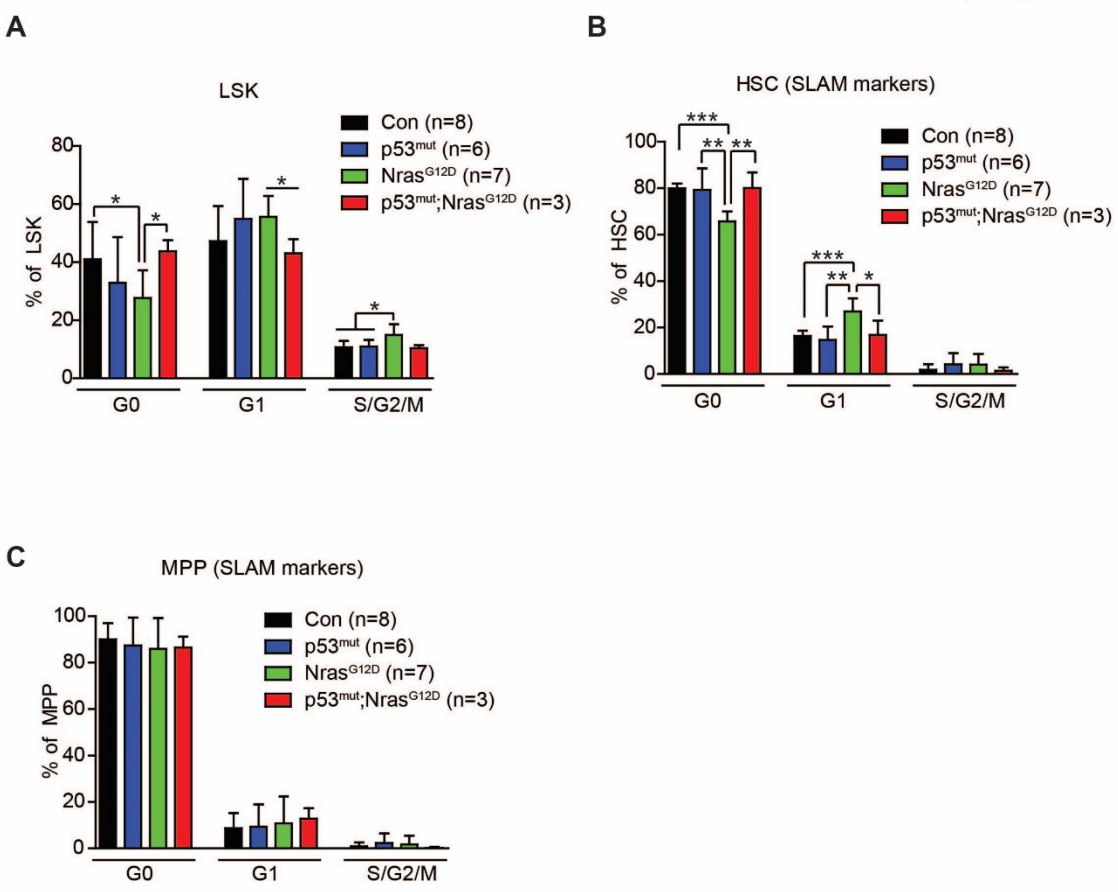

**Figure 3-S6: Gene expression of known positive and negative regulators of *RAS* pathway**

Bulk transcriptome analysis was performed using 50,000 sorted Lin$^-$ cKit$^+$ cells sorted from moribund AML *p53$^{mut}$; Nras$^{G12D}$* (n=4) and pI-pC treated age-matched control (n=3) bone marrow. (A, B) Volcano plot depicting (A) positive regulators of *RAS* pathway along with RPKM value of differentially expressed *Rasgrp4* (B) negative regulators of *RAS* pathway along with RPKM value of differentially expressed *Dab2ip*. *P* values were calculated using R Limma package statistics for differential expression analysis.

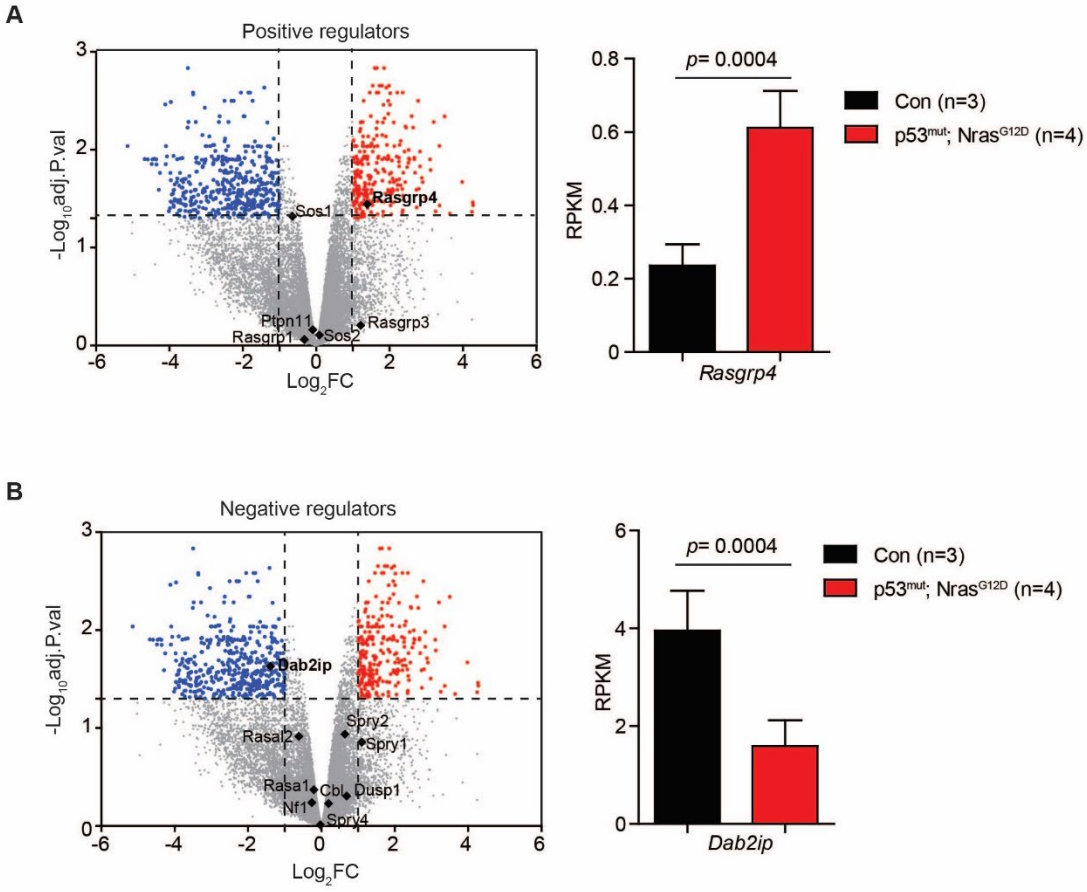

**Figure 3-S7: Inflammatory cytokines are upregulated in *p53$^{mut}$*; *Nras$^{G12D}$* primary and recipient mice**

Quantification of IL-6, IL-2 and TNFα cytokine in serum of control, ~8 week *p53$^{mut}$; Nras$^{G12D}$* mice and *p53$^{mut}$; Nras$^{G12D}$*-BMT mice (8 weeks after transplantation) using MSD's V-PLEX Proinflammatory panel 1 (mouse) assay kit. Data is presented as mean ± standard deviation (SD). * *P*< 0.05, ***P*< 0.01, ****P*< 0.001.

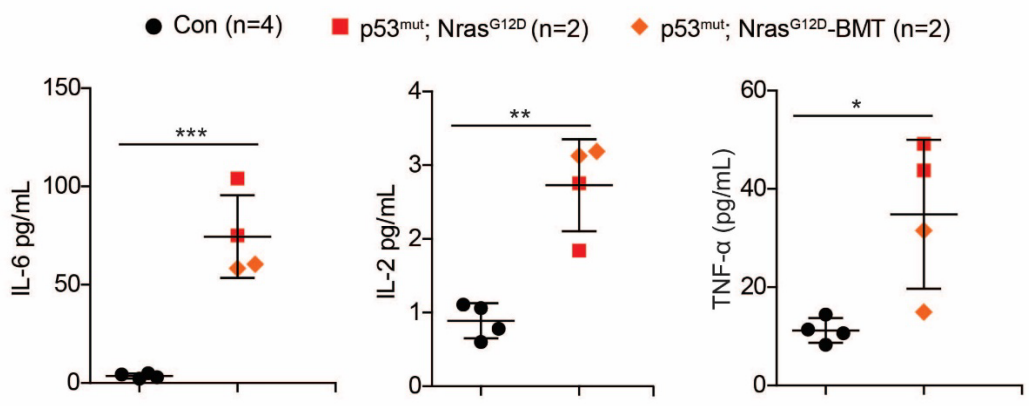

**Figure 3-S8: *Gata2* target genes are downregulated in *p53*$^{mut}$; *Nras*$^{G12D}$ Lin$^{-}$ cKit$^{+}$ cells**

RPKM values of master transcription factors *Gata2* target genes critical for erythroid development in *p53*$^{mut}$*; Nras*$^{G12D}$ and control samples from bulk transcriptome sequencing of sorted Lin$^{-}$ cKit$^{+}$ cells. RPKM, reads per kilobase per million mapped reads. Data is presented as mean ± standard deviation (SD). *P* values were calculated using R Limma package statistics for differential expression analysis.

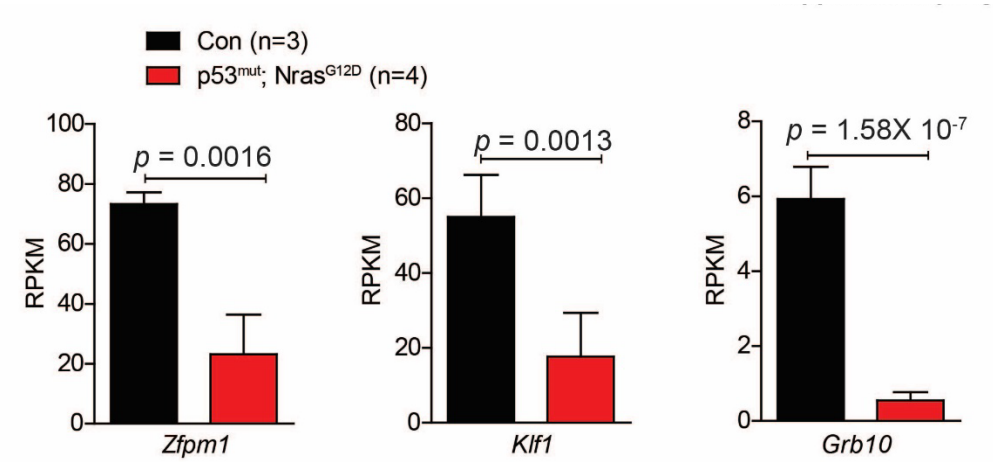

**Figure 3-S9: Schematic of cellular and molecular mechanisms of leukemogenesis in p53$^{mut}$; Nras$^{G12D}$ mice**

(Left) Mice expressing Nras$^{G12D/+}$ in the hematopoietic system develop chronic myelomonocytic leukemia (CMML) characterized by persistent monocytosis in peripheral blood. But these mice do not spontaneously transform to acute myeloid leukemia (AML), suggesting that additional genetic events are required to promote transformation. (Middle) Loss of tumor suppressor gene p53 cooperates with oncogenic Nras$^{G12D}$ to transform megakaryocyte-erythroid progenitor (MEP) cells and promote AML. (Right) AML patients with concurrent mutations in both RAS pathway and TP53 had a significantly shorter survival compared to single mutant patients. Majority of these TP53 mutations are missense, which can confer gain-of-function properties. Our study shows that p53$^{mut}$ and Nras$^{G12D}$ synergize to produce rapidly lethal AML in primary mice via mechanisms distinct from that of loss of p53. This genetic interaction perturbs key hematopoietic transcription factor (e.g., Gata2) networks, causes upregulation of several receptor-like tyrosine kinases and promotes systemic inflammation and AML.

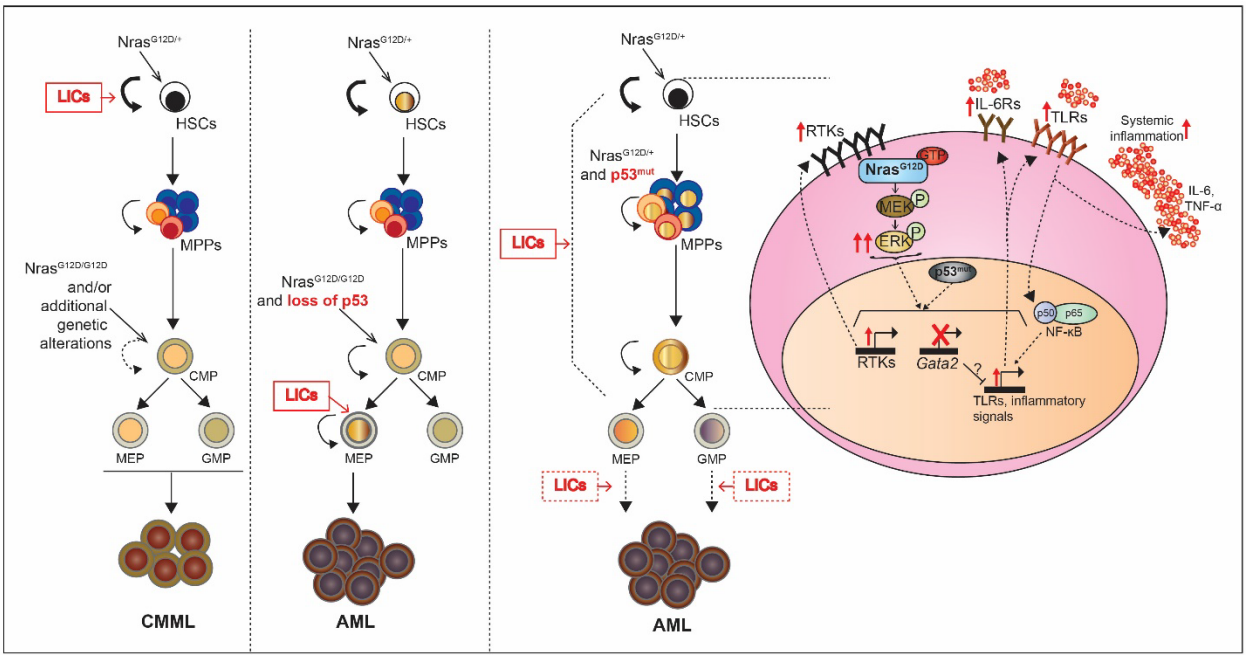

### 3.7 Tables

**Table 3-S1** *p53$^{mut}$; Nras$^{G12D}$* LSKs are fully transformed, while MEPs and GMPs are partially transformed

| Donor cell types | No. of donor cells | No. of helper cells | No. of recipient mice | Disease diagnosis | % Diseased animals |
|---|---|---|---|---|---|
| WBM (moribund) | 0.25 M | 0.25 M | 9 | AML | 100 |
| WBM (6 wk) | 0.25 M | 0.25 M | 5 | adv MPN/AML | 100 |
| LSK (6 wk) | 4000 | 0.25 M | 4 | adv MPN/AML | 100 |
| GMP (6 wk) | 4000 | 0.25 M | 4 | adv MPN/AML | 50 |
| MEP (6 wk) | 2000 | 0.25 M | 5 | adv MPN/AML | 60 |

### 3.8 References


1. Döhner, Hartmut, Daniel J. Weisdorf, and Clara D. Bloomfield. "Acute myeloid leukemia." New England Journal of Medicine 373.12 (2015): 1136-1152.
2. Dombret, Hervé, and Claude Gardin. "An update of current treatments for adult acute myeloid leukemia." *Blood* 127.1 (2016): 53-61.
3. Short, Nicholas J., et al. "Advances in the treatment of acute myeloid leukemia: new drugs and new challenges." *Cancer discovery* 10.4 (2020): 506-525.
4. Kastenhuber, Edward R., and Scott W. Lowe. "Putting p53 in context." *Cell* 170.6 (2017): 1062-1078.
5. Liu, Yan, et al. "p53 regulates hematopoietic stem cell quiescence." *Cell stem cell* 4.1 (2009): 37-48.
6. Prokocimer, Miron, Alina Molchadsky, and Varda Rotter. "Dysfunctional diversity of p53 proteins in adult acute myeloid leukemia: projections on diagnostic workup and therapy." *Blood* 130.6 (2017): 699-712.
7. Boettcher, Steffen, et al. "A dominant-negative effect drives selection of TP53 missense mutations in myeloid malignancies." *Science* 365.6453 (2019): 599-604.
8. Cancer Genome Atlas Research Network. "Genomic and epigenomic landscapes of adult de novo acute myeloid leukemia." *New England Journal of Medicine* 368.22 (2013): 2059-2074.
9. Shih, Alan H., et al. "Mutational analysis of therapy-related myelodysplastic syndromes and acute myelogenous leukemia." *Haematologica* 98.6 (2013): 908.
10. Rücker, Frank G., et al. "TP53 alterations in acute myeloid leukemia with complex karyotype correlate with specific copy number alterations, monosomal karyotype, and dismal outcome." *Blood* 119.9 (2012): 2114-2121.
11. Papaemmanuil, Elli, et al. "Genomic classification and prognosis in acute myeloid leukemia." *New England Journal of Medicine* 374.23 (2016): 2209-2221.
12. Lindsley, R. Coleman, et al. "Prognostic mutations in myelodysplastic syndrome after stem-cell transplantation." *New England Journal of Medicine* 376.6 (2017): 536-547.
13. Lindsley, R. Coleman, et al. "Acute myeloid leukemia ontogeny is defined by distinct somatic mutations." *Blood* 125.9 (2015): 1367-1376.
14. Donehower, Lawrence A., et al. "Mice deficient for p53 are developmentally normal but susceptible to spontaneous tumours." *Nature* 356.6366 (1992): 215-221.
15. Jacks, Tyler, et al. "Tumor spectrum analysis in p53-mutant mice." *Current biology* 4.1 (1994): 1-7.

16. Olive, Kenneth P., et al. "Mutant p53 gain of function in two mouse models of Li-Fraumeni syndrome." *Cell* 119.6 (2004): 847-860.
17. Lang, Gene A., et al. "Gain of function of a p53 hot spot mutation in a mouse model of Li-Fraumeni syndrome." *Cell* 119.6 (2004): 861-872.
18. Rampal, Raajit, et al. "Genomic and functional analysis of leukemic transformation of myeloproliferative neoplasms." *Proceedings of the National Academy of Sciences* 111.50 (2014): E5401-E5410.
19. Zhang, Jingfang, et al. "p53−/− synergizes with enhanced Nras G12D signaling to transform megakaryocyte-erythroid progenitors in acute myeloid leukemia." *Blood, The Journal of the American Society of Hematology* 129.3 (2017): 358-370.
20. Ward, Ashley F., Benjamin S. Braun, and Kevin M. Shannon. "Targeting oncogenic Ras signaling in hematologic malignancies." *Blood, The Journal of the American Society of Hematology* 120.17 (2012): 3397-3406.
21. Niemeyer, Charlotte M., and Christian Flotho. "Juvenile myelomonocytic leukemia: who's the driver at the wheel?." *Blood* 133.10 (2019): 1060-1070.
22. Itzykson, Raphaël, et al. "Clonal architecture of chronic myelomonocytic leukemias." *Blood, The Journal of the American Society of Hematology* 121.12 (2013): 2186-2198.
23. Merlevede, Jane, et al. "Mutation allele burden remains unchanged in chronic myelomonocytic leukaemia responding to hypomethylating agents." *Nature communications* 7.1 (2016): 1-13.
24. Onida, Francesco, and Miloslav Beran. "Chronic myelomonocytic leukemia: myeloproliferative variant." *Current hematology reports* 3 (2004): 218-226.
25. Ricci, Clara, et al. "RAS mutations contribute to evolution of chronic myelomonocytic leukemia to the proliferative variant." *Clinical Cancer Research* 16.8 (2010): 2246-2256.
26. Itzykson, Raphaël, et al. "Prognostic score including gene mutations in chronic myelomonocytic leukemia." *Journal of clinical oncology* 31.19 (2013): 2428-2436.
27. Elena, Chiara, et al. "Integrating clinical features and genetic lesions in the risk assessment of patients with chronic myelomonocytic leukemia." *Blood* 128.10 (2016): 1408-1417.
28. Patnaik, Mrinal M., et al. "Therapy related-chronic myelomonocytic leukemia (CMML): molecular, cytogenetic, and clinical distinctions from de novo CMML." *American journal of hematology* 93.1 (2018): 65-73.
29. Liu, Xin, et al. "RAS mutations in acute myeloid leukaemia patients: a review and meta-analysis." *Clinica Chimica Acta* 489 (2019): 254-260.

30. Bowen, David T., et al. "RAS mutation in acute myeloid leukemia is associated with distinct cytogenetic subgroups but does not influence outcome in patients younger than 60 years." *Blood* 106.6 (2005): 2113-2119.
31. Bacher, Ulrike, et al. "Implications of NRAS mutations in AML: a study of 2502 patients." *Blood* 107.10 (2006): 3847-3853.
32. Damm, Frederik, et al. "Integrative prognostic risk score in acute myeloid leukemia with normal karyotype." *Blood, The Journal of the American Society of Hematology* 117.17 (2011): 4561-4568.
33. Sano, Hirozumi, et al. "RAS mutations are frequent in FAB type M4 and M5 of acute myeloid leukemia, and related to late relapse: a study of the Japanese Childhood AML Cooperative Study Group." *International journal of hematology* 95.5 (2012): 509-515.
34. Schlenk, Richard F., et al. "Mutations and treatment outcome in cytogenetically normal acute myeloid leukemia." *New England Journal of Medicine* 358.18 (2008): 1909-1918.
35. Wang, Shujuan, et al. "Mutational spectrum and prognosis in NRAS-mutated acute myeloid leukemia." *Scientific Reports* 10.1 (2020): 1-9.
36. Ball, Brian J., et al. "The prognosis and durable clearance of RAS mutations in patients with acute myeloid leukemia receiving induction chemotherapy." *American journal of hematology* (2021).
37. Amatangelo, Michael D., et al. "Enasidenib induces acute myeloid leukemia cell differentiation to promote clinical response." *Blood, The Journal of the American Society of Hematology* 130.6 (2017): 732-741.
38. Choe, Sung, et al. "Molecular mechanisms mediating relapse following ivosidenib monotherapy in IDH1-mutant relapsed or refractory AML." *Blood advances* 4.9 (2020): 1894-1905.
39. Wang, Jinyong, et al. "Endogenous oncogenic Nras mutation promotes aberrant GM-CSF signaling in granulocytic/monocytic precursors in a murine model of chronic myelomonocytic leukemia." *Blood, The Journal of the American Society of Hematology* 116.26 (2010): 5991-6002.
40. Li, Qing, et al. "Hematopoiesis and leukemogenesis in mice expressing oncogenic NrasG12D from the endogenous locus." *Blood, The Journal of the American Society of Hematology* 117.6 (2011): 2022-2032.
41. Padua, R. A., et al. "RAS, FMS and p53 mutations and poor clinical outcome in myelodysplasias: a 10-year follow-up." *Leukemia* 12.6 (1998): 887-892.

42. Zhao, Zhen, et al. "Cooperative loss of RAS feedback regulation drives myeloid leukemogenesis." *Nature genetics* 47.5 (2015): 539-543.
43. Olivier, Magali, Monica Hollstein, and Pierre Hainaut. "TP53 mutations in human cancers: origins, consequences, and clinical use." *Cold Spring Harbor perspectives in biology* 2.1 (2010): a001008.
44. Muller, Patricia AJ, and Karen H. Vousden. "Mutant p53 in cancer: new functions and therapeutic opportunities." *Cancer cell* 25.3 (2014): 304-317.
45. Zhu, Jiajun, et al. "Gain-of-function p53 mutants co-opt chromatin pathways to drive cancer growth." *Nature* 525.7568 (2015): 206-211.
46. Loizou, Evangelia, et al. "A gain-of-function p53-mutant oncogene promotes cell fate plasticity and myeloid leukemia through the pluripotency factor FOXH1." *Cancer discovery* 9.7 (2019): 962-979.
47. Kong, Guangyao, et al. "The ability of endogenous Nras oncogenes to initiate leukemia is codon-dependent." *Leukemia* 30.9 (2016): 1935-1938.
48. Wang, Jinyong, et al. "Endogenous oncogenic Nras mutation initiates hematopoietic malignancies in a dose-and cell type-dependent manner." *Blood, The Journal of the American Society of Hematology* 118.2 (2011): 368-379.
49. Wang, Jinyong, et al. "NrasG12D/+ promotes leukemogenesis by aberrantly regulating hematopoietic stem cell functions." *Blood, The Journal of the American Society of Hematology* 121.26 (2013): 5203-5207.
50. Pietras, Eric M., et al. "Functionally distinct subsets of lineage-biased multipotent progenitors control blood production in normal and regenerative conditions." *Cell stem cell* 17.1 (2015): 35-46.
51. Forsberg, E. Camilla, et al. "Differential expression of novel potential regulators in hematopoietic stem cells." *PLoS Genet* 1.3 (2005): e28.
52. Krivtsov, Andrei V., et al. "Transformation from committed progenitor to leukaemia stem cell initiated by MLL–AF9." *Nature* 442.7104 (2006): 818-822.
53. Pant, Vinod, Alfonso Quintás-Cardama, and Guillermina Lozano. "The p53 pathway in hematopoiesis: lessons from mouse models, implications for humans." *Blood, The Journal of the American Society of Hematology* 120.26 (2012): 5118-5127.
54. Zhou, Yingyao, et al. "Metascape provides a biologist-oriented resource for the analysis of systems-level datasets." *Nature communications* 10.1 (2019): 1-10.
55. Han, Heonjong, et al. "TRRUST v2: an expanded reference database of human and mouse transcriptional regulatory interactions." *Nucleic acids research* 46.D1 (2018): D380-D386.

56. Mehta, Charu, et al. "Integrating enhancer mechanisms to establish a hierarchical blood development program." *Cell reports* 20.12 (2017): 2966-2979.
57. Johnson, Kirby D., et al. "Cis-regulatory mechanisms governing stem and progenitor cell transitions." *Science advances* 1.8 (2015): e1500503.
58. Cai, Xiongwei, et al. "Runx1 loss minimally impacts long-term hematopoietic stem cells." *PloS one* 6.12 (2011): e28430.
59. Subramanian, Aravind, et al. "Gene set enrichment analysis: a knowledge-based approach for interpreting genome-wide expression profiles." *Proceedings of the National Academy of Sciences* 102.43 (2005): 15545-15550.
60. Bellissimo, Dana C., et al. "Runx1 negatively regulates inflammatory cytokine production by neutrophils in response to Toll-like receptor signaling." *Blood advances* 4.6 (2020): 1145-1158.
61. Meisel, Marlies, et al. "Microbial signals drive pre-leukaemic myeloproliferation in a Tet2-deficient host." *Nature* 557.7706 (2018): 580-584.
62. Reynaud, Damien, et al. "IL-6 controls leukemic multipotent progenitor cell fate and contributes to chronic myelogenous leukemia development." *Cancer cell* 20.5 (2011): 661-673.
63. Chang, Yuan-I., et al. "Loss of Dnmt3a and endogenous Kras G12D/+ cooperate to regulate hematopoietic stem and progenitor cell functions in leukemogenesis." *Leukemia* 29.9 (2015): 1847-1856.
64. Akira, Shizuo, and Kiyoshi Takeda. "Toll-like receptor signalling." *Nature reviews immunology* 4.7 (2004): 499-511.
65. Kawai, Taro, and Shizuo Akira. "TLR signaling." *Cell Death & Differentiation* 13.5 (2006): 816-825.
66. Johnson, Kirby D., et al. "Constructing and deconstructing GATA2-regulated cell fate programs to establish developmental trajectories." *Journal of Experimental Medicine* 217.11 (2020).
67. Farr, Laura, Swagata Ghosh, and Shannon Moonah. "Role of MIF Cytokine/CD74 receptor pathway in protecting against injury and promoting repair." *Frontiers in Immunology* 11 (2020).
68. Scheller, Jürgen, et al. "The pro-and anti-inflammatory properties of the cytokine interleukin-6." *Biochimica et Biophysica Acta (BBA)-Molecular Cell Research* 1813.5 (2011): 878-888.
69. Steelman, L. S., et al. "Roles of the Ras/Raf/MEK/ERK pathway in leukemia therapy." Leukemia 25.7 (2011): 1080-1094

70. Weisberg, Ellen, et al. "FLT3 inhibition and mechanisms of drug resistance in mutant FLT3-positive AML." *Drug Resistance Updates* 12.3 (2009): 81-89.
71. Matsumoto, Misako, and Tsukasa Seya. "TLR3: interferon induction by double-stranded RNA including poly (I: C)." *Advanced drug delivery reviews* 60.7 (2008): 805-812.
72. Wen, Zhi, et al. "Nras Q61R/+ and Kras−/− cooperate to downregulate Rasgrp1 and promote lympho-myeloid leukemia in early T-cell precursors." Blood, The Journal of the American Society of Hematology 137.23 (2021): 3259-3271.

# Chapter 4

# Conclusions & Future Directions

## 4.1 Introduction

*RAS* genes constitute the most frequently mutated oncogene family in human cancers and are important for tumor progression (1). *RAS* genes display isoform and codon specific differences in the types of cancer they are predominantly mutated. For example, in hematological malignancies, *KRAS* and *NRAS* mutations are common, whereas *HRAS* is rarely mutated (2). *NRAS* Q61 mutations are predominant in plasma cell myeloma, whereas *NRAS* G12 mutations are more common in acute myeloid leukemia (3). *RAS* mutations cooperate with other genetic alterations to enhance tumor formation and progression (4-6). Herein, we delineate the mechanisms of how different oncogenic *Nras* codon mutations synergize with interacting partners to promote different hematological malignancies. The work described here contributes to the expanding body of work done to better understand the cellular, molecular and disease phenotypes of *RAS* codon mutational preferences seen in patient tumors. In the future, additional work could be directed towards the following avenues.

## 4.2 To determine whether combinatorial therapy of MEK inhibition and immunotherapy agents can alleviate MM phenotypes

Our VQ model recapitulated many biological and clinical features characteristic of human advanced MM, including preservation of immune-checkpoint pathways PD-1/PD-L1 and CD155/TIGIT, which can mediate T-cell suppression in MM patients leading to myeloma escape (7-9). However, PD-1 blockade as a monotherapy does not produce sufficient anti-myeloma responses, thus prompting investigation into combinatorial therapeutic strategies (10,11). Given that trametinib, a MEK inhibitor, inhibited VQ MM cell growth *in vitro* and significantly reduced PD-L1 surface expression on myeloma cells, its effects in combination with anti-PD-1/PD-L1 antibody need to be explored. As the VQ cell lines also express PD-L1 on the surface, they can be successfully used to first test efficacy of single agent (anti-PD-L1) and in combination with trametinib at various dosages in a co-culture system with isolated CD8+ T cells. Cell viability will

be measured after a short period of incubation (5-7 days) using CellTiter-Glo assay to determine $IC_{50}$ concentrations and combination index. Additionally, surface expression of PD-L1 and checkpoint ligands will be measured after combination therapy. Depending on *in vitro* results, this therapeutic strategy can be tested *in vivo* in transplantation models.

### 4.3 To generate a humanized VQ model for testing immunomodulatory drugs

Many MM treatment regimens currently in use involve two or more active drugs. These drugs fall into four major categories: alkylating agents (e.g. melphalan and cyclophosphamide), corticosteroids (e.g. dexamethasone and prednisone), immunomodulatory drugs (e.g. lenalidomide, pomalidomide, and thalidomide) and proteasome inhibitors (e.g. bortezomib and carfilzomib) (16). The preferred initial therapy includes a three-drug combination of bortezomib, lenalidomide, and dexamethasone (dubbed VRd). In humans, thalidomide or its analogs bind to Cereblon (CRBN), the substrate adaptor of an E3 ubiquitin ligase complex, and alter its substrate specificity, resulting in degradation of key transcription factors, Ikaros (IKZF1) and Aiolos (IKZF3) (17). Unfortunately, thalidomide and its derivatives lack activity in murine models. A knock-in mouse model where a single amino acid substitution in mouse Cereblon (*Crbn*$^{I391V}$) renders the animals responsive to thalidomide and its derivatives has been recently described (18). Thus, in order to identify new MEK inhibition-based combination therapies relevant in clinical setting, the VQ model can be introduced into Crbn$^{1391V}$ background to develop a humanized VQ model in which immunomodulatory drugs can also be tested.

### 4.4 To identify therapeutic susceptibilities in VQ model by re-purpose screen of FDA approved drugs

We showed that US FDA approved MEK inhibitor trametinib killed MM cells in a dose dependent manner with an $IC_{50}$ of 5-10nM (22). Furthermore, trametinib treatment significantly reduced surface expression of PD-L1 on MM cell lines (22). Mice transplanted with VQ-D1 cells also

showed significantly prolonged survival upon trametinib treatment, compared to control (22). These results provide a strong rationale for MEK inhibition-based combination therapies which can be developed using the myeloma cell lines. For this, a high throughput screening assay was set up at the Small Molecule Screening Facility to screen for potential drug combinations among several available FDA approved drug libraries, e.g., NCI panel of 147 anti-cancer drugs. VQ cell lines were cultured and expanded prior to the drug screening and treated with drug candidates at 100nM and 10000nM with or without trametinib (10nM) for 48 hours. Cell viability was then quantified using CellTiter-Glo luminescence assay. Trametinib alone serves as positive control while DMSO treated cells are negative control. A graph of viability fold change of anti-cancer drug alone (X axis) vs viability fold change in combination with 10nM trametinib (Y axis) was plotted, with area under the curve representing increased efficacy of combination therapy with trametinib. This platform could be easily adapted to screen all FDA-approved drugs and positive hits may be further validated in vitro and in vivo.

### 4.5 To identify transcription factors downstream of oncogenic Ras that bind to mutant p53 and drive AML

We showed that several key transcription factor (TF) networks are perturbed in $p53^{mut}$; $Nras^{G12D}$ AML cells through bulk RNA-seq study. We hypothesize that mutant p53 interacts with TFs downstream of oncogenic Ras to drive the AML signature. To test this hypothesis, p53 (along with interacting partners) will be immunoprecipitated from equal number of WT and mutant p53 $Nras^{G12D}$ BM cells and used for quantitative mass spectrometry. p53-null $Nras^{G12D}$ cells will serve as negative control. Peptides significantly enriched in mutant p53 background compared to WT and p53-null, which also correlate with our RNA-seq results and publicly available p53 ChIP-seq dataset will be prioritized further. In the event that p53 cannot be readily immunoprecipitated, the mice will be sublethally irradiated and BM cells will be harvested within 1-2 hours and used for IP-mass spec. Alternatively, KY821 human leukemia cell line that contains oncogenic *NRAS*

mutation and *P53*$^{R175H}$ mutation (which corresponds to *p53*$^{R172H}$ in mice) can be used. Top 3-5 candidates from the list will be further validated by performing reciprocal IP in *p53*$^{mut}$*; Nras*$^{G12D}$ AML cells (or KY821 cells). To determine specificity of interactions, K562 cell line with WT TP53 and control BM cell lysates will be used as controls. Validated targets will be knocked down in *p53*$^{mut}$; *Nras*$^{G12D}$ AML cells and resulting transcriptome changes will be evaluated using bulk RNA-seq to determine pathway changes that are crucial for AML. The target genes regulated by identified TFs & mutant p53 will be defined as genes that are differentially regulated after TF knockdown in the direction opposite to that of the initial RNA-seq experiment.

### 4.6 To determine whether Gata2 re-expression in *p53*$^{mut}$*; Nras*$^{G12D}$ cells can downregulate TLR and inflammatory signaling

We showed that Gata TF networks were enriched in downregulated genes in our RNA-seq data and the expression of both Gata1 and Gata2 were downregulated in *p53*$^{mut}$*; Nras*$^{G12D}$ cells. In addition, genes downregulated in *Gata2* enhancer -77$^{-/-}$ fetal liver MPs were also downregulated in *p53*$^{mut}$*; Nras*$^{G12D}$ cells (12). *Gata2* downregulation in fetal liver MPs results in upregulation of TLR and inflammatory pathways (13). As described previously, *p53*$^{mut}$*; Nras*$^{G12D}$ primary mice were associated with progressive loss of lymphocytes, including T cells and negligible thymus at moribund stage. Moribund recipients of AML cells also showed a reduced T-cell compartment in hematopoietic tissues. We recently demonstrated that recipients transplanted with Gata2 enhancer +9.5$^{+/-}$ BM cells had reduced number of donor-derived lymphoid-primed multipotent progenitors (LMPPs) leading to decreased donor-derived T cells (19). Additionally, several studies have shown that systemic inflammation promotes myelopoiesis in lieu of lymphopoiesis (20,21). Taken together, we hypothesize that loss of Gata2 TF activity in *p53*$^{mut}$*; Nras*$^{G12D}$ HSPCs results in the predominant inflammatory gene signatures including TLR pathway upregulation, with concomitant decrease in T-cell compartment. To test this hypothesis, Gata2 expression will be restored using retroviral transduction in *p53*$^{mut}$*; Nras*$^{G12D}$ cells with Gata2 vector and control vector

(negative control), with the aim to achieve Gata2 expression levels comparable to endogenous levels. Bulk RNA-seq will be performed with these samples to ascertain transcriptome change downstream of Gata2 re-expression. Comparison with earlier RNA-seq data will reveal the extent of rescue, including which pathways downstream of Gata2 were important. The Gata2 or control vector transduced mutant cells will be transplanted into sublethally irradiated mice to determine whether re-expression of Gata2 prolongs survival of mice and examine effect on donor-derived T-cell compartment. Pathways downstream of Gata2 TF activity identified from the RNA-seq experiment will also be evaluated in these mice. For example, NFκB pathway, a major contributor to inflammation, will be evaluated using western blotting and/or Image-Stream to quantify nuclear:cytoplasmic localization of NFκB transcription factors.

### 4.7 To determine whether *p53$^{mut}$; Nras$^{G12D}$* MPPs have a differentiation defect

We showed that *p53$^{mut}$; Nras$^{G12D}$* mice rapidly developed a fully penetrant AML, and the HSPCs displayed a strong MPP gene signature. We also observed that LSK population was fully transformed and induced AML in 100% recipients, while MEPs and GMPs were only partially transformed. LSK population is a heterogeneous mix of several subpopulations, including several distinctly lineage primed MPPs (14). We found that although all lineage primed MPPs were expanded, this expansion was not entirely replicated in downstream progenitors. For example, in the bone marrow, the lymphoid primed MPP4 expansion did not lead to increased downstream CLPs, and similarly, the myeloid primed MPP2/3 expansion caused downstream CMP expansion but not GMPs and MEPs. To determine whether an MPP differentiation defect exists, I will perform myeloid and lymphoid colony assays using sorted MPP 2, MPP3 and MPP4 cells using the surface markers listed in Pietras et al (14). Briefly, bone marrow cells will be isolated from 6-8 week old *p53$^{mut}$; Nras$^{G12D}$* mice, stained for the appropriate surface markers, and MPP2/3/4 cells will be sorted. Myeloid colony cultures will be performed in semisolid methylcellulose culture media, while lymphoid colony cultures will be performed by co-culture assays with OP-9 and OP-

9/DL1 cells to determine B and T cell differentiation potential. Additionally, these MPP cell subsets will be transplanted into lethally irradiated mice with 0.25 million helper cells and disease phenotypes (if any) will be monitored, along with monthly donor derived percentage evaluation in the peripheral blood. These experiments will further shed light on the complex mechanisms underlying the LIC transformation.

### 4.8 To identify therapeutic susceptibilities in *p53$^{mut}$; Nras$^{G12D}$* driven AML

*TP53* mutations in AML patients independently predict poor survival outcome, and frequently associate with complex karyotype, an adverse prognostic factor (15, 16). We have previously reported that patients with concurrent mutations in *TP53* and *RAS* pathways have shorter survival than patients with single pathway mutations (6). Majority of these *TP53* mutations are missense mutations that occur in hotspots including R172. Patients with *TP53* AML treated with standard anthracycline-based and ARA-C based therapy show poor outcomes (17). Thus, the *p53$^{mut}$; Nras$^{G12D}$* AML model can potentially be used to explore MEK-inhibition based combinatorial therapeutic regimens. In this regard, a repurpose screening of 2580 FDA- approved drugs that include a diverse array of treatments for oncology, cardiology, anti-inflammation will be done. Briefly, splenocytes from moribund *p53$^{mut}$; Nras$^{G12D}$* mice will be harvested and treated with increasing concentrations of trametinib (MEK inhibitor) to determine the $IC_{50}$. Next, a large scale pilot screening will be done using AML splenocytes with single FDA approved drug as well as in combination with trametinib at its $IC_{50}$ concentration. Potential hits arising from initial screening experiments will be further validated *in vitro*.

### 4.9 Final conclusion

The work described herein sheds light on how different oncogenic *Nras* codons cooperate with genetic alterations to promote different types of hematological cancers. *Nras$^{Q61R}$* cooperates with *MYC* transgene in plasma cells to induce a highly malignant multiple myeloma, while *Nras$^{G12D}$*

synergizes with missense mutant *p53* to promote a fully penetrant AML-like disease. Both these models describe how elevated oncogenic Nras signaling can play an important role in promoting aggressive tumor phenotypes thus providing a strong rationale for developing combinatorial therapies targeting downstream Ras signaling. The resources generated herein will prove to be useful in developing such therapeutic regimens.

### 4.10 References


1. Cox, Adrienne D., et al. "Drugging the undruggable RAS: mission possible?" Nature reviews Drug discovery 13.11 (2014): 828-851.
2. Ward, Ashley F., Benjamin S. Braun, and Kevin M. Shannon. "Targeting oncogenic Ras signaling in hematologic malignancies." Blood, The Journal of the American Society of Hematology 120.17 (2012): 3397-3406.
3. Kong, Guangyao, et al. "The ability of endogenous Nras oncogenes to initiate leukemia is codon-dependent." Leukemia 30.9 (2016): 1935-1938.
4. Hingorani, Sunil R., et al. "Trp53R172H and KrasG12D cooperate to promote chromosomal instability and widely metastatic pancreatic ductal adenocarcinoma in mice." Cancer cell 7.5 (2005): 469-483.
5. Haigis, Kevin M., et al. "Differential effects of oncogenic K-Ras and N-Ras on proliferation, differentiation and tumor progression in the colon." Nature genetics 40.5 (2008): 600.
6. Zhang, Jingfang, et al. "p53−/− synergizes with enhanced Nras G12D signaling to transform megakaryocyte-erythroid progenitors in acute myeloid leukemia." Blood, The Journal of the American Society of Hematology 129.3 (2017): 358-370.
7. Guillerey, Camille, et al. "TIGIT immune checkpoint blockade restores CD8+ T-cell immunity against multiple myeloma." *Blood* 132.16 (2018): 1689-1694.
8. Jelinek, T., and R. Hajek. "PD-1/PD-L1 inhibitors in multiple myeloma: The present and the future." *Oncoimmunology* 5.12 (2016): e1254856.
9. Minnie, Simone A., et al. "Myeloma escape after stem cell transplantation is a consequence of T-cell exhaustion and is prevented by TIGIT blockade." *Blood* 132.16 (2018): 1675-1688.
10. Suen, H., et al. "The failure of immune checkpoint blockade in multiple myeloma with PD-1 inhibitors in a phase 1 study." *Leukemia* 29.7 (2015): 1621-1622.

11. Costa, Federica, et al. "Checkpoint inhibition in myeloma: opportunities and challenges." *Frontiers in immunology* 9 (2018): 2204.
12. Pietras, Eric M., et al. "Functionally distinct subsets of lineage-biased multipotent progenitors control blood production in normal and regenerative conditions." *Cell stem cell* 17.1 (2015): 35-46.
13. Papaemmanuil, Elli, et al. "Genomic classification and prognosis in acute myeloid leukemia." *New England Journal of Medicine* 374.23 (2016): 2209-2221.
14. Rücker, Frank G., et al. "TP53 alterations in acute myeloid leukemia with complex karyotype correlate with specific copy number alterations, monosomal karyotype, and dismal outcome." *Blood* 119.9 (2012): 2114-2121.
15. Grossmann, Vera, et al. "A novel hierarchical prognostic model of AML solely based on molecular mutations." *Blood, The Journal of the American Society of Hematology* 120.15 (2012): 2963-2972.
16. Rajkumar, S. Vincent, and Shaji Kumar. "Multiple myeloma current treatment algorithms." Blood cancer journal 10.9 (2020): 1-10.
17. Krönke, Jan, et al. "Lenalidomide causes selective degradation of IKZF1 and IKZF3 in multiple myeloma cells." Science 343.6168 (2014): 301-305.
18. Fink, Emma C., et al. "Crbn I391V is sufficient to confer in vivo sensitivity to thalidomide and its derivatives in mice." Blood, The Journal of the American Society of Hematology 132.14 (2018): 1535-1544.
19. You, Xiaona, et al. "Gata2+ 9.5 enhancer regulates adult hematopoietic stem cell self-renewal and T cell development." Blood Advances (2021).
20. Boettcher, Steffen, et al. "Cutting edge: LPS-induced emergency myelopoiesis depends on TLR4-expressing nonhematopoietic cells." The Journal of Immunology 188.12 (2012): 5824-5828.

21. Reynaud, Damien, et al. "IL-6 controls leukemic multipotent progenitor cell fate and contributes to chronic myelogenous leukemia development." Cancer cell 20.5 (2011): 661-673.
22. Wen, Zhi, et al. "Expression of NrasQ61R and MYC transgene in germinal center B cells induces a highly malignant multiple myeloma in mice." Blood 137.1 (2021): 61-74.